Variational-Bound Finite-Element Methods for Three-Dimensional Low-Reynolds-Number Porous Media and Sedimentation Flows

by

Matteo Pedercini

B.S., University of Virginia (1993)

Submitted to the Department of Mechanical Engineering
in partial fulfillment of the requirements for the degree of

Master of Science in Mechanical Engineering

at the

MASSACHUSETTS INSTITUTE OF TECHNOLOGY

September 1995

Author .....
Department of Mechanical Engineering
August 25, 1995

Certified by .....
Anthony T. Patera
Professor of Mechanical Engineering
Thesis Supervisor

Accepted by .....
Ain A. Sonin
Chairman, Departmental Committee on Graduate Students

Variational-Bound Finite-Element Methods for Three-Dimensional Low-Reynolds-Number Porous Media and Sedimentation Flows

by

Matteo Pedercini

Submitted to the Department of Mechanical Engineering
on August 25, 1995, in partial fulfillment of the
requirements for the degree of
Master of Science in Mechanical Engineering

Abstract

Two phase media are of great importance in science and engineering. In general, two phase systems can be divided into particulate and fibrous materials. This thesis focuses on the former type of material, in which many inclusions are dispersed in a continuous matrix. In particular, we analyze three-dimensional porous media and sedimentation flows at negligible Reynolds numbers, when the particulate phase consists of monodisperse spheres. Because of the complex microstructure of such systems, it is convenient to focus on their macroscopic behavior rather than on their detailed microscopic workings: it is common practice to replace the inhomogeneous materials with a homogenized medium having the appropriate effective property. For this reason, we focus on procedures that yield the permeability and the average settling speed that characterize porous media and suspensions, respectively.

Our methodology consists of the analysis of three scale-decoupled subproblems: the macro-, meso-, and micro-scale subproblems. In the macro-scale analysis the bulk quantity of interest is determined by using the effective property. The meso-scale subproblem yields the effective macroscopic property of interest, provided the statistics related to the spatial distribution of the inclusions are known. In fact, the solution is achieved by solving the transport equations over a statistically significant periodic cell extracted from the original medium. The solution of the governing equations is approximated by the finite-element solution over the appropriate spaces. Lastly, the micro-scale treatment is useful when two or more meso-scale inclusions are very close to each other. This geometrically stiff problem is alleviated by introducing geometry changes that also have bounding properties on the effective property of interest.

Although our methodology can treat statistically random distributions of spherical inclusions, we focus on very simple periodic sphere distributions to validate our porous media and sedimentation formulations.

Thesis Supervisor: Anthony T. Patera
Title: Professor of Mechanical Engineering

Acknowledgments

First, and foremost, I would like to thank Professor Anthony T. Patera for his support and impeccable guidance provided during my experience at MIT. I am also grateful to Dr. Manuel Cruz for laying out the sedimentation formulation and for explaining many aspects of the analysis of multicomponent media. Professor Jaime Peraire, of the Department of Aeronautics and Astronautics of MIT, was invaluable for providing us with the mesh generator FELISA. Lastly, I would like to thank all the members of the Fluid Mechanics Laboratory for creating a very friendly and laid back working environment.

This work was supported by the Advanced Research Projects Agency under Grant N00014-91-J-1889, by the Office of Naval Research under Grants N00014-90-J-4124 and N00014-89-J-1610, and by the Air Force Office of Scientific Research under Grant F49620-94-1-0121.

I would also like to acknowledge the MIT Starr Foundation for the Starr Fellowship that supported my studies for the first two semesters.

Contents

Chapter 1

Introduction

1.1 Motivation

Multicomponent media are of great importance in science and engineering. Among multicomponent media, two phase materials are the simplest and most common. In general, two phase systems can be divided into particulate and fibrous materials. In this thesis we focus on the former type of materials, in which a great number of particles is dispersed in a continuous matrix. More specifically, we concern ourselves with highly viscous flow through porous media and low Reynolds number sedimentation. The former process is of relevance in filtering, ground water flow, oil recovery and powder metallurgy, among others [44]. The latter is used to separate particles from a fluid, as well as to separate particles having different settling speeds [12]. Because of the complex microstructure of such systems, it is convenient to focus on their macroscopic behavior rather than on their detailed microscopic workings. In fact, it is common engineering practice to replace the original particulate media with a homogeneous material having an appropriate effective property. For this reason, we focus on procedures that yield the permeability and average settling speed that characterize porous media and suspensions, respectively.

Most analytical and numerical methods have serious shortcomings in determining these macroscopic properties. On one hand, the first class of methods have difficulty with random distributions of particles, specially at non-dilute concentrations.

Moreover, in Stokes flows, the fluid motion induced by a moving boundary decays very slowly with distance, so far field conditions have to be modeled correctly. On the other hand, numerical methods are limited by the number of particles that can be modeled. In addition, the presence of disparate length scales results in excessive degrees-of-freedom. Even experimental procedures are not always successful since they provide results that are only valid for the tested specimens.

The analytico-computational method we propose is able to overcome many of these obstacles. However, our methodology must still assume that a probabilistic particle distribution is given. Whereas most porous media analyses rely on this assumption, many sedimentation analyses do not. In fact, many researchers strive to *determine* the particle distribution by dynamically tracking the motion of a suspension [16] [32]. We, on the other hand, follow the approach of other researchers, such as Batchelor [2], that argue that the particle distribution can be assumed and the particle motions determined statistically by averaging over several "snapshots" of the system.

In the next section, some previous efforts to determine the effective permeability and average settling rate are reviewed.

1.2 Previous Work

There have been many efforts to calculate the effective properties of interest. The methods vary from purely analytical to purely computational. What follows is a brief discussion of some investigations.

Porous Media

One of the most useful approaches, specially before the advent of the digital computer, is to obtain bounds on the effective property. Early on, Prager [40] developed bounds on the effective permeability that only required the volume concentration of the inclusions as input. Although these bounds offer the advantage of being general and not requiring data that typically cannot be obtained, they are crude since they do not depend on the micro-structure of the porous media. More recently, Torquato [48]

has reviewed advances in determining sharper bounds on the permeability by using n-point correlation functions that characterize a random media. Unfortunately, these bounds are presently *potentially* sharp, since high order correlation functions cannot be measured by modern technology.

Some researchers have tried to provide exact analytical solutions. Unfortunately, their results are either limited to highly regular periodic arrangements of the inclusions or to dilute particle concentrations. For example, Zick & Homsy [49] solve for the drag exerted on a regular array of spheres by transforming the differential equations that govern the flow into integral equations and then using a Galerkin method to arrive at the solution. Batchelor [3] discusses random particulate media limited to low concentrations. Brady & Bossis [5] and Durlofsky, Brady & Bossis [15] propose a dynamic simulation technique applicable to a variety of particulate media problems. Their method, "Stokesian dynamics", relies on mobility-resistance functions for Stokes flows. Unfortunately, their simulation techniques are not always exact. For instance, they compare their permeability results for a regular cubic array of spheres with those of Zick & Homsy [49] and show that for high concentrations the results can be off by about 50%.

With the advent of fast computers, part of the research community has pursued a purely computational approach to multicomponent media. Some authors employ classic numerical techniques such as the finite volume method to resolve the flow around an array of spheres [10]. The main drawback of such methods is the limited number of inclusions that can be modeled. A different approach is used by authors such as Rothman [41] who applies the lattice-gas automata to the porous media problem. This method uses fictitious particles of identical mass that hop from site to site on a regular lattice undergoing ideal collisions. Lattice-gas methods are still in their infancy, and it is not clear that they always model the underlying physics correctly.

Ultimately, permeability results have to be compared with experimental data. Permeability measurements can be performed quite simply by means of Darcy's law. However, these results are not very general unless they can be related to the micro-

structure of the material being tested [44]. To date, there is much uncertainty on the type of micro-structure that characterizes a particulate medium.

Sedimentation

As for the porous media problem, some authors describe general extremum principles to bound the settling speed of a suspension. For example, Keller, Lester & Rubenfeld [28] give a lower bound for spheres settling in a regular cubic array and prove that the Stokes flow for inertia-free sedimenting particles minimizes viscous dissipation [24].

A sharper mathematical analysis is attempted by authors such as Batchelor [2] and Saffman [42], who have been able to analyze random distributions of inclusions as long as their volume concentration is low. The method of Stokesian dynamics described earlier can be applied to sedimentation with the same limitations of porous media flow [5] [15]. Note also that the results presented by Zick & Homsy for porous media are extendible to sedimentation of regular periodic arrays of spheres.

A third approach, is to rely on numerical methods such as finite element [16] and boundary element methods [25] to solve the conservation equations of the system. As mentioned, these approaches are limited by the number of particles that can be modeled.

Experimental verification of theory is complicated by the fact that settling velocity data is hard to obtain. For example, it is difficult to track a particle in highly concentrated suspensions. Moreover, truly monodisperse suspensions are difficult to obtain [20], [14].

1.3 Objectives

In this thesis, we extend the (two-dimensional) fibrous porous media work of Cruz, Ghaddar & Patera [8] to (three-dimensional) particulate media. In addition, we formulate and validate the low Reynolds number sedimentation methodology. Both problems are solved by (i) analyzing a unit periodic cell that contains enough particles to capture the characteristics of the original medium; (ii) bounding the effective

property in cases that are too geometrically stiff. The actual solution procedure relies upon the variational formulation of the problems and subsequent finite-element treatment of the discrete variational equations.

Our methodology overcomes many limitations of previous analytical and numerical studies. First, although we presently analyze highly regular inclusion distributions to validate our methodology, we can readily include random arrangements of particles. Second, we are capable of determining the permeability and settling speed of particulate media of any concentration. Third, although we limit our study to materials consisting of identical spherical inclusions dispersed in a continuous matrix, we can modify our procedure to include non-spherical bodies. Finally, we can include fluid inertia, as done by Ghaddar for two-dimensional fibrous porous media [17].

The main goals of this thesis are:

- Calculate the permeability of simple cubic arrays of spheres and compare the results to known analytical solutions to validate our methodology.
- Develop and implement variational bounding procedures for geometrically stiff porous media problems. This allows us to achieve maximum packing density and compute the fluidization velocity of the regular array.
- Calculate the settling speed of a simple cubic array of spheres and relate it to the permeability results for validation.
- Calculate the settling speed of other periodic arrays of spheres in which a unit cell contains two or three spheres. These problems should provide more *physically* interesting results.
- Develop and implement variational bounding procedures for geometrically stiff sedimentation problems.

Although our methodology can treat statistically random particulate media, we only analyze highly regular particle distributions in order to validate our procedures for inertia-free porous media and sedimentation problems. For this reason we do not

focus on other aspects of our methodology, such as parallel processing and Monte-Carlo methods, which extend directly from the works of Cruz & Patera [9] and Cruz, Ghaddar & Patera [7].

1.4 Outline

This thesis is divided into five chapters. In Chapter 2, the scale decomposition procedure that yields the permeability and the settling speed is presented. In Chapter 3, we develop the bounding procedures for geometrically stiff problems. In Chapter 4, the numerical methods used for the solution of the problems are discussed. In Chapter 5, we present the results of our investigation and draw some conclusions.

Chapter 2

Formulation of Problems

In this chapter we develop the mathematical formulations of the low Reynolds number porous media and sedimentation problems. It should be noted that the scale decomposition procedure of Section 2.1 is discussed in detail by Cruz & Patera [9], and in a more general fashion by Bensoussan, Lions & Papanicolaou [4] and Mei & Auriault [36]. Nevertheless, we discuss this procedure to establish the framework for the formulation of the problems of Sections 2.2 and 2.3. Furthermore, although we concern ourselves with highly regular particulate media, Section 2.1 deals with the more general case of random multicomponent media.

2.1 Scale Decomposition Procedure

As shown in Figure 2-1, our scale decomposition procedure applies to two phase materials that consist of monodisperse spherical inclusions (of volume fraction c) dispersed in a continuous matrix. When, the macroscopic length scale of the medium L is much greater than the sphere diameter d, i.e. $d/L \ll 1$, we are faced with a multi-scale problem which exhibits a clear separation of scales.

In general, one might be interested in predicting the behavior of the material when a known gradient is applied over the macro-scale. For example, if the material is composed of a heat conducting matrix and insulating inclusions, one might need to quantify the heat flow through the material for a given imposed temperature gradient

[9] [13] [33]. However, solving Laplace's equation is often impossible for such multi-scale problems. In fact, modern analytical methods only succeed with simple spatial distributions of the inclusions. Moreover, numerical solutions of multi-scale problems require so much computer time and memory that they are virtually unattainable. Fortunately, by replacing the multi-scale problem with a homogenized medium and the appropriate effective property, the problem has a tractable solution.

In order to use a scale decoupling procedure, we postulate the existence of a joint probability density function (JPDF) that adequately describes the spatial arrangement of the inclusions. Another important assumption is that there exists an intermediate meso-scale length λ ($d < \lambda < L$), that is large enough to capture the statistics of the medium, but small compared to the macro-scale ($\epsilon \equiv \lambda/L \ll 1$) (Figure 2-2). These assumptions allow us to capture the macroscopic properties of the medium by analyzing the tractable meso-scale problem. Through this analysis, the original two phase material can be replaced by a one phase material that has an equivalent effective property. Returning to our heat conduction example, we would solve for the temperature field in a cube of side λ, calculate the effective conductivity [13] [34] [43], and then calculate the heat flux on the homogenized macro-scale for a given temperature gradient using Fourier's law.

Finally, it should be pointed out that in some meso-scale problems two or more inclusions can be so close to each other that the distance separating them is much smaller than d. For such geometrically stiff cases, the meso-scale numerical solution remains difficult. In order to alleviate this problem, we introduce numerically favorable changes in the meso-scale geometry that provide bounds on the effective property of interest.

What follows is a more detailed description of the three scale decoupled problems: the macro- , meso- , micro-scale subproblems.

Macro-scale

The macro-scale subproblem consists of replacing the original multicomponent medium with a homogeneous material having an effective property. One can then calculate

the needed bulk quantity (e.g. heat flux, volume flowrate) by using the appropriate macroscopic phenomenological relation (e.g. Fourier's law, Darcy's law) and the calculated effective property (e.g. conductivity, permeability).

Meso-scale

The meso-scale analysis yields the appropriate effective property. As mentioned earlier, we assume that the statistics of the original medium can be captured by analyzing a periodic unit cube of side λ. At this point, the appropriate transport equations are formulated first in their strong form and, subsequently, in their variational weak form. The latter formulation is the natural one for the finite element method and it allows us to prove bounding procedures for the effective property of interest.

When dealing with random media two other steps must be considered. First, due to the statistical nature of the problem, one needs to compute the mean effective property for a given cell size λ and concentration c. This is accomplished by sampling the JPDF with Monte-Carlo methods. Second, the size of the meso-scale cell needs to be increased until the effective property of interest reaches an asymptotic value (i.e., the cell is large enough to capture the characteristics of the original medium). In practice, this thesis does not deal with random media, so the last two steps do not apply to our analysis. Furthermore, note that the meso-scale subproblem represents the bulk of our computational effort.

Micro-scale

In many instances, particularly when dealing with random media, our numerical procedure might fail due to the proximity of two or more particles. In the worst case, the particles might be so close that a mesh cannot be generated. In less severe cases, an excessive number of degrees-of-freedom are needed to resolve the small gap between the particles: as a consequence, the size of the discretized problem is too large, and the system matrices are ill-conditioned. Our approach is to geometrically modify the nip region (the gap between two close neighbors) to make the problem tractable. In doing so, we are no longer able to precisely calculate the effective property of interest, but

we are able to bound it (typically sharply). A detailed discussion of these nip-element methods is given in the next chapter.

2.2 Creeping Flow through Porous Media

Figure 2-3 represents an example of a porous material. The continuous matrix Ω_{co} consists of an incompressible Newtonian fluid of density ρ_{co} and viscosity μ_{co}. The inclusions Ω_{di} are rigid spheres held fixed in space. The fluid is set in motion by a pressure gradient $\Delta P/L$ that extends over the macroscopic length scale L. Moreover, the Reynolds number based on the average fluid velocity and the diameter of the spheres is negligible.

Macro-scale

The two phase medium can be replaced by a homogeneous material that has an effective permeability κ. Through Darcy's law, one can then relate the macroscopic velocity (and volume flowrate) to the pressure gradient in the following way:

$$< \mathbf{u} >_v = -\frac{1}{\mu_{co}} \underline{\kappa} \cdot < \nabla p >_v , \tag{2.1}$$

where $\mathbf{u}$ is the local fluid velocity vector; $\underline{\kappa}$ is the permeability tensor; ∇p is the local pressure gradient; and $<>_v$ represents a volume average. Obviously, for isotropic materials, $\underline{\kappa}$ is just a scalar quantity.

To calculate the local pressure gradient, one can solve the homogenized steady-state creeping flow equation, which, from Darcy's Law and incompressibility, reads

$$-\frac{\partial}{\partial x_i}\left[\frac{\kappa_{ij}(c(\mathbf{x}))}{\mu_{co}}\frac{\partial p_{ma}}{\partial x_j}\right] = 0 \ \text{ in } \Omega_{ma} , \tag{2.2}$$

where $\mathbf{x} = (x_1, x_2, x_3)$ represents the Cartesian coordinate system of figure 2-3. The Dirichlet and Neumann conditions on the boundaries shown in figure 2-3 read

$$p_{ma} = p_{in} \ \text{ on } \Gamma_{in} , \tag{2.3}$$

$$p_{ma} = p_{out} \text{ on } \Gamma_{out} \,, \tag{2.4}$$

and

$$\frac{\kappa_{ij}}{\mu_{co}} \frac{\partial p_{ma}}{\partial x_j} n_i = 0 \text{ on } \Gamma_w \,, \tag{2.5}$$

where $p_{ma}(\mathbf{x})$ is the macro-scale pressure (which is the pressure field over the homogenized medium); Ω_{ma} is the region occupied by the entire multi-scale medium ($\Omega_{ma} = \Omega_{co} \cup \Omega_{di}$); Γ_{in} , Γ_{out} and Γ_w are the inflow, outflow and wall boundaries respectively; $\underline{\kappa} \equiv \kappa_{ij}(c)$, $i, j = 1, 2, 3$, is the permeability tensor–concentration function; $\mathbf{n} = n_i$ denotes the unit outward normal to the fluid; and the summation convention over repeated indices is assumed. In general, the problem defined by (2.2) – (2.5) is solvable with the aid of commercial software packages. The reader should note that henceforth we deal only with isotropic materials, so that we only consider an effective *scalar* permeability κ.

Meso-scale

In order to solve problem (2.2)-(2.5), one needs the effective permeability, which is produced by the meso-scale analysis. As shown in Figure 2-4, we extract a periodic unit cell of size λ that contains N spheres and solve the appropriate meso-scale Stokes equations. To arrive at the governing equations, we assume that the pressure solution for the original multi-phase problem can be written as (Mei & Auriault [36])

$$p_{orig}(\mathbf{x}, \mathbf{y}) \;=\; p_{ma}(\mathbf{x}) \;+\; \epsilon\, p(\mathbf{x}, \mathbf{y}) \;+\; O(\epsilon^2) \,, \tag{2.6}$$

where $p_{ma} = -\frac{\Delta P}{L} x_1$; $\epsilon = \lambda / L \ll 1$; p is the periodic perturbation component of p_{orig}; and $\mathbf{y} \equiv \mathbf{x}/\epsilon$ is the rapidly varying coordinate of figure 2-4. Plugging (2.6) into the Stokes equations for the original two phase problem, we arrive at

$$-\frac{\partial}{\partial y_j}(\mu_{co} \frac{\partial u_i}{\partial y_j}) + \frac{\partial p}{\partial y_i} = \frac{\Delta P}{L} \delta_{1i} \text{ in } \Omega_{me} \text{ for } i = 1, 2, 3 \,, \tag{2.7}$$

$$-\frac{\partial u_i}{\partial y_i} = 0 \text{ in } \Omega_{me} \,, \tag{2.8}$$

where δ_{ij} is the Kronecker delta; and Ω_{me} is the fluid region of the meso-scale cell. Clearly, this equation shows that, on the meso-scale, the macroscopic pressure gradient is seen as a forcing term. The no–slip Dirichlet and periodic boundary conditions are

$$\mathbf{u} = 0 \ \text{ on } \partial\Omega_{me} \,, \tag{2.9}$$

and

$$\mathbf{u}(\mathbf{y}) = \mathbf{u}(\mathbf{y} + \lambda(m_1\mathbf{e}_1 + m_2\mathbf{e}_2 + m_3\mathbf{e}_3)) \ \text{ on } \partial\Omega_{\#} \,, \tag{2.10}$$

$$p(\mathbf{y}) = p(\mathbf{y} + \lambda(m_1\mathbf{e}_1 + m_2\mathbf{e}_2 + m_3\mathbf{e}_3)) \ \text{ on } \partial\Omega_{\#} \,, \tag{2.11}$$

where $(\mathbf{e}_1, \mathbf{e}_2, \mathbf{e}_3)$ are the unit vectors of the coordinate system (y_1, y_2, y_3); y_1 is the arbitrarily chosen direction for the driving pressure gradient; $\partial\Omega_{me}$ and $\partial\Omega_{\#}$ are the fluid-particle and periodic meso-scale cell boundaries respectively; and m_1, m_2, m_3 are integers. Since adding a constant to the pressure solution yields another solution we require, for uniqueness, that

$$\int_{\Omega_{me}} p \, d\mathbf{y} \ = \ 0 \,, \tag{2.12}$$

where $d\mathbf{y} \ = \ dy_1 dy_2 dy_3$.

We non-dimensionalize the pressure by $\Delta P \frac{d}{L}$, the velocity by $\frac{\Delta P d^2}{\mu_{co} L}$, and the lengths by d. (From this point to the end of the section, all quantities are implicitly non-dimensional.) As a result, (2.7) and (2.8) become

$$-\frac{\partial^2 u_i}{\partial y_j \partial y_j} + \frac{\partial p}{\partial y_i} = \delta_{1i} \ \text{ in } \Omega_{me} \ \text{ for } i = 1, 2, 3 \,, \tag{2.13}$$

$$-\frac{\partial u_i}{\partial y_i} = 0 \ \text{ in } \Omega_{me} \,. \tag{2.14}$$

The dimensionless permeability κ (which is non-dimensionalized by d^2), is derived by using (2.1), recognizing that $< \nabla p >_v \ = \ -\frac{\Delta P}{L} \, \mathbf{e}_1$ and that $< \mathbf{u} >_v \ = \ \frac{1}{\lambda^3} \int_{\Omega_{me}} u_1 d\mathbf{y}$, since $< u_2 >_v = < u_3 >_v \ = \ 0$ due to periodicity. The result is

$$\kappa = \frac{1}{\lambda^3} \int_{\Omega_{me}} u_1 d\mathbf{y} \,. \tag{2.15}$$

At this point, we pursue the variational statement of the meso-scale problem. Helmholtz's minimum dissipation theorem states that flow with negligible inertia has a smaller rate of dissipation than any other incompressible velocity field compatible with the boundary conditions of the problem. Mathematically, for the porous media problem, we have

$$\mathbf{u} = \arg\min_{\mathbf{v}\in Z}(-J^P_\Omega(\mathbf{v})) = \arg\max_{\mathbf{v}\in Z} J^P_\Omega(\mathbf{v}) \,, \tag{2.16}$$

where

$$J^P_\Omega(\mathbf{v}) = 2\int_\Omega v_1 d\mathbf{y} - \int_\Omega \frac{\partial v_i}{\partial y_k}\frac{\partial v_i}{\partial y_k} d\mathbf{y} \,, \tag{2.17}$$

and

$$Z = \{(v_1, v_2, v_3) \in (H^1_{0\#}(\Omega_{me}))^3 \mid div\, \mathbf{v} = 0\} \,, \tag{2.18}$$

where $H^1_{0\#}(\Omega_{me})$ is the space of all square-integrable functions that vanish on $\partial\Omega_{me}$, are periodic (of period λ), and whose derivatives are square-integrable over Ω_{me}. By multiplying (2.13) by $\mathbf{u}$, integrating over Ω_{me}, and using the divergence theorem along with (2.14), we arrive at

$$\int_{\Omega_{me}} u_1 d\mathbf{y} = J^P_{\Omega_{me}}(\mathbf{u}) = \int_{\Omega_{me}} \frac{\partial u_i}{\partial y_j}\frac{\partial u_i}{\partial y_j} d\mathbf{y} \,, \tag{2.19}$$

which states that

$$\kappa = \frac{1}{\lambda^3} J^P_{\Omega_{me}}(\mathbf{u}) \,. \tag{2.20}$$

The permeability is thus always non-negative, and is proportional to the maximum value of the functional $J^P_{\Omega_{me}}$. In fact, from (2.16) and (2.20) it follows that

$$\kappa = \frac{1}{\lambda^3} \max_{\mathbf{v}\in Z} J^P_{\Omega_{me}}(\mathbf{v}) \,. \tag{2.21}$$

In order to arrive at the appropriate velocity field $\mathbf{u}$, we transform the constrained maximization problem of (2.16) into an unconstrained saddle-problem by introducing

a Lagrange multiplier q to impose the incompressibility constraint. We have the Lagrangian L^P_Ω,

$$L^P_\Omega(\mathbf{v}, q) \;=\; J^P_\Omega(\mathbf{v}) + \int_\Omega q \frac{\partial v_i}{\partial y_i} d\mathbf{y}\,. \tag{2.22}$$

By taking the first variation of the Lagrangian, and setting it equal to zero for stationarity, we look for a solution $(\mathbf{u}, p) \in \{(H^1_{0\#}(\Omega_{me}))^3, L^2_{\#,0}(\Omega_{me})\}$ that satisfies

$$\int_{\Omega_{me}} \frac{\partial v_i}{\partial y_j}\frac{\partial u_i}{\partial y_j}\, d\mathbf{y} - \int_{\Omega_{me}} \frac{\partial v_i}{\partial y_i}\, p\, d\mathbf{y} = \delta_{1i}\int_{\Omega_{me}} v_i\, d\mathbf{y} \quad \forall (v_1, v_2, v_3) \in (H^1_{0\#}(\Omega_{me}))^3\,, \tag{2.23}$$

$$-\int_{\Omega_{me}} q\,\frac{\partial u_i}{\partial y_i}\, d\mathbf{y} = 0 \quad \forall q \in L^2_{\#,0}(\Omega_{me})\,, \tag{2.24}$$

where $L^2_{\#,0}(\Omega_{me})$ is the space of all λ-triply periodic functions $q(\mathbf{y})$ which are square–integrable over Ω_{me} (note that candidate pressures need not be continuous), and for which $\int_{\Omega_{me}} q\, d\mathbf{y} = 0$. Note that solving (2.23) and (2.24) for $\mathbf{u}$ and p is equivalent to solving the strong form of the porous media problem (2.13), (2.14), which, together with the negative-definiteness of the quadratic part of J^P_Ω, proves (2.16). Indeed, multiplying (2.13) by $\mathbf{v}$ and integrating by parts over Ω_{me} we get (2.23). Similarly, by multiplying (2.14) by q and integrating over Ω_{me} we obtain (2.24) [6].

Equations (2.23) and (2.24) constitute the meso-scale subproblem that is solved to yield the permeability as defined in (2.15).

Micro-scale

In order to successfully solve a geometrically stiff meso-scale problem, we choose to replace the nip region with very simple models that provide us with lower and upper bounds for the permeability. In short, we argue that a lower bound can be achieved by blocking the flow through the nip region, whereas an upper bound is achieved by facilitating the flow between two close neighbors (i.e., by enlarging the nip region). A complete discussion of these bounds is provided in Section 3.1.

2.3 Low-Reynolds-Number Sedimentation

Figure 2-5 is a schematic of particles settling under gravity. As in Section 2.2, the continuous matrix consists of an incompressible Newtonian fluid of density ρ_{co} and viscosity μ_{co}. The inclusions are non-colloidal monodisperse spheres of density ρ_{di} ($> \rho_{co}$) that settle under the action of gravity. We assume that inertia plays no role in the fluid and particle motions. Moreover, we require that the particle and fluid motions are quasi-static. This means that if the system is perturbed it quickly reaches a new equilibrium without the particles rearranging themselves considerably. The conditions for this are

$$V_p\theta_p \ll d \qquad \text{and} \qquad V_p\theta_f \ll d\,, \tag{2.25}$$

where V_p is the characteristic speed of a particle (i.e. the Stokes settling speed); θ_p and θ_f are the characteristic particle and fluid times, respectively; and d is the sphere diameter. θ_p can be estimated as $(d^2\frac{\rho_{di}}{\mu_{co}})$ and θ_f as $(l^2\frac{\rho_{co}}{\mu_{co}})$, where l is the characteristic inter-particle distance. θ_p is the time constant associated with the exponential decay of the velocity of a sphere in an unbounded fluid whose motion is retarded by Stokes drag. Using the expression for θ_p we can rewrite the first condition of (2.25) as $Re_p \ll 1$, where $Re_p = \frac{\rho_{di}V_p d}{\mu_{co}}$ is the particle Reynolds number. The second condition of (2.25) can be restated as $Re_f \ll 1$, where $Re_f = \frac{\rho_{co}V_p l^2}{\mu_{co}d}$ is the fluid Reynolds number. In other words, the quasi-static assumption is fulfilled by sedimenting suspensions for which the two Reynolds numbers, Re_p and Re_f, are negligible. This is equivalent to the assumption of inertia-free fluid and particle motions. The quasi-static assumption allows us to replace the self consistent motion of the suspension with a JPDF that we sample by taking "snapshots" of the system, as proposed by Batchelor [2].

As shown in figure 2-5, when a suspension is sedimenting in a container three distinct regions of different particle concentration are observed. The upper clarified region consists of fluid with no particles; the lower compression zone is where the particles accumulate; and the middle region is the suspension filled sub-domain. We

focus our attention on the latter region. Note that since the settling process occurs in a closed tank, we require zero net (fluid and particle) volume flowrate at any horizontal surface [31].

In general, when tackling a sedimentation problem, we would assume a JPDF for the particle distribution and find a statistically steady-state settling speed. However, as discussed in Chapter 5, we limit ourselves to a maximum of three particles in a meso-scale cell to validate our methodology.

Macro-scale

Our homogeneous, quasi-static, quantity of interest is the average sedimentation speed (or settling rate), $\mathcal{U}$. Since this quantity defines our macro-scale subproblem, we pass directly to the meso-scale formulation. It should be noted that for other suspension flows the macro-scale problem is more complex. For example, for duct flow of particulate suspensions, we need to model the flow of a homogenized fluid with an effective viscosity.

Meso-scale

As in Figure 2-4, we extract a unit periodic cell of size λ that contains N spheres. Again, we derive the meso-scale equations from the Stokes equations that govern the flow in the original multi-scale medium, which are as follow,

$$-\frac{\partial}{\partial x_j}\left[\mu_{co}\left(\frac{\partial u_i}{\partial x_j}+\frac{\partial u_j}{\partial x_i}\right)\right]+\frac{\partial p}{\partial x_i}+\rho_{co}g\delta_{2i}\mathbf{e}_i=0 \quad \text{in } \Omega_{orig} \text{ for } i=1,2,3\,, \tag{2.26}$$

$$-\frac{\partial u_i}{\partial x_i}=0 \quad \text{in } \Omega_{orig}\,, \tag{2.27}$$

where g is the acceleration of gravity which acts in the $-\mathbf{e}_2$ direction; and Ω_{orig} is the fluid region in the original multi-scale problem. Note that instead of using the usual Laplacian operator on the velocity in (2.26) we use an equivalent "stress formulation", which allows us to incorporate the boundary conditions naturally in our variational

weak form.

On the meso-scale, the pressure can be written as $p = p_0 - \rho_{co} g y_2 - \tau y_2 + p'(\mathbf{y})$, where p_0 is a reference pressure, τ is the (positive) fluid "backflow" pressure gradient, and $p'(\mathbf{y})$ is the periodic perturbation pressure. The "backflow" pressure gradient results from imposing zero volume flowrate. In fact, it can be viewed as the pressure gradient responsible for the upward movement of fluid as the particles settle. Plugging the expression for p in (2.26), we arrive at the meso-scale Stokes equations,

$$-\frac{\partial}{\partial y_j}\left[\mu_{co}\left(\frac{\partial u_i}{\partial y_j}+\frac{\partial u_j}{\partial y_i}\right)\right]+\frac{\partial p'}{\partial y_i}-\tau\,\delta_{2i}=0 \quad \text{in } \Omega_{me} \text{ for } i=1,2,3\,, \tag{2.28}$$

$$-\frac{\partial u_i}{\partial y_i}=0 \quad \text{in } \Omega_{me}\,. \tag{2.29}$$

The zero net flowrate requirement is expressed as,

$$-\left(\int_{\Omega_{me}} u_2\, d\mathbf{y}+\frac{\pi d^3}{6}\sum_{k=1}^{N}(U_2)_k\right)=0\,, \tag{2.30}$$

where $\mathbf{U}_k$ is the translational velocity vector of particle $k = 1, .., N$. Equation (2.30) can be obtained by writing the zero net flowrate condition at a $y_2 = constant$ surface of the meso-scale cell and integrating it from $y_2 = 0$ to $y_2 = \lambda$. We also require for uniqueness that

$$\int_{\Omega_{me}} u_1 d\mathbf{y} = \int_{\Omega_{me}} u_3 d\mathbf{y} = 0\,, \tag{2.31}$$

and

$$\int_{\Omega_{me}} p' d\mathbf{y} = 0\,. \tag{2.32}$$

Turning now to boundary conditions, the no-slip boundary condition must be consistent with solid body translation and rotation of the spheres such that

$$\mathbf{u}|_{\partial\Omega_k} = \mathbf{U}_k + \mathbf{W}_k \times (\mathbf{y}-\mathbf{y}_k)\,, \quad k=1,\ldots,N\,, \tag{2.33}$$

where $\partial\Omega_k$ is the surface of sphere k; $\mathbf{W}_k$ is the rotational velocity vector of particle k; $() \times ()$ denotes the cross product; and $\mathbf{y}_k$ denotes the center (of mass) of sphere k. An additional requirement on $\mathbf{u}$ is that it must be λ-triply periodic. Our quasi-static analysis also requires zero net force on each particle, which can be written as

$$\int_{\partial\Omega_k} (\mathbf{T}' : \mathbf{n})\, ds \;=\; \left(\tau\,\frac{\pi d^3}{6} - \mathcal{W}\right)\mathbf{e}_2\,, \quad k = 1, \ldots, N\,, \tag{2.34}$$

where $T'_{ij} = \mu_{co}(\partial u_i/\partial y_j + \partial u_j/\partial y_i) - p'\delta_{ij}$ is the "perturbation" stress tensor; $(\mathbf{T}' : \mathbf{n}) = T'_{ij}\, n_j$; and $\mathcal{W} = (\rho_{di} - \rho_{co})g\pi d^3/6$ is the buoyancy corrected weight of a sphere, which accounts for the hydrostatic pressure gradient $-\rho_{co}g\mathbf{e}_2$ since only p' is included in $\mathbf{T}'$. So (2.34) requires that, for each particle, the integral of the surface stresses described by the stress tensor T'_{ij} be in equilibrium with the buoyancy corrected weight and the additional buoyancy created by the backflow pressure gradient. Finally, we require zero net torque on each sphere, which reads

$$\int_{\partial\Omega_k} (\mathbf{y} - \mathbf{y}_k) \times (\mathbf{T}' : \mathbf{n})\, ds \;=\; 0\,, \quad k = 1, \ldots, N\,. \tag{2.35}$$

Note that τ and $(\mathbf{U}_k\,, \mathbf{W}_k)$ are not specified, but, rather, are part of the solution. In essence, the zero net volume flux and particle force equilibrium equations, (2.30) and (2.34)–(2.35), respectively, are the complementary conditions from which the backflow gradient and particle velocities can be deduced. The strong–form equations (2.28)–(2.35) are the point of departure from Batchelor's analysis [2].

In the sedimentation problem, the effective property of interest is the average settling speed of the particles which, by virtue of horizontal ($x_1 - -x_3$ plane) homogeneity, is defined as

$$\mathcal{U} \equiv \frac{1}{N\mathcal{W}}\, I^S_{\Omega_{me}}(\mathbf{u})\,, \tag{2.36}$$

where, for $\mathbf{v}$ satisfying $\mathbf{v}|_{\partial\Omega_k} = \mathbf{V}_k + \mathbf{Z}_k \times (\mathbf{y} - \mathbf{y}_k)$,

$$I^S_\Omega(\mathbf{v}) \;=\; -\mathcal{W} \sum_{k=1}^{N} (V_2)_k\,. \tag{2.37}$$

We also introduce the dissipation functional $J^S_\Omega(\mathbf{v})$,

$$J^S_\Omega(\mathbf{v}) = 2\, I^S_\Omega(\mathbf{v}) - \mu_{co}\frac{1}{2}\int_\Omega \left(\frac{\partial v_i}{\partial y_j} + \frac{\partial v_j}{\partial y_i}\right)\left(\frac{\partial v_i}{\partial y_j} + \frac{\partial v_j}{\partial y_i}\right) d\mathbf{y}\,. \tag{2.38}$$

By multiplying equation (2.28) by $\mathbf{u}$, integrating by parts over Ω_{me}, and using (2.29)–(2.35), we derive (see Appendix A for details)

$$I^S_{\Omega_{me}}(\mathbf{u}) = J^S_{\Omega_{me}}(\mathbf{u}) = \mu_{co}\frac{1}{2}\int_{\Omega_{me}} \left(\frac{\partial u_i}{\partial y_j} + \frac{\partial u_j}{\partial y_i}\right)\left(\frac{\partial u_i}{\partial y_j} + \frac{\partial u_j}{\partial y_i}\right) d\mathbf{y}\,. \tag{2.39}$$

From (2.36) and (2.39) it is clear that the average settling velocity $\mathcal{U}$ is always positive.

As for the creeping flow problem, we can prove that (see Appendix A)

$$\mathbf{u} = \arg\max_{\mathbf{v}\in B} J^S_{\Omega_{me}}(\mathbf{v})\,, \tag{2.40}$$

where

$$B = \left\{\mathbf{v}\in Y \mid \operatorname{div}\mathbf{v} = 0\,,\ \int_{\Omega_{me}} v_2\, d\mathbf{y} - \frac{\pi d^3}{6\mathcal{W}}\, I^S(\mathbf{v}) = 0\right\}\,, \tag{2.41}$$

and

$$Y = \Big\{(v_1, v_2, v_3)\in (H^1_\#(\Omega_{me}))^3 \ \mid\ \int_{\Omega_{me}} v_1\, d\mathbf{y} = 0\,, \int_{\Omega_{me}} v_3\, d\mathbf{y} = 0\,,$$
$$\text{and } \forall k\in\{1,\ldots,N\}, \mathbf{v}|_{\partial\Omega_k} = \mathbf{V}_k + \mathbf{Z}_k \times (\mathbf{y}-\mathbf{y}_k), \mathbf{V}_k\in\mathcal{R}^3, \mathbf{Z}_k\in\mathcal{R}^3\Big\}\,.$$

From (2.36), (2.39), and (2.40) we can derive the following expression for the settling velocity,

$$\mathcal{U} = \frac{1}{N\mathcal{W}}\max_{\mathbf{v}\in B} J^S_{\Omega_{me}}(\mathbf{v})\,. \tag{2.42}$$

Related variational expressions for the sedimentation problem can be found in Hill & Power [24]; Keller, Rubenfeld & Molyneux [28]; and Kim & Karrila [30]. Related extremum statements for the settling velocity can be found in Keller, Rubenfeld & Molyneux [28]. In order to arrive at (2.40), we multiply (2.28) by the test function $\mathbf{v}\in B$, and integrate over Ω_{me}. By integrating by parts, using (2.34), (2.35) and the attributes of the space B, we obtain that the first variation of $J^S_{\Omega_{me}}(\mathbf{u})$ is equal to

zero. Since the second variation is always negative, we are extremizing $J^S_{\Omega_{me}}(\mathbf{v})$ as described in (2.40) (see Appendix A).

Similarly to the previous section, we proceed by converting the constrained maximization problem into an unconstrained extremization problem by introducing a Lagrangian L^S_Ω,

$$L^S_\Omega(\mathbf{v}, q, \eta) \;=\; -\frac{1}{2} J^S_\Omega(\mathbf{v}) - \int_\Omega q \frac{\partial v_i}{\partial y_i} d\mathbf{y} - \eta \left[\int_\Omega v_2 d\mathbf{y} - \frac{\pi d^3}{6\mathcal{W}} I^S_\Omega(\mathbf{v}) \right], \tag{2.43}$$

where $\mathbf{v} \in Y$, $q \in L^2_{\#,0}(\Omega)$, and $\eta \in \mathcal{R}$. Taking the first variation of the Lagrangian and setting it equal to zero, we find that $(\mathbf{u}, p', \tau) \in (Y, L^2_{\#,0}(\Omega), \mathcal{R})$ is a stationary point. Moreover, it maximizes the functional J^S_Ω with respect to solenoidal admissible velocity fields. The variational weak form is thus

$$\begin{aligned} \mu_{co} \int_{\Omega_{me}} \frac{\partial v_i}{\partial y_j} \left(\frac{\partial u_i}{\partial y_j} + \frac{\partial u_j}{\partial y_i} \right) d\mathbf{y} \;-\; & \int_{\Omega_{me}} p' \frac{\partial v_i}{\partial y_i} d\mathbf{y} - \tau \left[\int_{\Omega_{me}} v_2 \, d\mathbf{y} - \frac{\pi d^3}{6\mathcal{W}} I^S(\mathbf{v}) \right] \\ & = \; I^S(\mathbf{v}) \quad \forall \mathbf{v} \in Y \,, \end{aligned} \tag{2.44}$$

$$- \int_{\Omega_{me}} q \frac{\partial u_i}{\partial y_i} d\mathbf{y} \;=\; 0 \quad \forall q \in L^2_{\#,0}(\Omega_{me}) \,, \tag{2.45}$$

$$- \eta \left[\int_{\Omega_{me}} u_2 \, d\mathbf{y} - \frac{\pi d^3}{6\mathcal{W}} I^S(\mathbf{u}) \right] \;=\; 0 \quad \forall \eta \in \mathcal{R} \,. \tag{2.46}$$

Note that solving (2.44)- (2.46) for $\mathbf{u}$, p and τ is equivalent to solving the strong form of the problem (2.28)- (2.35). Indeed, multiplying (2.28) by $\mathbf{v} \in Y$ and integrating by parts over Ω_{me} we get (2.44). Similarly, by multiplying (2.29) by $q \in L^2_{\#,0}$ and integrating over Ω_{me} we obtain (2.45). Lastly, (2.46) results from multiplying (2.30) by $\eta \in \mathcal{R}$. It is important to notice that the zero net force and torque requirements of (2.34) and (2.35) appear as *natural* boundary conditions in the variational formulation of the sedimentation problem (see Appendix A). This constitutes a great advantage for the numerical implementation of this method.

Choosing $\mathbf{v} = (0, 1, 0) \in Y$, we derive from (2.44) that τ is given by

$$\tau = \frac{N\mathcal{W}}{\mathcal{V}_{tot}}, \tag{2.47}$$

where $\mathcal{V}_{tot} = (N\pi d^3/6 + \int_{\Omega_{me}} d\mathbf{y}) = \lambda^3$ is the total volume of the meso-scale cell. Note that we have determined one of the unknowns of the problem, so it seems we have too many equations. However, from a mathematical viewpoint, (2.44)-(2.46) are all necessary. In fact, (2.44) is not solvable without τ (try $\mathbf{v} = (0, 1, 0) \in Y$). Although we have determined τ, which is associated with the Lagrange multiplier η, we still need (2.46) to prevent the velocity solution u_2 from floating, that is, ensuring that $(u_2 + constant)$ is not a solution. Note that both the sedimentation problem and the porous media problem have unique solutions since they are positive-definite problems.

The backflow pressure gradient τ depends only on the buoyancy corrected weight and concentration of the particles, not on their spatial distribution. This can be understood by carrying out a y_2-momentum balance for a control volume that consists of the meso-scale cell. It is clear that the hydrostatic pressure distribution balances the weight of the fluid and is responsible for the buoyant forces on the particles. The only other surface force that can balance the buoyancy corrected weight of the inclusions $N\mathcal{W}$ is, therefore, $\tau\mathcal{V}_{tot}$. So that, indeed, $N\mathcal{W} = \tau\mathcal{V}_{tot}$ as claimed in (2.47).

Lastly, the variational weak form should be non-dimensionalized. The velocities are non-dimensionalized by $\frac{(\rho_{di}-\rho_{co})gd^2}{\mu_{co}}$; the pressure by $(\rho_{di} - \rho_{co})gd$; and lengths by d. The resulting non-dimensional equations are:

$$\int_{\Omega_{me}} \frac{\partial v_i}{\partial y_j}\left(\frac{\partial u_i}{\partial y_j} + \frac{\partial u_j}{\partial y_i}\right) d\mathbf{y} \; - \; \int_{\Omega_{me}} p' \frac{\partial v_i}{\partial y_i} d\mathbf{y} - c\left[\int_{\Omega_{me}} v_2 d\mathbf{y} + \frac{\pi}{6}\sum_{k=1}^{N}(V_2)_k\right]$$
$$= \; -\frac{\pi}{6}\sum_{k=1}^{N}(V_2)_k \quad \forall \mathbf{v} \in Y\,, \tag{2.48}$$

$$-\int_{\Omega_{me}} q\frac{\partial u_i}{\partial y_i} d\mathbf{y} \; = \; 0 \quad \forall q \in L^2_{\#,0}(\Omega_{me})\,, \tag{2.49}$$

$$-\eta\left[\int_{\Omega_{me}} u_2 d\mathbf{y} + \frac{\pi}{6}\sum_{k=1}^{N}(U_2)_k\right] \; = \; 0 \quad \forall \eta \in \mathcal{R}\,, \tag{2.50}$$

where $c = \frac{N\pi d^3}{6\lambda^3}$ is the sphere volume fraction.

Equations (2.36) and (2.48)-(2.50) constitute the sedimentation meso-scale problem that is solved numerically.

Micro-scale

As discussed for the porous media problem, the methodology can be hindered by excessively disparate length scales within the meso-scale. When two or more spheres are too close to each other, we replace the nip region with simple models that yield lower and upper bounds for the average settling speed. A lower bound is achieved by rigidly connecting a pair of particles with a cylindrical connection; an upper bound is achieved by shrinking the spheres while keeping their buoyancy corrected weight constant. A complete discussion of these methods is presented in Section 3.2.

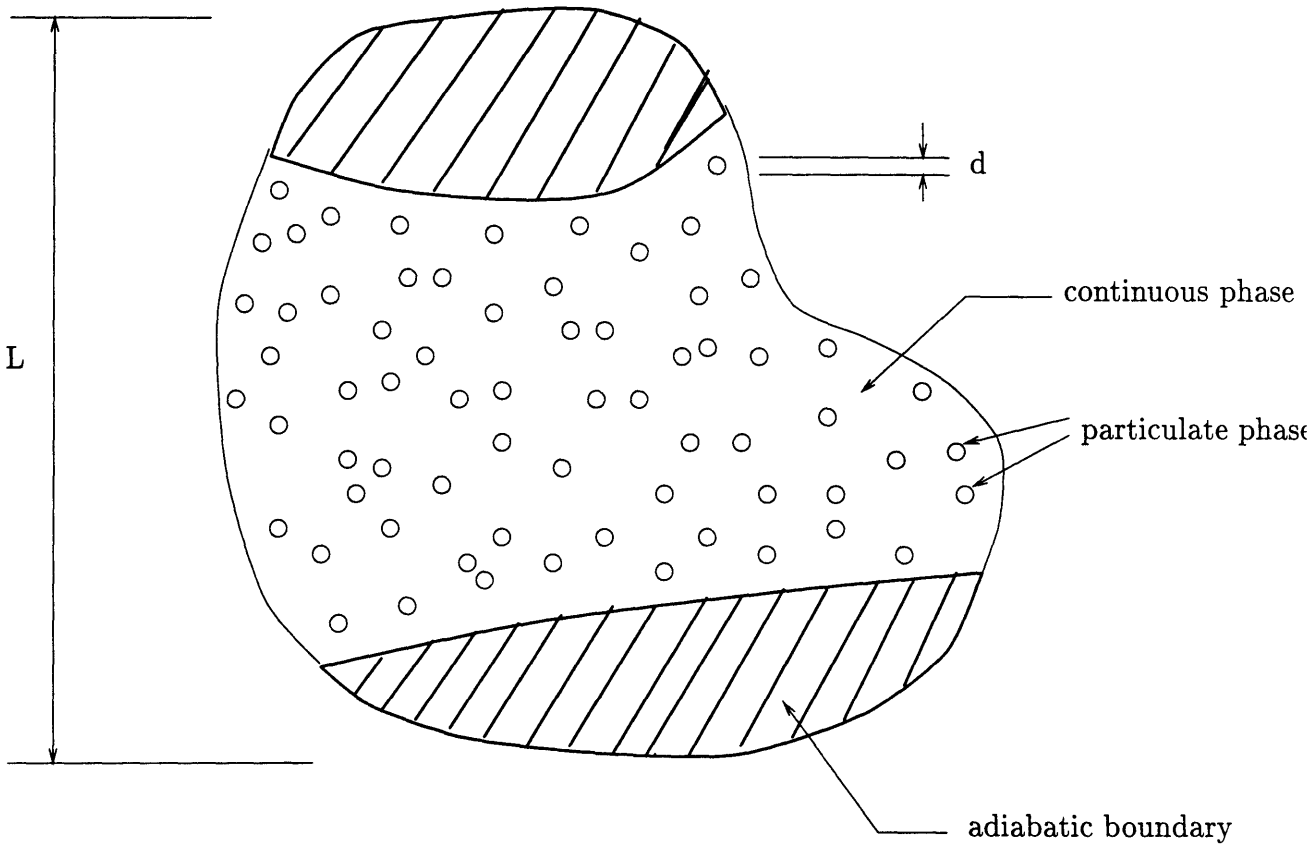

Figure 2-1: The original multi-scale problem.

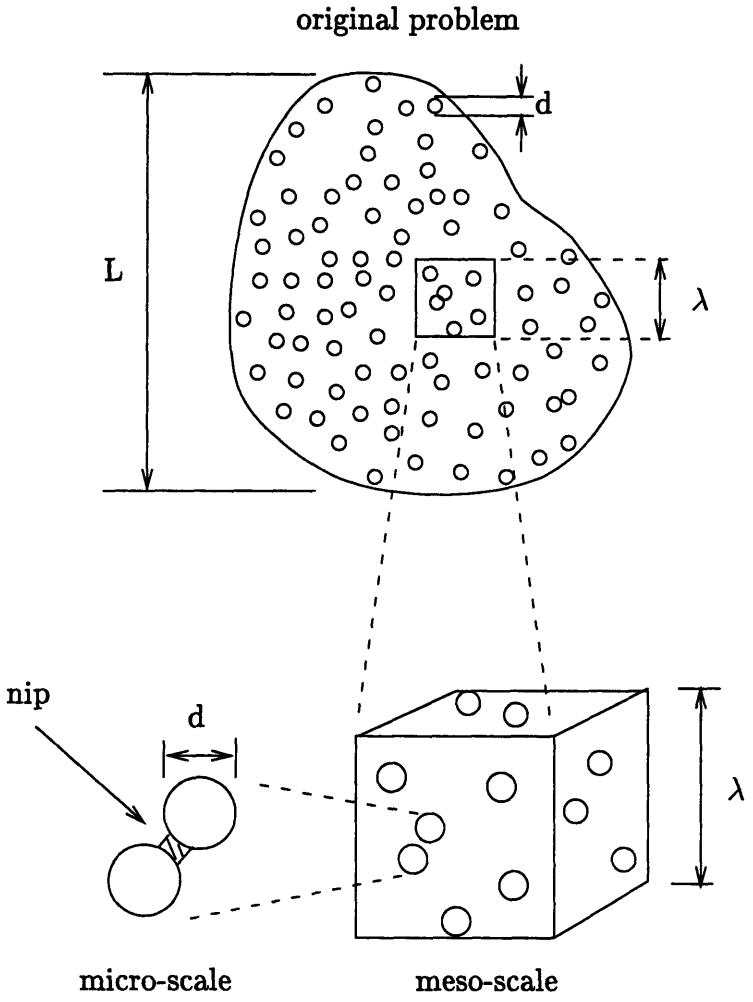

Figure 2-2: Decomposition of the original multi-scale problem.

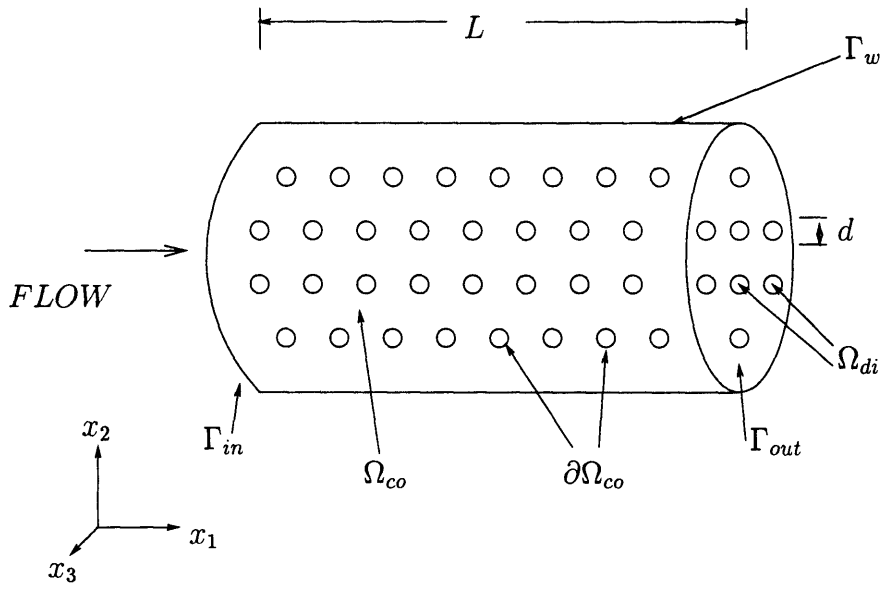

Figure 2-3: An example of porous media flow: flow in a duct.

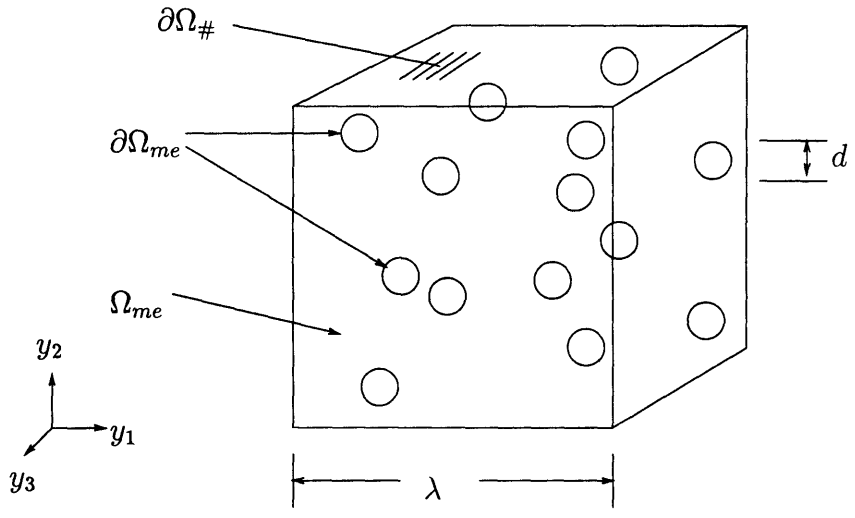

Figure 2-4: Meso-scale cell.

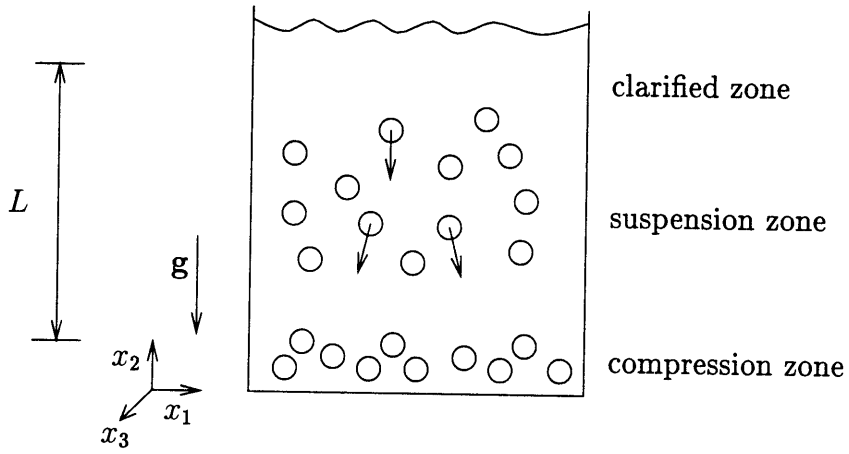

Figure 2-5: Batch particle Stokes sedimentation.

Chapter 3

Variational Bounds: Micro-Scale Problem

In general, the micro-scale analysis can be of two types: the modeling of interfacial phenomena between the inclusions and the continuous matrix; and the development of bounding procedures that alleviate the geometrical stiffness present when two or more inclusions are very close to each other. The former is important in cases such as thermal conduction in composites with significant contact resistance between the two phases, or in fluid flow problems where the inclusions are drops or bubbles that are contaminated by surfactants. In our study the inclusions are solid spheres, so interfacial phenomena are irrelevant.

As discussed earlier, our meso-scale analysis may be hindered by the proximity of two or more spheres. In order to circumvent the problem, a variational-bound methodology is introduced: we simply modify the geometry of the meso-scale problem and prove that such modification bounds the effective property of interest. The proofs are based on the extremizing properties of the scalar permeability κ and the average settling speed $\mathcal{U}$. Once the bounds are established, we show what modifications, if any, need to be made to the original meso-scale formulation to include the bounds. Note that our micro-scale analysis does not approximate the fluid flow in the nip region very well; however, it can provide reasonably sharp bounds on the macroscopic scale (i.e., the effective property). Moreover, the proofs rely on previously used variational

techniques of space restriction and expansion [24] [28].

In Section 3.1 we present the bound proofs for the porous media problem: we discuss the lower bound in Section 3.1.1 and the upper bound in Section 3.1.2. The proofs are, at first, for a pair of particles, then they are generalized to clusters of many particles which is important if we want to analyze close-packed geometries. Section 3.2 follows a similar logic for the sedimentation bounds, although the variational meso-scale formulation needs to be modified.

3.1 Porous Media Problem

Figure 3-1 shows the simple geometric modifications proposed for the porous media case. To obtain a lower bound, the two spheres are connected with a solid cylinder whose axis coincides with the line of centers (figure 3-1a). The modified fluid region $\mathcal{C}$ is now the old fluid region Ω minus the nip region $\mathcal{D}$ ($\mathcal{C} = \Omega \setminus \mathcal{D}$). Figure 3-1b depicts the upper bound geometry, which consists of two shaved spheres. In this case, the fluid region $\mathcal{C}$ occupies region $\mathcal{D}$ as well as the old domain Ω ($\mathcal{C} = \Omega \cup \mathcal{D}$). The porous media proofs follow the arguments made by Cruz, Ghaddar & Patera [8] for two-dimensional porous media (i.e. cylinders in a cross-flow).

3.1.1 Lower Bound

Physically the lower bound is achieved by blocking the flow between selected particle pairs; mathematically the proof is based on variational arguments. The following proof is for a meso-scale comprised of N spheres, only two of which are considered for the micro-scale treatment. We define three motions (figure 3-2): motion 1 corresponds to the solution of the original geometrically stiff problem over the fluid region Ω; motion 2 corresponds to the solution over the modified geometry $\mathcal{C}$; and motion 3 corresponds to the velocity field of motion 2 and the geometry of motion 1 (we remove region $\mathcal{D}$ and replace it with fluid at rest). The velocity field of motion 3 ($\mathbf{u}^{(3)}$) is an admissible, but non-maximizing, candidate to the porous media problem (2.16)-(2.18) defined over the region Ω. To show this, we need to prove that $\mathbf{u}^{(3)} \in Z$ over

Ω as defined in (2.18) (with Ω_{me} replaced by Ω). Indeed, $\mathbf{u}^{(3)}$ is an incompressible, periodic continuous function which vanishes at the sphere surfaces. So for the fluid region Ω we can say that

$$J_{\Omega}^{P}(\mathbf{u}^{(1)}) \geq J_{\Omega}^{P}(\mathbf{u}^{(3)}), \tag{3.1}$$

where $\mathbf{u}^{(1)}$ is the velocity solution of motion 1. Furthermore, motions 2 and 3 produce the same amount of viscous dissipation, since the quiescent fluid in region $\mathcal{D}$ of motion 3 does not dissipate energy. It follows that

$$J_{\mathcal{C}}^{P}(\mathbf{u}^{(2)}) = J_{\Omega}^{P}(\mathbf{u}^{(3)}), \tag{3.2}$$

where $\mathbf{u}^{(2)}$ is the velocity solution of motion 2 which maximizes $J_{\mathcal{C}}^{P}(\mathbf{v})$, $\mathbf{v} \in Z$ over $\mathcal{C}$. From (3.1), (3.2), and the extremum statement of (2.21) we can write

$$\kappa_{LB} \leq \kappa, \tag{3.3}$$

where κ_{LB} is given by the solution of motion 2; and κ is the permeability of motion 1.

Although we have not said anything about the size of region $\mathcal{D}$, it can be shown that by decreasing the radius of the nip region a sharper bound is obtained. Moreover, the above proof readily extends to multiple nips and the bound gets more crude as the number of nips increases for a given geometry and nip radius. In general, the lower bound proof relies on the simple argument of space restriction: we are restricting the candidate functions to have a value of zero over $\mathcal{D}$, so the maximum value of J^P over the restricted class of functions cannot be greater than the original maximum of motion 1.

3.1.2 Upper Bound

The physical argument in favor of the proposed nip-enlargement technique is that the new geometry enhances the flow through the nip. We prove this mathematically for a pair of spheres in a meso-scale comprised of N spheres. As for the lower bound proof,

envision three motions (figure 3-3): motion 1 consists of the solution of the original meso-scale problem in region Ω; motion 2 is the solution of the porous media problem over the modified geometry $\mathcal{C} = \Omega \cup \mathcal{D}$; and motion 3 consists of the fluid geometry $\mathcal{C}$ with a velocity field of motion 1 (the nip region $\mathcal{D}$ is filled with quiescent fluid). The velocity field of motion 3 ($\mathbf{u}^{(3)}$) is an admissible, non-maximizing, candidate to the porous media problem (2.16)-(2.18) defined over the region $\mathcal{C}$. In fact, $\mathbf{u}^{(3)} \in Z$ over $\mathcal{C}$ since it is a divergence-free, periodic, and continuous function which vanishes at the inclusion surfaces. So for the fluid region $\mathcal{C}$ we have

$$J^P_{\mathcal{C}}(\mathbf{u}^{(2)}) \geq J^P_{\mathcal{C}}(\mathbf{u}^{(3)}) , \tag{3.4}$$

where $\mathbf{u}^{(2)}$ is the velocity solution of motion 2 which maximizes $J^P_{\mathcal{C}}(\mathbf{v})$, $\mathbf{v} \in Z$ over $\mathcal{C}$. In addition, motions 1 and 3 disperse the same amount of energy through viscous dissipation. We can thus write

$$J^P_{\Omega}(\mathbf{u}^{(1)}) = J^P_{\mathcal{C}}(\mathbf{u}^{(3)}) , \tag{3.5}$$

where $\mathbf{u}^{(1)}$ is the velocity solution of motion 1. From (3.4), (3.5), the extremum statement of (2.21), and (3.3) we can write

$$\kappa_{LB} \leq \kappa \leq \kappa_{UB} , \tag{3.6}$$

where κ_{UB} is given by solving the permeability problem of motion 2.

Again, by increasing the size of region $\mathcal{D}$ for a given meso-scale geometry, the upper bound becomes more crude. Moreover, the addition of multiple nips still generates an upper bound. This can be proved by using a space enrichment argument: by replacing part of a sphere with fluid we increase the number of admissible test functions $\mathbf{v} \in Z$; as a result, the maximum of J^P cannot be smaller than the maximum of the original problem (motion 1).

The implementation of the bounds is straightforward: one only needs to change the geometry of the inclusions and then solve the meso-scale equations (2.23), (2.24), and (2.15).

3.2 Sedimentation Problem

As shown in figure 3-4, the geometries of the proposed micro-scale models are simple. Figure 3-4a is a sketch of the lower bound geometry which is obtained by rigidly connecting a pair of spheres by means of region $\mathcal{D}$. This region consists of a non-buoyant cylinder whose axis coincides with the line of centers and whose spherical end-caps are removed. Figure 3-4b shows the upper bound geometry, which is obtained by reducing the diameter of the spheres while holding their centers $\mathbf{y}_k$ in the same location and their buoyancy corrected weights $\mathcal{W}$ constant.

3.2.1 Lower Bound

To prove the lower bound on the settling speed of N meso-scale spheres, two of which are affected by the geometric changes described, we use the same procedure used for the porous media proofs. Figure 3-5 shows the pair of modified spheres for three different meso-scale motions. Motion 1 is the original motion of the N sedimenting spheres in the fluid region Ω. Motion 2 consists of the motion of $(N-1)$ sedimenting particles, one of which is the "dumbbell" obtained by connecting two particles of the previous geometry. The fluid occupies region $\mathcal{C} = \Omega \setminus \mathcal{D}$. Lastly, motion 3 is the "dumbbell" motion 2 extended to the larger fluid domain Ω of motion 1.

The proof follows the same logic of the porous media lower bound proof. However, due to the added particle dynamics, we present a more detailed derivation. We first consider each motion in more detail.

Motion 1 is characterized by

$$J^S_\Omega(\mathbf{u}^{(1)}) \;=\; -2\mathcal{W}\sum_{k=1}^{N}(U_2^{(1)})_k \;-\; \frac{\mu_{co}}{2}\int_\Omega \left(\frac{\partial u_i^{(1)}}{\partial y_j}+\frac{\partial u_j^{(1)}}{\partial y_i}\right)\left(\frac{\partial u_i^{(1)}}{\partial y_j}+\frac{\partial u_j^{(1)}}{\partial y_i}\right)d\mathbf{y}\,, \quad (3.7)$$

$$\int_\Omega u_1^{(1)}d\mathbf{y} \;=\; \int_\Omega u_3^{(1)}d\mathbf{y} \;=\; 0\,, \quad (3.8)$$

$$\int_{\Omega} u_2^{(1)} dy + \frac{\pi d^3}{6} \sum_{k=1}^{N} (U_2^{(1)})_k = 0 , \tag{3.9}$$

where $\mathbf{u}^{(1)}$ is the fluid velocity and $\mathbf{U}_k^{(1)}$ is the translational velocity of particle $k = 1, .., N$. In addition, the velocity field must satisfy all the requirements of (2.41) over region Ω, and be such that

$$\mathbf{u}^{(1)} = \arg\max_{\mathbf{v} \in B} J_{\Omega}^{S}(\mathbf{v}) . \tag{3.10}$$

The settling speed is given by (2.42), which can be written as

$$\mathcal{U}^{(1)} = \frac{1}{N\mathcal{W}} J_{\Omega}^{S}(\mathbf{u}^{(1)}) . \tag{3.11}$$

In motion 2 we treat the two particles that make up the "dumbbell" as a single particle with buoyancy corrected weight of $2\mathcal{W}$. Motion 2 satisfies the following strong form

$$-\frac{\partial}{\partial y_j}\left[\mu_{co}\left(\frac{\partial u_i^{(2)}}{\partial y_j} + \frac{\partial u_j^{(2)}}{\partial y_i}\right)\right] + \frac{\partial p'^{(2)}}{\partial y_i} - \tau\,\delta_{2i} = 0 \quad \text{in } \mathcal{C} \text{ for } i = 1, 2, 3 , \tag{3.12}$$

$$-\frac{\partial u_i^{(2)}}{\partial y_i} = 0 \quad \text{in } \mathcal{C} , \tag{3.13}$$

where $\tau = \frac{\sum_{k=1}^{N_D} \mathcal{W}_k}{\lambda^3} = \frac{N\mathcal{W}}{\lambda^3}$, since the buoyancy corrected weight of particle k is given by

$$\mathcal{W}_k = \begin{cases} \mathcal{W} & \text{if } k = 1, .., N_D - 1 \\ 2\mathcal{W} & \text{if } k = N_D \end{cases}$$

where $N_D = N - 1$ is the number of particles; and $k = N_D$ represents the dumbbell. The zero net flowrate requirement is expressed as,

$$-\left(\int_{\mathcal{C}} u_2^{(2)}\, dy + \sum_{k=1}^{N_D} \mathcal{V}_k (U_2^{(2)})_k\right) = 0 , \tag{3.14}$$

where $\mathbf{U}_k^{(2)}$ is the translational velocity vector of particle $k = 1, .., N_D$. The volume of particle k is given by

$$\mathcal{V}_k = \begin{cases} \frac{\pi}{6} d^3 & \text{if } k = 1, .., N_D - 1 \\ 2\frac{\pi}{6} d^3 + \mathcal{V}_{nip} & \text{if } k = N_D \end{cases}$$

where $\mathcal{V}_{nip}$ is the volume of the nip region $\mathcal{D}$. We also require for uniqueness that

$$\int_C u_1^{(2)} d\mathbf{y} \;=\; \int_C u_3^{(2)} d\mathbf{y} \;=\; 0\,, \tag{3.15}$$

and

$$\int_C p'^{(2)} d\mathbf{y} \;=\; 0\,. \tag{3.16}$$

Turning now to boundary conditions, the no-slip boundary condition reads

$$\mathbf{u}^{(2)}|_{\partial\Omega_k} \;=\; \mathbf{U}_k^{(2)} + \mathbf{W}_k^{(2)} \times (\mathbf{y} - \mathbf{y}_k)\,, \quad k = 1, \ldots, N_D\,, \tag{3.17}$$

where $\mathbf{W}_k^{(2)}$ is the rotational velocity vector of particle k; and $\mathbf{y}_k$ denotes the center (of mass) of particle k. An additional requirement on $\mathbf{u}^{(2)}$ is that it must be λ-triply periodic. Our quasi-static analysis also requires zero net force on each particle, which reads

$$\int_{\partial\Omega_k} (\mathbf{T}'^{(2)} : \mathbf{n})\, ds \;=\; (\tau\, \mathcal{V}_k - \mathcal{W}_k)\, \mathbf{e}_2\,, \quad k = 1, \ldots, N_D\,. \tag{3.18}$$

Finally, we require zero net torque on each particle, which can be written as

$$\int_{\partial\Omega_k} (\mathbf{y} - \mathbf{y}_k) \times (\mathbf{T}'^{(2)} : \mathbf{n})\, ds \;=\; 0\,, \quad k = 1, \ldots, N_D\,. \tag{3.19}$$

In the lower bound problem, the effective property of interest is the average settling speed of the particles, defined as

$$\mathcal{U}^{(2)} \equiv \frac{1}{\sum_{k=1}^{N_D} \mathcal{W}_k} I_C^S(\mathbf{u}^{(2)}) \;=\; \frac{1}{N\mathcal{W}} I_C^S(\mathbf{u}^{(2)})\,, \tag{3.20}$$

(we have used $\sum_{k=1}^{N_D} \mathcal{W}_k = N\mathcal{W}$) where for $\mathbf{v}$ satisfying $\mathbf{v}|_{\partial\Omega_k} = \mathbf{V}_k + \mathbf{Z}_k \times (\mathbf{y} - \mathbf{y}_k)$,

$$I_C^S(\mathbf{v}) = -\sum_{k=1}^{N_D} \mathcal{W}_k (V_2)_k \,. \tag{3.21}$$

The dissipation functional $J_C^S(\mathbf{v})$ is defined as in (2.38) to be

$$J_C^S(\mathbf{v}) = 2\, I_C^S(\mathbf{v}) - \mu_{co} \frac{1}{2} \int_C \left(\frac{\partial v_i}{\partial y_j} + \frac{\partial v_j}{\partial y_i} \right) \left(\frac{\partial v_i}{\partial y_j} + \frac{\partial v_j}{\partial y_i} \right) d\mathbf{y} \,. \tag{3.22}$$

By multiplying equation (3.12) by $\mathbf{u}^{(2)}$, integrating by parts over $\mathcal{C}$, and using (3.13)–(3.19), we derive

$$I_C^S(\mathbf{u}^{(2)}) = J_C^S(\mathbf{u}^{(2)}) = \mu_{co} \frac{1}{2} \int_C \left(\frac{\partial u_i^{(2)}}{\partial y_j} + \frac{\partial u_j^{(2)}}{\partial y_i} \right) \left(\frac{\partial u_i^{(2)}}{\partial y_j} + \frac{\partial u_j^{(2)}}{\partial y_i} \right) d\mathbf{y} \,. \tag{3.23}$$

From (3.20) and (3.23) it is clear that the settling velocity $\mathcal{U}^{(2)}$ is always positive.

As for the original sedimentation problem, we can prove that (see Section 2.3)

$$\mathbf{u}^{(2)} = \arg\max_{\mathbf{v} \in B} J_C^S(\mathbf{v}) \,, \tag{3.24}$$

where

$$B = \left\{ \mathbf{v} \in Y \mid \operatorname{div} \mathbf{v} = 0 \,,\ \int_C v_2 \, d\mathbf{y} + \sum_{k=1}^{N_D} \mathcal{V}_k (V_2)_k = 0 \right\} \,, \tag{3.25}$$

and

$$Y = \Big\{ (v_1, v_2, v_3) \in (H^1_{\#}(C))^3 \ \mid \ \int_C v_1 \, d\mathbf{y} = 0 \,, \int_C v_3 \, d\mathbf{y} = 0 \,,$$
$$\text{and } \forall\, k \in \{1, \ldots, N_D\}, \mathbf{v}|_{\partial\Omega_k} = \mathbf{V}_k + \mathbf{Z}_k \times (\mathbf{y} - \mathbf{y}_k), \mathbf{V}_k \in \mathcal{R}^3 \,, \mathbf{Z}_k \in \mathcal{R}^3 \Big\} \,.$$

From (3.20) and (3.23) we can derive the following expression for the settling velocity,

$$\mathcal{U}^{(2)} = \frac{1}{N\mathcal{W}} J_C^S(\mathbf{u}^{(2)}) \,, \tag{3.26}$$

which in view of (3.24), becomes

$$\mathcal{U}^{(2)} = \frac{1}{N\mathcal{W}} \max_{\mathbf{v}\in B} J_{\mathcal{C}}^{S}(\mathbf{v}) \,. \tag{3.27}$$

In order to arrive at (3.24), we multiply (3.12) by the test function $\mathbf{v} \in B$, and integrate over $\mathcal{C}$. By integrating by parts, using (3.18), (3.19) and the attributes of the space B over $\mathcal{C}$, we obtain that the first variation of $J_{\mathcal{C}}^{S}(\mathbf{u}^{(2)})$ is equal to zero. Since the second variation is always negative, we are extremizing $J_{\mathcal{C}}^{S}(\mathbf{v})$ as described in (3.24).

Finally, in motion 3 the fluid region is enlarged to contain the nip region $\mathcal{D}$ with a velocity field that consists of motion 2 extended to region $\mathcal{D}$ as follows

$$(\mathbf{u}^{(3)})' = \begin{cases} \mathbf{u}^{(2)} & \text{in } \Omega \setminus \mathcal{D} \\ \mathbf{U}_{N_D}^{(2)} + \mathbf{W}_{N_D}^{(2)} \times (\mathbf{y} - \mathbf{y}_{N_D}) & \text{in } \mathcal{D} \ . \end{cases} \tag{3.28}$$

We introduce motion 3 to prove that motion 2 provides a lower bound for the settling speed of N spheres (motion 1). First, we show that the velocity field of motion 3 is an admissible variation of the original meso-scale problem of motion 1. In other words, we want to prove that $\mathbf{u}^{(3)} \in B$ over the domain Ω. In order to satisfy (3.8), we need to shift the velocity field $(\mathbf{u}^{(3)})'$ in the following manner

$$\mathbf{u}^{(3)} = \begin{cases} \mathbf{u}^{(2)} - A\mathbf{e}_1 - C\mathbf{e}_3 & \text{in } \Omega \setminus \mathcal{D} \\ \mathbf{U}_{N_D}^{(2)} + \mathbf{W}_{N_D}^{(2)} \times (\mathbf{y} - \mathbf{y}_{N_D}) - A\mathbf{e}_1 - C\mathbf{e}_3 & \text{in } \mathcal{D} \end{cases}$$

where $A = (U_1^{(2)})_{N_D} \frac{\mathcal{V}_{nip}}{\mathcal{V}_\Omega}$; $C = (U_3^{(2)})_{N_D} \frac{\mathcal{V}_{nip}}{\mathcal{V}_\Omega}$; and $\mathcal{V}_\Omega$ is the volume of region Ω. Since we have not added a shift in the $\mathbf{e}_2$ direction, motion 3 does not violate the zero net volume flowrate condition (3.14) satisfied by motion 2. In fact, condition (3.14) requires that the integral of the velocity in the $\mathbf{e}_2$ direction at every point in the meso-cell (fluid *and* particles) vanish. Since the velocity components in the $\mathbf{e}_2$ direction of motions 2 and 3 are identical at each point within the meso-scale cube of volume λ^3, it follows that motion 3 satisfies the zero net flowrate condition. Moreover, the velocity field is still continuous and λ-triple periodic (i.e. it is in $(H^1_{\#}(\Omega))^3$). The fluid

motion is consistent with solid body motion of the particles and the no-slip boundary condition. In addition, $\mathbf{u}^{(3)}$ is still divergence-free since the fluid in region $\mathcal{D}$ is in solid body motion. Having showed that $\mathbf{u}^{(3)} \in B$ over region Ω, it follows from (3.10) that

$$J_{\Omega}^{S}(\mathbf{u}^{(1)}) \geq J_{\Omega}^{S}(\mathbf{u}^{(3)}) . \tag{3.29}$$

Second, we show that the velocity field of motions 2 and 3 create the same amount of viscous dissipation, since solid body rotation and translation of the fluid in region $\mathcal{D}$ of motion 3 does not dissipate energy. Physically, it is intuitive that translation does not dissipate energy. Moreover, even solid body rotation does not dissipate energy. In fact, imagine a bucket of water that is rotating on a frictionless turntable. In steady state, no energy input is needed to sustain the motion. In addition, since $I_{\mathcal{C}}^{S}(\mathbf{u}^{(2)}) = I_{\Omega}^{S}(\mathbf{u}^{(3)})$, it must be that

$$J_{\mathcal{C}}^{S}(\mathbf{u}^{(2)}) = J_{\Omega}^{S}(\mathbf{u}^{(3)}) . \tag{3.30}$$

From (3.11), (3.26), (3.29) and (3.30), we can assert that $\mathcal{U}^{(2)} \leq \mathcal{U}^{(1)}$, which we rewrite as

$$\mathcal{U}_{LB} \leq \mathcal{U} , \tag{3.31}$$

where $\mathcal{U}_{LB} = \mathcal{U}^{(2)}$ and $\mathcal{U} = \mathcal{U}^{(1)}$. Note that we are able to make this comparison because the two settling speeds have the same proportionality to their corresponding dissipation integrals due to our requirement that the weight of the dumbbell is the same as the weight of two spheres.

Unlike for the porous media problem, the modified geometry requires certain changes in the dimensional formulation of the meso-scale equations (2.44)-(2.46) that lead to changes in the dimensionless formulation of the problem (2.48)-(2.50). Let us examine the case of N spheres two of which are rigidly connected. Equation (2.44) changes to

$$\mu_{co}\int_C \frac{\partial v_i}{\partial y_j}\left(\frac{\partial u_i^{(2)}}{\partial y_j}+\frac{\partial u_j^{(2)}}{\partial y_i}\right)d\mathbf{y} \;-\; \int_C p'^{(2)}\frac{\partial v_i}{\partial y_i}\,d\mathbf{y} \;-\; \frac{N\mathcal{W}}{\mathcal{V}_{tot}}\left[\int_C v_2\,d\mathbf{y}+\sum_{k=1}^{N_D}\mathcal{V}_k(V_2)_k\right]$$
$$= \;-\sum_{k=1}^{N_D}\mathcal{W}_k(V_2)_k \quad \forall\,\mathbf{v}\in Y\,, \tag{3.32}$$

where we have replaced τ with expression (2.47) since the total weight of the particles does not change. By non-dimensionalizing (3.32) we obtain

$$\int_C \frac{\partial v_i}{\partial y_j}\left(\frac{\partial u_i^{(2)}}{\partial y_j}+\frac{\partial u_j^{(2)}}{\partial y_i}\right)d\mathbf{y} \;-\; \int_C p'^{(2)}\frac{\partial v_i}{\partial y_i}\,d\mathbf{y} \;-\; c\left[\int_C v_2\,d\mathbf{y}+\frac{\pi}{6}\sum_{k=1}^{N}(V_2)_k\right]$$
$$-\frac{\pi}{6}N\frac{\mathcal{V}_{nip}}{\mathcal{V}_{tot}}(V_2)_{N_D} \;=\; -\frac{\pi}{6}\sum_{k=1}^{N}(V_2)_k \quad \forall\,\mathbf{v}\in Y\,, \tag{3.33}$$

where $c=\frac{N\pi d^3}{6\lambda^3}$ is the sphere volume fraction previous to the addition of the nip; and $(V_2)_N\equiv(V_2)_{N_D}$ since the two spheres of the dumbbell, treated separately in the summations of (3.33), must conform to the original dumbbell rigid body motion. In the case of $N=2$, (3.33) reduces to

$$\int_C \frac{\partial v_i}{\partial y_j}\left(\frac{\partial u_i^{(2)}}{\partial y_j}+\frac{\partial u_j^{(2)}}{\partial y_i}\right)d\mathbf{y} \;-\; \int_C p'^{(2)}\frac{\partial v_i}{\partial y_i}\,d\mathbf{y} \;-\; c\int_C v_2\,d\mathbf{y} \;-\; 2c'\frac{\pi}{6}(V_2)_{N_D}$$
$$= \;-2\frac{\pi}{6}(V_2)_{N_D} \quad \forall\,\mathbf{v}\in Y\,, \tag{3.34}$$

where $c'=\frac{2\pi d^3/6+\mathcal{V}_{nip}}{\lambda^3}$ is the volume fraction occupied by the entire dumbbell.

Equation (2.45) still holds in region $\mathcal{C}$, as does (2.49). However, (2.46) does change and so does the dimensionless (2.50). For N particles, a pair of which forms a dumbbell, we have

$$-\eta\left[\int_C u_2^{(2)}\,d\mathbf{y}+\sum_{k=1}^{N_D}\mathcal{V}_k(U_2^{(2)})_k\right]=0 \quad \forall\,\eta\in\mathcal{R}\,. \tag{3.35}$$

By non-dimensionalizing this equation we obtain

$$-\eta\left[\int_C u_2^{(2)}\,d\mathbf{y}+\frac{\pi}{6}\sum_{k=1}^{N}(U_2^{(2)})_k+\frac{\mathcal{V}_{nip}}{d^3}(U_2^{(2)})_{N_D}\right]=0\quad\forall\eta\in\mathcal{R}\,,\tag{3.36}$$

where $(U_2^{(2)})_N \equiv (U_2^{(2)})_{N_D}$. For the case of two spherical inclusions ($N = 2$ and $N_D = 1$) (3.36) reduces to

$$-\eta\left[\int_C u_2^{(2)}\,d\mathbf{y}+\left(2\frac{\pi}{6}+\frac{\mathcal{V}_{nip}}{d^3}\right)(U_2^{(2)})_{N_D}\right]=0\quad\forall\eta\in\mathcal{R}\,.\tag{3.37}$$

Equations (2.49),(3.34) and (3.37) describe the two particle ($N = 2$) problem that is solved and described in Chapter 5 to show the lower bound results.

It should be mentioned, that introducing multiple nips still produces a lower bound on the settling speed. In fact, whenever two spheres are connected, we effectively remove six degrees-of-freedom from the original suspension (three translational and three rotational). Having restricted the space of admissible functions, the maximum of the new problem cannot be greater than the maximum of the original problem, and since the total buoyancy corrected weight of the particles is constant, we indeed have a lower bound on the settling speed.

3.2.2 Upper Bound

The upper bound proof follows closely the lower bound one. Again, we are concerned with the settling speed of N meso-scale spheres two of which are affected by the geometric changes described. Figure 3-6 shows three different motions. Motion 1 is the original motion of the N sedimenting spheres in fluid region Ω. Motion 2 consists of the motion of the same N sedimenting particles, two of which are shrunk to a smaller diameter $d'(< d)$ but preserve the same buoyancy corrected weight and center of mass. The fluid occupies region $\mathcal{C} = \Omega \cup \mathcal{D}$; where $\mathcal{D} = \bigcup_{k=N-1}^{N} \Omega'_k$ is the region of fluid obtained by shrinking the spheres $k = N-1$ and $k = N$ (see figure 3-4). Region Ω'_k is the spherical shell of inner diameter d' and outer diameter d obtained by shrinking sphere k. Lastly, motion 3 consists of motion 1 extended to the larger

fluid domain $\mathcal{C}$ of motion 2. We now characterize the three motions in more detail.

Motion 1 is described in Section 3.2.1 by equations (3.7)-(3.11). In motion 2 we have N spheres, two of which are shrunk ($k = N-1$ and $k = N$). Motion 2 satisfies the following strong form

$$-\frac{\partial}{\partial y_j}\left[\mu_{co}\left(\frac{\partial u_i^{(2)}}{\partial y_j}+\frac{\partial u_j^{(2)}}{\partial y_i}\right)\right]+\frac{\partial p'^{(2)}}{\partial y_i}-\tau\,\delta_{2i}=0 \quad \text{in } \mathcal{C} \text{ for } i=1,2,3\,, \tag{3.38}$$

$$-\frac{\partial u_i^{(2)}}{\partial y_i}=0 \quad \text{in } \mathcal{C}\,, \tag{3.39}$$

where $\tau = \frac{N\mathcal{W}}{\lambda^3}$. The zero net flowrate requirement is expressed as,

$$-\left(\int_{\mathcal{C}} u_2^{(2)}\,d\mathbf{y}+\sum_{k=1}^{N}\mathcal{V}_k(U_2^{(2)})_k\right)=0\,, \tag{3.40}$$

where $\mathbf{U}_k^{(2)}$ is the translational velocity vector of particle $k = 1,..,N$. The volume of particle k is given by

$$\mathcal{V}_k=\begin{cases}\frac{\pi}{6}d^3 & \text{if } k=1,..,(N-2)\\ \frac{\pi}{6}d'^3 & \text{if } k=(N-1),N\end{cases}$$

To ensure uniqueness of the solution we require

$$\int_{\mathcal{C}} u_1^{(2)}d\mathbf{y}\;=\;\int_{\mathcal{C}} u_3^{(2)}d\mathbf{y}\;=\;0\,, \tag{3.41}$$

and

$$\int_{\mathcal{C}} p'^{(2)}d\mathbf{y}\;=\;0\,. \tag{3.42}$$

Focusing now on boundary conditions, the no-slip boundary condition reads

$$\mathbf{u}^{(2)}|_{\partial\Omega_k}\;=\;\mathbf{U}_k^{(2)}+\mathbf{W}_k^{(2)}\times(\mathbf{y}-\mathbf{y}_k)\,,\quad k=1,\ldots,N\,, \tag{3.43}$$

where $\mathbf{W}_k^{(2)}$ is the rotational velocity vector of particle k; and $\mathbf{y}_k$ denotes the center (of mass) of particle k. In addition, we require that $\mathbf{u}^{(2)}$ is λ-triply periodic. Our

quasi-static analysis also requires zero net force on each particle, which reads

$$\int_{\partial\Omega_k} (\mathbf{T}'^{(2)} : \mathbf{n})\, ds \;=\; (\tau\, \mathcal{V}_k - \mathcal{W})\, \mathbf{e}_2\,, \quad k = 1, \ldots, N\,, \tag{3.44}$$

and zero net torque on each particle, which can be written as

$$\int_{\partial\Omega_k} (\mathbf{y} - \mathbf{y}_k) \times (\mathbf{T}'^{(2)} : \mathbf{n})\, ds \;=\; 0\,, \quad k = 1, \ldots, N\,. \tag{3.45}$$

In the upper bound problem, the effective property of interest is the average settling speed of the particles, defined as

$$\mathcal{U}^{(2)} \equiv \frac{1}{N\mathcal{W}} I_C^S(\mathbf{u}^{(2)})\,, \tag{3.46}$$

where, for $\mathbf{v}$ satisfying $\mathbf{v}|_{\partial\Omega_k} = \mathbf{V}_k + \mathbf{Z}_k \times (\mathbf{y} - \mathbf{y}_k)$,

$$I_C^S(\mathbf{v}) \;=\; -\mathcal{W} \sum_{k=1}^{N} (V_2)_k\,. \tag{3.47}$$

The dissipation functional $J_C^S(\mathbf{v})$ is defined as in (2.38) to be

$$J_C^S(\mathbf{v}) \;=\; 2\, I_C^S(\mathbf{v}) \;-\; \mu_{co}\, \frac{1}{2} \int_C \left(\frac{\partial v_i}{\partial y_j} + \frac{\partial v_j}{\partial y_i} \right) \left(\frac{\partial v_i}{\partial y_j} + \frac{\partial v_j}{\partial y_i} \right) d\mathbf{y}\,. \tag{3.48}$$

By multiplying equation (3.38) by $\mathbf{u}^{(2)}$, integrating by parts over $\mathcal{C}$, and using (3.39)–(3.45), we derive

$$I_C^S(\mathbf{u}^{(2)}) \;=\; J_C^S(\mathbf{u}^{(2)}) \;=\; \mu_{co}\, \frac{1}{2} \int_C \left(\frac{\partial u_i^{(2)}}{\partial y_j} + \frac{\partial u_j^{(2)}}{\partial y_i} \right) \left(\frac{\partial u_i^{(2)}}{\partial y_j} + \frac{\partial u_j^{(2)}}{\partial y_i} \right) d\mathbf{y}\,. \tag{3.49}$$

Again, we can prove that (see Section 2.3)

$$\mathbf{u}^{(2)} \;=\; \arg\max_{\mathbf{v} \in B} J_C^S(\mathbf{v})\,, \tag{3.50}$$

where

$$B \;=\; \left\{ \mathbf{v} \in Y \mid \operatorname{div} \mathbf{v} = 0\,,\; \int_C v_2\, d\mathbf{y} \;+\; \sum_{k=1}^{N} \mathcal{V}_k (V_2)_k = 0 \right\}\,, \tag{3.51}$$

and

$$Y = \left\{(v_1, v_2, v_3) \in (H^1_{\#}(\mathcal{C}))^3 \;\middle|\; \int_{\mathcal{C}} v_1 \, d\mathbf{y} = 0\,, \int_{\mathcal{C}} v_3 \, d\mathbf{y} = 0\,,\right.$$
$$\left. \text{and } \forall k \in \{1, \ldots, N\}, \mathbf{v}|_{\partial\Omega_k} = \mathbf{V}_k + \mathbf{Z}_k \times (\mathbf{y} - \mathbf{y}_k), \mathbf{V}_k \in \mathcal{R}^3\,, \mathbf{Z}_k \in \mathcal{R}^3\right\}.$$

From (3.46) and (3.49) we can derive the following expression for the settling velocity,

$$\mathcal{U}^{(2)} = \frac{1}{N\mathcal{W}} J^S_{\mathcal{C}}(\mathbf{u}^{(2)})\,, \tag{3.52}$$

which in view of (3.50), becomes

$$\mathcal{U}^{(2)} = \frac{1}{N\mathcal{W}} \max_{\mathbf{v} \in B} J^S_{\mathcal{C}}(\mathbf{v})\,. \tag{3.53}$$

Finally, motion 3 consists of motion 1 with region $\mathcal{D}$ replaced by fluid. This motion is first defined as

$$(\mathbf{u}^{(3)})' = \begin{cases} \mathbf{u}^{(1)} & \text{in } \mathcal{C} \setminus \mathcal{D} \\ \mathbf{U}^{(1)}_k + \mathbf{W}^{(1)}_k \times (\mathbf{y} - \mathbf{y}_k) & \text{in } \Omega'_k,\ k = N-1, N\ . \end{cases} \tag{3.54}$$

Then, in order to satisfy (3.41) we need to shift this velocity field in a similar fashion to the lower bound problem:

$$\mathbf{u}^{(3)} = \begin{cases} \mathbf{u}^{(1)} - D\mathbf{e}_1 - F\mathbf{e}_3 & \text{in } \mathcal{C} \setminus \mathcal{D} \\ \mathbf{U}^{(1)}_k + \mathbf{W}^{(1)}_k \times (\mathbf{y} - \mathbf{y}_k) - D\mathbf{e}_1 - F\mathbf{e}_3 & \text{in } \Omega'_k,\ k = N-1, N \end{cases}$$

where $D = \sum_{k=N-1}^{N} (U^{(1)}_1)_k \frac{\mathcal{V}_{\Omega'}}{\mathcal{V}_{\mathcal{C}}}$ and $F = \sum_{k=N-1}^{N} (U^{(1)}_3)_k \frac{\mathcal{V}_{\Omega'}}{\mathcal{V}_{\mathcal{C}}}$ are the shifts. We have used $\mathcal{V}_{\Omega'}$ to denote the volume of the spherical shell of inner diameter d' and outer diameter d, and $\mathcal{V}_{\mathcal{C}}$ to denote the volume of region $\mathcal{C}$. Notice that the velocity field $\mathbf{u}^{(3)}$ of motion 3 consists of the velocity field $\mathbf{u}^{(1)}$ over Ω and the solid body rotation and translation of the two unshrunk spheres extended to the fluid region $\mathcal{D}$ (plus the discussed shifts). First, we show that the velocity field of motion 3 is an admissible candidate to the upper bound problem of motion 2. In fact, the concocted field $\mathbf{u}^{(3)}$ satisfies (3.41) by construction, and is continuous, λ-triply periodic, and divergence-

free. In addition, it is consistent with no-slip at the fluid-particle interface and it satisfies zero net flowrate in the $\mathbf{e}_2$ direction since motion 1 satisfies this requirement. In fact,

$$\begin{aligned}
\int_{\mathcal{C}} u_2^{(3)} d\mathbf{y} + \sum_{k=1}^{N} \mathcal{V}_k (U_2^{(3)})_k &= \\
\int_{\Omega} u_2^{(1)} d\mathbf{y} + \sum_{k=N-1}^{N} \int_{\Omega_k'} \left\{ (U_2^{(1)})_k \right. &+ \left. [\mathbf{W}_k^{(1)} \times (\mathbf{y} - \mathbf{y}_k)]_2 \right\} d\mathbf{y} + \\
\frac{\pi d^3}{6} \sum_{k=1}^{N-2} (U_2^{(1)})_k &+ \frac{\pi d'^3}{6} \sum_{k=N-1}^{N} (U_2^{(1)})_k = \\
\int_{\Omega} u_2^{(1)} d\mathbf{y} + \frac{\pi d^3}{6} \sum_{k=1}^{N} (U_2^{(1)})_k &= 0 \,,
\end{aligned} \tag{3.55}$$

where we used (3.54) and the fact that $\int_{\Omega_k'} [\mathbf{W}_k^{(1)} \times (\mathbf{y} - \mathbf{y}_k)]_2 d\mathbf{y} = 0$. In conclusion, the proposed velocity field $\mathbf{u}^{(3)}$ is an admissible candidate for the sedimentation problem defined over the geometry $\mathcal{C}$. This translates as

$$J_{\mathcal{C}}^S(\mathbf{u}^{(2)}) \geq J_{\mathcal{C}}^S(\mathbf{u}^{(3)}) \,. \tag{3.56}$$

It can also be shown that the velocity field of motion 3 creates the same amount of viscous dissipation as the field of motion 1, since solid body rotation and translation of the fluid in region $\mathcal{D}$ in motion 3 do not dissipate energy. From this, and the fact that $I_{\Omega}^S(\mathbf{u}^{(1)}) = I_{\mathcal{C}}^S(\mathbf{u}^{(3)})$, it follows that

$$J_{\Omega}^S(\mathbf{u}^{(1)}) = J_{\mathcal{C}}^S(\mathbf{u}^{(3)}) \,. \tag{3.57}$$

From (3.11), (3.52), (3.56), (3.57), and the fact that all particles weigh the same, we realize that $\mathcal{U}^{(1)} \leq \mathcal{U}^{(2)}$, which is written as

$$\mathcal{U} \leq \mathcal{U}_{UB} \,, \tag{3.58}$$

where $\mathcal{U}_{UB} = \mathcal{U}^{(2)}$ and $\mathcal{U} = \mathcal{U}^{(1)}$. The reader should be aware of the fact that this is a bound on the dimensional settling speed. Non-dimensional speeds are discussed

later in the section.

The modified geometry requires certain changes in the dimensional formulation of the meso-scale equations (2.44)-(2.46), that lead to changes in the dimensionless formulation of the problem (2.48)-(2.50). Again, let us examine the case of N spheres two of which are shrunk while keeping their buoyancy corrected weight constant.

Equation (2.44) changes to

$$\mu_{co}\int_C \frac{\partial v_i}{\partial y_j}\left(\frac{\partial u_i^{(2)}}{\partial y_j}+\frac{\partial u_j^{(2)}}{\partial y_i}\right)d\mathbf{y} \;-\; \int_C p'^{(2)}\frac{\partial v_i}{\partial y_i}\,d\mathbf{y} - \frac{N\mathcal{W}}{\mathcal{V}_{tot}}\left[\int_C v_2\,d\mathbf{y}+\sum_{k=1}^{N}\mathcal{V}_k(V_2)_k\right]$$
$$= \;-\mathcal{W}\sum_{k=1}^{N}(V_2)_k \quad \forall\,\mathbf{v}\in Y\,, \tag{3.59}$$

where we have replaced τ with expression (2.47) since the total weight of the particles does not change. When non-dimensionalizing (3.59) we use d' as the length scale of the problem. This leads to

$$\int_C \frac{\partial v_i}{\partial y_j}\left(\frac{\partial u_i^{(2)}}{\partial y_j}+\frac{\partial u_j^{(2)}}{\partial y_i}\right)d\mathbf{y} \;-\; \int_C p'^{(2)}\frac{\partial v_i}{\partial y_i}\,d\mathbf{y} - c'\left[\int_C v_2\,d\mathbf{y}+\frac{\pi}{6}\sum_{k=(N-1)}^{N}(V_2)_k\right]$$
$$-c\frac{\pi}{6}\sum_{k=1}^{N-2}(V_2)_k \;=\; -\frac{\pi}{6}\sum_{k=1}^{N}(V_2)_k \quad \forall\,\mathbf{v}\in Y\,, \tag{3.60}$$

where $c=\frac{N\pi d^3}{6\lambda^3}$; $c'=\frac{N\pi d'^3}{6\lambda^3}$; and the summation $\sum_{k=1}^{N-2}$ vanishes for $N=2$. In the case of $N=2$, (3.60) reduces to (2.48) by replacing c with c'.

Equation (2.45) still holds in region $\mathcal{C}$, as does (2.49). However, (2.46) does change and so does the dimensionless (2.50). For N particles, a pair of which is shrunk, we have

$$-\eta\left[\int_C u_2^{(2)}\,d\mathbf{y}+\sum_{k=1}^{N}\mathcal{V}_k(U_2^{(2)})_k\right]=0 \quad \forall\,\eta\in\mathcal{R}\,. \tag{3.61}$$

By non-dimensionalizing this equation we obtain (using d' as the length scale)

$$-\eta\left[\int_C u_2^{(2)}\,dy+\frac{\pi}{6}\sum_{k=(N-1)}^{N}(U_2^{(2)})_k+\frac{\pi}{6}(\frac{d}{d'})^3\sum_{k=1}^{N-2}(U_2^{(2)})_k\right]=0\quad\forall\eta\in\mathcal{R}\,,\qquad(3.62)$$

which for the case of two spherical inclusions $N=2$ reduces to (2.50). Equations (2.48)-(2.50) describe the two particle problem ($N=2$) that is solved and described in Chapter 5 to show the upper bound results, taking care of using c' as the particle concentration.

Notice that we use c' instead of c for particle concentration. Since we use a different length scale to non-dimensionalize the upper bound problem, we have to take care when comparing the settling speeds. In fact, our upper bound proof applies to the *dimensional* settling speeds $\mathcal{U}$ and $\mathcal{U}_{UB}$. Since our numerical procedure relies on the dimensionless formulation of the sedimentation problem we need to state what happens to the dimensionless settling speeds $\mathcal{U}^*$ and $\mathcal{U}^*_{UB}$. In motion 1, the velocities are non-dimensionalized by $(\frac{\Delta\rho_{co}gd^2}{\mu_{co}})=(\frac{6\mathcal{W}}{\pi\mu_{co}d})$; whereas in the upper bound problem we use $(\frac{6\mathcal{W}}{\pi\mu_{co}d'})$. It follows from (3.58) that

$$\mathcal{U}^*\;\leq\;\left(\frac{d}{d'}\right)\mathcal{U}^*_{UB}\,,\qquad(3.63)$$

for N particles in a cell.

Since in this study we only implement the micro-scale treatment for the case $N=2$, we choose to non-dimensionalize the upper bound equations (3.59) and (3.61) by using d' as the length scale. In this fashion, the variational weak form reduces to the original meso-scale equations (2.48)-(2.50). In general, when $N>2$, we might non-dimensionalize (3.59) and (3.61) with d so that (3.63) reduces to $\mathcal{U}^*\leq\mathcal{U}^*_{UB}$.

It should be mentioned that shrinking more than two spheres still produces an upper bound on the settling speed. In fact, whenever the diameter of a sphere is reduced, we effectively enrich the space B so that the maximum of J^S has to be greater than, or equal to, the maximum of the original problem. Since the buoyancy corrected weight is constant, the settling speed for the modified problem has to be greater or equal than that of the original problem.

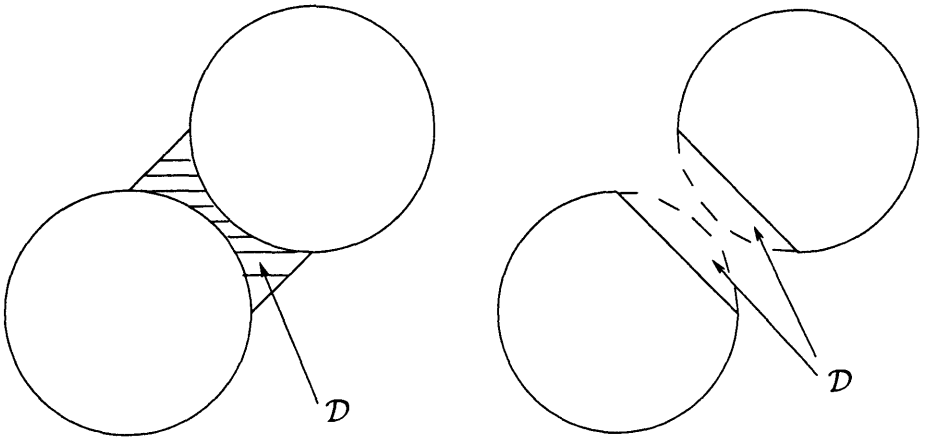

Figure 3-1: Porous media nip-region modification: a) nip-region blockage (lower bound); b) nip-region enlargement (upper bound).

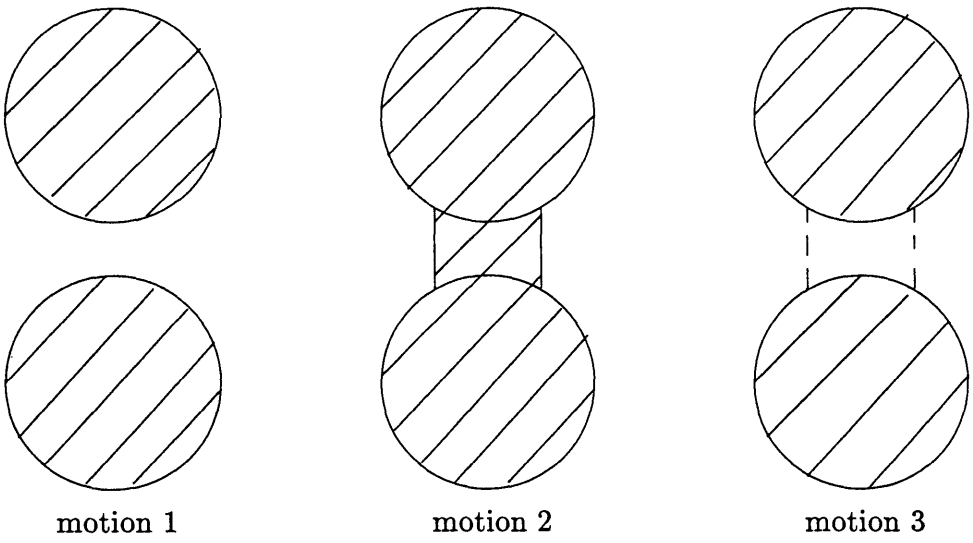

Figure 3-2: Porous media lower bound proof.

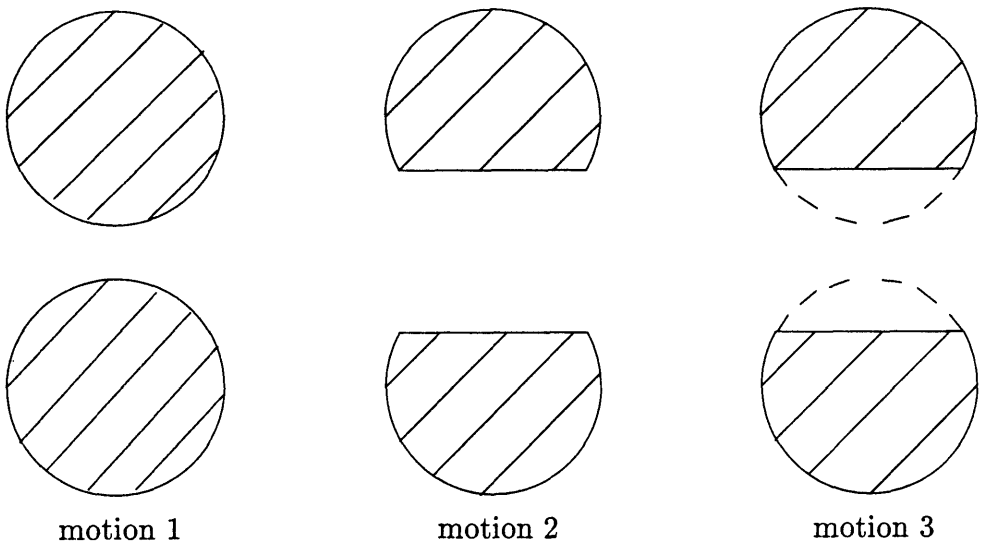

Figure 3-3: Porous media upper bound proof.

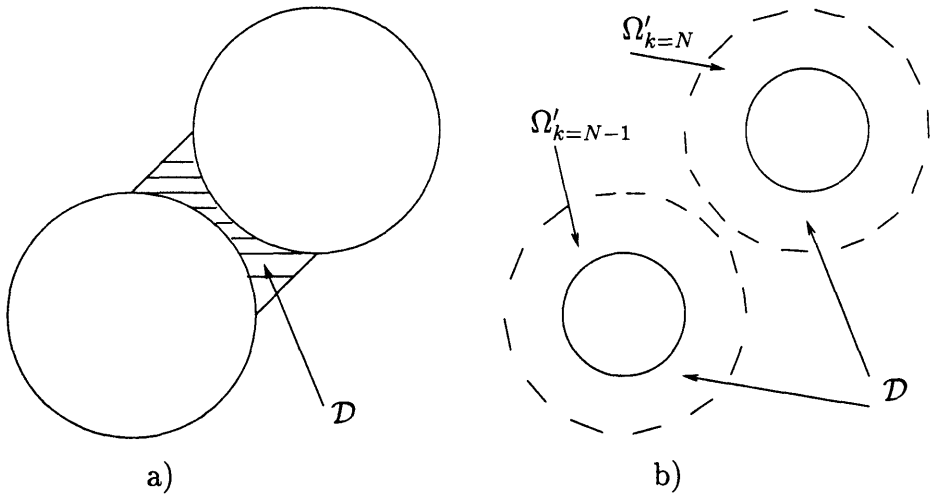

Figure 3-4: Sedimentation nip-region modification: a) connecting two spheres to make a dumbbell (lower bound); b) shrinking two spheres (upper bound).

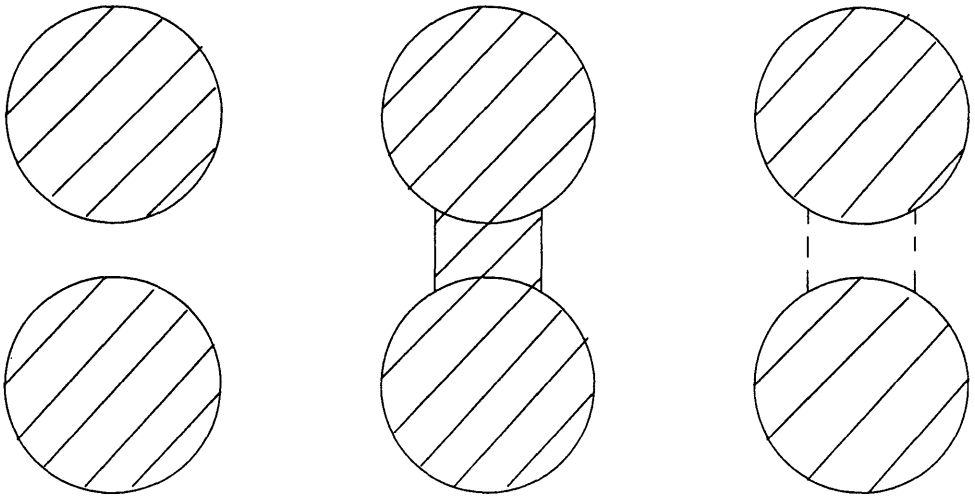

Figure 3-5: Sedimentation lower bound proof.

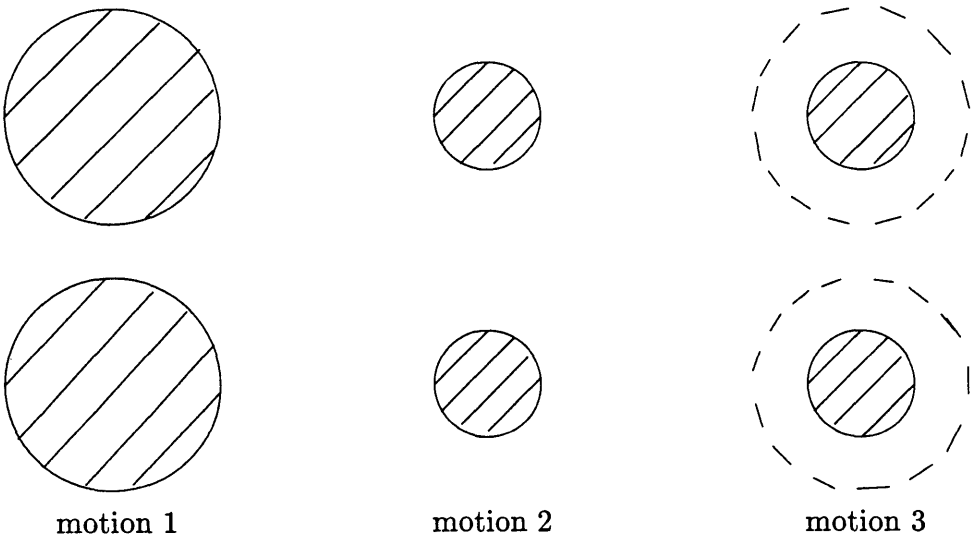

Figure 3-6: Sedimentation upper bound proof.

Chapter 4

Numerical Methods

In this chapter we implement the finite element method to solve the variational weak forms of the porous media and sedimentation problems. In Section 4.1 we review some fundamental notions with the aid of a model problem: Poisson's equation. The section discusses the discrete finite element matrix equations, the solution algorithm, and the mesh generation procedure. In Section 4.2 we build on Section 4.1 to formulate the porous media discrete equations and solution scheme. Finally, in Section 4.3 we extend the discussion to the sedimentation problem.

4.1 Three-Dimensional Finite-Element Methods: Discretization and Solution of Poisson's Equation

4.1.1 Discretization at a Global Level

We discuss a finite element discretization and solution of the following Poisson problem defined over the meso-scale region Ω_{me}

$$-\nabla^2 u = f \quad \text{in } \Omega_{me}\,, \tag{4.1}$$

where $u(\mathbf{y})$ is the unknown scalar field and $f(\mathbf{y})$ is the forcing term. The boundary conditions are Dirichlet on the sphere boundaries $\partial\Omega_{me}$ and periodic on the cube boundaries $\partial\Omega_{\#}$ (see figure 2-4).

$$u = 0 \qquad \text{on } \partial\Omega_{me}\,, \tag{4.2}$$

$$u(\mathbf{y}) = u(\mathbf{y} + \lambda(m_1\mathbf{e}_1 + m_2\mathbf{e}_2 + m_3\mathbf{e}_3)) \;\text{ on } \partial\Omega_{\#}\,, \tag{4.3}$$

where $(\mathbf{e}_1, \mathbf{e}_2, \mathbf{e}_3)$ represent the unit vectors of the coordinate system (y_1, y_2, y_3); and m_1, m_2, m_3 are integers. The variational weak form associated with the problem is given by

$$a(v,u) = (v,f) \qquad \forall v \in X\,, \tag{4.4}$$

where

$$a(v,u) = \int_{\Omega_{me}} \frac{\partial v}{\partial y_k}\frac{\partial u}{\partial y_k} d\mathbf{y}\,, \tag{4.5}$$

and

$$(v,f) = \int_{\Omega_{me}} v f d\mathbf{y}\,. \tag{4.6}$$

The space $X = \{v \in H^1_{0\#}(\Omega_{me})\}$ is the space of all λ-triply periodic square-integrable functions that vanish at the surface of a sphere and whose first derivatives are square-integrable.

We subdivide the fluid region Ω_{me} into $\mathcal{K}$ conforming tetrahedra Ω^{k_e} such that

$$\Omega_{me} = \bigcup_{k_e=1}^{\mathcal{K}} \Omega^{k_e} \qquad k_e = 1, .., \mathcal{K}\,. \tag{4.7}$$

We introduce the discrete approximation of X: $X_h = \{v|_{\Omega^{k_e}} \in \mathcal{P}_{\mathcal{N}_0}(\Omega^{k_e})\} \cap H^1_{\#}(\Omega_{me})$ where $\mathcal{P}_{\mathcal{N}_0}$ are polynomials of total degree $\mathcal{N}_0 = 1, 2$ defined on the tetrahedra Ω^{k_e}. The intersection with $H^1_{\#}(\Omega_{me})$ guarantees that v is a continuous function across

elements. Although first order elements ($\mathcal{N}_o = 1$) suffice for Poisson's problem, we introduce second order elements ($\mathcal{N}_o = 2$) because they are needed in Sections 4.2 and 4.3. Note that the function $v \in X_h$ does not have to vanish at the surface of a sphere: we take care of the Dirichlet boundary condition in our solution scheme of Section 4.1.3.

We now introduce the global basis functions $\phi_i \in X_h$

$$\phi_i(\mathbf{y}_j) \;=\; \delta_{ij}\,, \quad 1 \leq i,j \leq N_{gn}\,, \tag{4.8}$$

where N_{gn} is the total number of global nodes; and $\mathbf{y}_j$ is the coordinate of the j^{th} global node. We can use the basis ϕ_i to represent a function v over Ω_{me}

$$v(\mathbf{y}) \;=\; \sum_{i=1}^{N_{gn}} v_i \phi_i(\mathbf{y})\,, \tag{4.9}$$

where $v_i = v(\mathbf{y}_i)$. Note that $span\{\phi_i\} = X_h$.

If we use (4.9) to expand all the functions of the variational form (4.4) (except for $f(\mathbf{y})$ which can be discontinuous), we obtain the linear matrix equation

$$\underline{\mathbf{A}}\,\underline{u_h} \;=\; \underline{f}\,, \tag{4.10}$$

where the global matrix $\underline{\mathbf{A}} = A_{ij} = a(\phi_i, \phi_j)$ is the discrete Laplacian operator; $\underline{u_h}$ is the global vector of the unknown nodal values of the discrete field $u_h(\mathbf{y}) \in X_h$; and $\underline{f} = \int_{\Omega_{me}} \phi_i f d\mathbf{y}$ is the forcing vector. If $f(\mathbf{y})$ is a continuous function, we can approximate $\underline{f}$ as $\underline{\tilde{f}}$

$$\underline{f} \;\approx\; \underline{\tilde{f}} \;=\; \underline{\mathbf{M}}\underline{\hat{f}}\,, \tag{4.11}$$

where $\underline{\mathbf{M}} = M_{ij} = (\phi_i, \phi_j)$ is the mass matrix; and $\underline{\hat{f}}$ is the vector of the values of $f(\mathbf{y})$ at the global nodes.

It follows from (4.5) and (4.2) that the matrix $\underline{\mathbf{A}}$ is symmetric and positive-definite. This allows us to use the conjugate gradient iteration to solve (4.10) as discussed Section 4.1.3.

4.1.2 Elemental Constructs

In order to solve the discrete equation (4.10), we form the system matrices $(\underline{\mathbf{A}}, \underline{\mathbf{M}})$ at an elemental (local) level. We then use direct stiffness summation to sum all the elemental contributions of the problem. We first introduce three types of elements: the linear ($\mathcal{P}_1$) tetrahedron; the bilinear ($\mathcal{P}_2$) subparametric tetrahedron; and the bilinear ($\mathcal{P}_2$) isoparametric tetrahedron. We introduce a local to global mapping $g_\alpha^{k_e}$, which takes as input the element number ($k_e = 1, .., \mathcal{K}$) and the local node number ($\alpha = 1, .., N_{local}$, where $N_{local} = 4$ for $\mathcal{P}_1$ and $N_{local} = 10$ for $\mathcal{P}_2$) and outputs the corresponding global node number. A description of tetrahedral elements can be found in many finite element books [50] [27] [29]. In this subsection we follow the discussion of triangular elements presented in the lecture notes of Prof. Patera's course "Computational Fluid Dynamics" [38].

$\mathcal{P}_1$–Linear Tetrahedron

Each linear tetrahedron has four local nodes, one at each vertex. We define a set of barycentric coordinates $(\zeta_1, \zeta_2, \zeta_3, \zeta_4)$ for a point $\mathbf{y}$ in the tetrahedron k_e

$$\begin{aligned} \zeta_1 &= \frac{vol(\mathbf{y}\,2\,3\,4)}{vol^{k_e}} \\ \zeta_2 &= \frac{vol(\mathbf{y}\,1\,3\,4)}{vol^{k_e}} \\ \zeta_3 &= \frac{vol(\mathbf{y}\,1\,2\,4)}{vol^{k_e}} \\ \zeta_4 &= \frac{vol(\mathbf{y}\,1\,2\,3)}{vol^{k_e}}, \end{aligned} \tag{4.12}$$

where $vol(\mathbf{y}\,1\,2\,3)$ is the volume of the tetrahedron formed by the vertices at node 1, node 2, node 3, and point $\mathbf{y}$; and vol^{k_e} is the volume of element k_e. It follows that $0 \leq \zeta_\alpha \leq 1$, $\alpha = 1, 2, 3, 4$ and $\zeta_1 + \zeta_2 + \zeta_3 + \zeta_4 = 1$. Every element Ω^{k_e} is mapped onto the reference element $\hat{\Omega}$ by using the affine transformation (4.12). We write it as $\mathbf{y} = F^{k_e}(\zeta)$ where $\zeta = (\zeta_1, \zeta_2, \zeta_3)$ does not include ζ_4 since only three barycentric coordinates are independent. In matrix form the affine transformation is

$$\zeta_\alpha \;=\; C_\alpha^{k_e} \;+\; \sum_{\beta=1}^{3} D_{\alpha\beta}^{k_e} y_\beta \,, \tag{4.13}$$

where $C_\alpha^{k_e}$ and $D_{\alpha\beta}^{k_e}$, $\alpha = 1,..,4$, $\beta = 1,..,3$, are defined in Appendix B. We also have the inverse of (4.13): $\mathbf{y} = (\mathbf{D}^{k_e})^{-1}\zeta - (\mathbf{D}^{k_e})^{-1}C^{k_e}$, where we exclude the last row of C^{k_e} and $\mathbf{D}^{k_e}$. It follows that $d\mathbf{y} = |\mathbf{J}|d\zeta$ where $\mathbf{J} = det(\mathbf{D}^{k_e})^{-1}$ is the Jacobian. Note that, for this transformation

$$\mathbf{y} \;=\; \sum_{\alpha=1}^{4} \hat{\mathbf{y}}_\alpha^{k_e} \zeta_\alpha \,, \tag{4.14}$$

where $\hat{\mathbf{y}}_\alpha^{k_e}$ is the coordinate vector of local node α of element k_e. Moreover, for a function $\hat{g}^{k_e}(\zeta)$ we have

$$\frac{\partial \hat{g}^{k_e}}{\partial y_m} \;=\; \sum_{i=1}^{3} \frac{\partial \hat{g}^{k_e}}{\partial \zeta_i}\frac{\partial \zeta_i}{\partial y_m} \;=\; \sum_{i=1}^{3} \frac{\partial \hat{g}^{k_e}}{\partial \zeta_i} D_{im}^{k_e} \,. \tag{4.15}$$

At this point we introduce the *elemental* basis functions $h_\alpha(\zeta)$, $\alpha = 1,..,4$

$$h_1 \;=\; \zeta_1 \,, h_2 \;=\; \zeta_2 \,, h_3 \;=\; \zeta_3 \,, h_4 \;=\; 1 - \zeta_1 - \zeta_2 - \zeta_3 \,. \tag{4.16}$$

Thus for any $\hat{v} \in \mathcal{P}_1$, we have

$$\hat{v}(\zeta) \;=\; \sum_{\alpha=1}^{4} \hat{v}_\alpha h_\alpha(\zeta) \,, \tag{4.17}$$

and we have

$$h_\alpha((F^{k_e})^{-1}(\mathbf{y})) \;=\; \phi_{g_\alpha^{k_e}}(\mathbf{y})|_{\Omega^{k_e}} \,. \tag{4.18}$$

The elemental versions of the global matrices $\underline{\mathbf{A}}$ and $\underline{\mathbf{M}}$ are

$$\hat{A}_{\alpha\beta}^{k_e} \;=\; \int_{\Omega^{k_e}} \frac{\partial h_\alpha}{\partial y_m}\frac{\partial h_\beta}{\partial y_m} d\mathbf{y} \,, \tag{4.19}$$

$$\hat{M}_{\alpha\beta}^{k_e} \;=\; \int_{\Omega^{k_e}} h_\alpha h_\beta d\mathbf{y} \,, \tag{4.20}$$

where $m = 1,2,3$; $1 \le \alpha,\beta \le 4$; and we sum over the repeated index m. By

transforming the element Ω^{k_e} to the reference $\hat{\Omega}$, and recognizing that $|\mathbf{J}| = 6\,vol^{k_e}$ we arrive at

$$\hat{A}^{k_e}_{\alpha\beta} = vol^{k_e} \sum_{m=1}^{3} D^{k_e}_{\alpha m} D^{k_e}_{\beta m}\,, \tag{4.21}$$

$$\hat{M}^{k_e}_{\alpha\beta} = \frac{vol^{k_e}}{20}(1+\delta_{\alpha\beta})\,. \tag{4.22}$$

The direct stiffness algorithm used to sum the local contributions is described after the discussion on $\mathcal{P}_2$ elements.

$\mathcal{P}_2$–Bilinear Subparametric Tetrahedron

In order to enrich our finite element space X_h, we pursue second order interpolants over each tetrahedra. We therefore introduce a 10 node element ($N_{local} = 10$), by adding 6 nodes to the linear element at the midpoint of each edge. We still use the barycentric coordinates used for the linear tetrahedron; however, the local basis h_α is now defined to be [27]

$$\begin{aligned}
h_1 &= (2\zeta_1 - 1)\zeta_1\,, & h_6 &= 4\zeta_2\zeta_3 \\
h_2 &= (2\zeta_2 - 1)\zeta_2\,, & h_7 &= 4\zeta_1\zeta_3 \\
h_3 &= (2\zeta_3 - 1)\zeta_3\,, & h_8 &= 4\zeta_1\zeta_4 \\
h_4 &= (2\zeta_4 - 1)\zeta_4\,, & h_9 &= 4\zeta_3\zeta_4 \\
h_5 &= 4\zeta_1\zeta_2\,, & h_{10} &= 4\zeta_2\zeta_4\,.
\end{aligned} \tag{4.23}$$

The elemental matrices are given by (4.19) and (4.20) as before. Since the integrals are not as straightforward to evaluate, we use Gaussian quadrature with np number of integration points $\breve{\zeta}_{\alpha j}$ and weights $\breve{w}_j$, $j = 1, .., np$ defined over the reference element $\hat{\Omega}$. We calculate the integral of a function $\hat{g}(\mathbf{y})$ over Ω^{k_e} as follows

$$\int_{\Omega^{k_e}} \hat{g}(\mathbf{y})d\mathbf{y} \;\approx\; vol^{k_e} \sum_{j=1}^{np} \breve{w}_j \hat{g}(\mathbf{y}(\breve{\zeta}_{1j}, \breve{\zeta}_{2j}, \breve{\zeta}_{3j}, \breve{\zeta}_{4j}))\,, \tag{4.24}$$

In order to integrate a fifth degree polynomial exactly we need $np = 15$ [46]. (The points and weights are given in Appendix B.)

$\mathcal{P}_2$–Bilinear Isoparametric Tetrahedron

The aforementioned elements have a common shortcoming: they cannot represent curved surfaces accurately and, therefore, introduce a skin-error ([45] page 108). For instance, in our case, these elements transform the surface of a sphere into a polygon. To improve this situation, we introduce the isoparametric tetrahedron. In other words, we use the basis h_α defined in (4.23) to represent the geometry as well as any function over $\hat{\Omega}$. We thus have

$$\mathbf{y} \;=\; \sum_{\alpha=1}^{10} \hat{\mathbf{y}}_\alpha^{k_e} h_\alpha(\zeta)\,. \tag{4.25}$$

As a result the Jacobian $\mathbf{J}$ is not constant within an element. The system elemental Laplacian (4.19) can be written as

$$\begin{aligned} \hat{A}_{\alpha\beta}^{k_e} \;=\; \int_{\hat{\Omega}} \frac{1}{|\mathbf{J}|} \Bigg[\left(\sum_{n=1}^{3} E_{\alpha n} a_n^{k_e}\right) \left(\sum_{n=1}^{3} E_{\beta n} a_n^{k_e}\right) + \left(\sum_{n=1}^{3} E_{\alpha n} b_n^{k_e}\right) \left(\sum_{n=1}^{3} E_{\beta n} b_n^{k_e}\right) \\ + \left(\sum_{n=1}^{3} E_{\alpha n} c_n^{k_e}\right) \left(\sum_{n=1}^{3} E_{\beta n} c_n^{k_e}\right) \Bigg] d\zeta\,, \end{aligned} \tag{4.26}$$

where $E_{\alpha n} = \frac{\partial h_\alpha}{\partial \zeta_n}$ and

$$\begin{aligned} a_n^{k_e} \;&=\; \mathbf{J}\frac{\partial \zeta_n}{\partial y_1} \;=\; \left(\frac{\partial y_2}{\partial \zeta_{[n+1]}}\frac{\partial y_3}{\partial \zeta_{[n+2]}} - \frac{\partial y_2}{\partial \zeta_{[n+2]}}\frac{\partial y_3}{\partial \zeta_{[n+1]}}\right)\,, \\ b_n^{k_e} \;&=\; \mathbf{J}\frac{\partial \zeta_n}{\partial y_2} \;=\; \left(\frac{\partial y_1}{\partial \zeta_{[n+2]}}\frac{\partial y_3}{\partial \zeta_{[n+1]}} - \frac{\partial y_1}{\partial \zeta_{[n+1]}}\frac{\partial y_3}{\partial \zeta_{[n+2]}}\right)\,, \\ c_n^{k_e} \;&=\; \mathbf{J}\frac{\partial \zeta_n}{\partial y_3} \;=\; \left(\frac{\partial y_1}{\partial \zeta_{[n+1]}}\frac{\partial y_2}{\partial \zeta_{[n+2]}} - \frac{\partial y_1}{\partial \zeta_{[n+2]}}\frac{\partial y_2}{\partial \zeta_{[n+1]}}\right)\,, \end{aligned} \tag{4.27}$$

where $[m] = m_{mod3}$; and $\frac{\partial y_p}{\partial \zeta_q} = \sum_{\alpha=1}^{10} (\hat{y_p})_\alpha^{k_e} \frac{\partial h_\alpha}{\partial \zeta_q}$ from (4.25). The elemental mass matrix is

$$\hat{M}_{\alpha\beta}^{k_e} = \int_{\hat{\Omega}} h_\alpha h_\beta |\mathbf{J}| d\zeta \,, \tag{4.28}$$

and the Jacobian is

$$\begin{aligned} \mathbf{J} = & \frac{\partial y_1}{\partial \zeta_1}\left(\frac{\partial y_2}{\partial \zeta_2}\frac{\partial y_3}{\partial \zeta_3} - \frac{\partial y_2}{\partial \zeta_3}\frac{\partial y_3}{\partial \zeta_2}\right) - \\ & \frac{\partial y_1}{\partial \zeta_2}\left(\frac{\partial y_2}{\partial \zeta_1}\frac{\partial y_3}{\partial \zeta_3} - \frac{\partial y_2}{\partial \zeta_3}\frac{\partial y_3}{\partial \zeta_1}\right) + \\ & \frac{\partial y_1}{\partial \zeta_3}\left(\frac{\partial y_2}{\partial \zeta_1}\frac{\partial y_3}{\partial \zeta_2} - \frac{\partial y_2}{\partial \zeta_2}\frac{\partial y_3}{\partial \zeta_1}\right) . \end{aligned} \tag{4.29}$$

As for the $\mathcal{P}_2$ subparametric elements, we use Gaussian quadrature to evaluate (4.27) and (4.28).

Note that we can mesh the surface of a sphere accurately since a sphere is described by a quadratic equation. However, when deforming an isoparametric element we need to check that we are not distorting the element too much, which can cause the Jacobian to change sign.

4.1.3 Direct Stiffness Procedure and Iterative Solver

In order to solve (4.10) we use an iterative scheme: the conjugate gradient method [18]. In three dimensions iterative solvers prove to be more efficient than direct solvers, specially in terms of memory requirements. Moreover, the conjugate gradient is robust, automatic, and minimizes data storage even more than other iterative solvers. For simplicity, we report the conjugate gradient for global data structures:

$$\begin{aligned} &\text{initialization}: \; m = 0 \,, \;\; \text{pick } \underline{u}_h^0 \,, \;\; \underline{r}^0 = \underline{mask} \circ (\underline{\mathbf{M}}\underline{\hat{f}} - \underline{\mathbf{A}}\,\underline{u}_h^0) \,, \;\; \underline{w}^0 = \underline{r}^0 \,; \\ &\qquad a^m = (\underline{r}^m, \underline{r}^m)/(\underline{w}^m, \underline{\mathbf{A}}\,\underline{w}^m) \,; \end{aligned} \tag{4.30}$$

$$\underline{u}_h^{m+1} = \underline{u}_h^m + a^m \underline{w}^m \; ; \tag{4.31}$$

$$\underline{r}^{m+1} = \underline{mask} \circ (\underline{r}^m - a^m \underline{\mathbf{A}}\, \underline{w}^m) \; ; \tag{4.32}$$

$$b^m = (\underline{r}^{m+1}, \underline{r}^{m+1})/(\underline{r}^m, \underline{r}^m) \; ; \tag{4.33}$$

$$\underline{w}^{m+1} = \underline{mask} \circ (\underline{r}^m + b^m \underline{w}^m) \; , \tag{4.34}$$

where m is the iteration number; $\underline{u}_h^m$ is the m^{th} iterate of $\underline{u}_h$ which is the vector of unknowns; $\underline{r}^m$ is the residual; $\underline{w}^m$ is the search direction; and $(\cdot\,,\cdot)$ denotes the discrete scalar product. The vector $\underline{mask}$ imposes the Dirichlet boundary conditions on the sphere: if node i is on a sphere then $mask_i = 0$, otherwise $mask_i = 1$, $i = 1, ..., N_{gn}$. Note that $\underline{u}_h^0$ has to be consistent with Dirichlet boundary conditions. The iteration proceeds until a stopping criterion is satisfied; typically, the incomplete iteration error is based on the H^1–seminorm $|\underline{u}_h - \underline{u}_h^m|_{H^1}$, and expressed in terms of the (computable) L^2–norm of the residual [6]. We implement the following stopping criterion

$$\left\{ \sum_{i=1}^{N_{dof}} \frac{(r_i^m)^2}{\tilde{M}_i} \right\}^{\frac{1}{2}} < \frac{\pi}{\lambda} \epsilon_{iter} \; , \tag{4.35}$$

where N_{dof} is the number of degrees-of-freedom of the system; $\tilde{M}_i$ is the "lumped" mass matrix; and ϵ_{iter} bounds the iteration error. In fact, if we define $\underline{\epsilon}^m = \underline{u}_h - \underline{u}_h^m$ to be the iteration error, (4.35) ensures that $\epsilon_{iter} > |\underline{\epsilon}^m|_{H^1}$. The lumped mass matrix is given by

$$\tilde{M}_{i=(g_\alpha^{k_e})} = \sum_{k_e}{}' \, vol^{k_e} \frac{\hat{M}_{\alpha\alpha}^{k_e}}{\sum_{m=1}^{N_{local}} \hat{M}_{mm}^{k_e}} \; , \tag{4.36}$$

where $\hat{M}_{mm}^{k_e}$, $m = 1, \ldots, N_{local}$, is a diagonal component of the local mass matrix; and $\sum_{k_e}'$ represents the direct stiffness operation. Notice that the denominator in (4.36) is the trace of $\hat{\underline{\mathbf{M}}}^{k_e}$.

As mentioned, we actually deal with local data structures, not global ones. Adapting the conjugate gradient to a local data structure is straightforward. All global vectors $(\underline{r}, \underline{u}_h, \underline{w}, \underline{mask})$ are replaced with their local representation. For example, we replace the residual r_i, $i = 1, ..., N_{gn}$ with $r_\alpha^{k_e}$, $\alpha = 1, .., N_{local}$, $k_e = 1, .., \mathcal{K}$. Note

that the scalar product $(\cdot,\cdot)$ is now handled in a slightly different manner. We still multiply the entries of the two arrays and add all of them; however, we need to ensure that we do not count the same degree-of-freedom more than once (for example, a node that is shared by five elements would be counted five times). To avoid the problem we create an array *multi* which, for each local node, gives the number of elements that share that global node. We now multiply the i^{th} $(= g_\alpha^{k_e})$ entries of the two arrays, divide their product by $multi_i$ and add the results.

In practice, we never assemble $\underline{\mathbf{A}}$. Instead, we evaluate $\underline{q} = \underline{\mathbf{A}}\,\underline{s}$, the *action* of $\underline{\mathbf{A}}$ on a vector $\underline{s}$, through our direct stiffness procedure, which on a local level is given by

- calculate the elemental matrix product

  set $q_\alpha^{k_e}$ to zero

  loop through $k_e = 1, ..., \mathcal{K}$

    loop through $\beta = 1, .., N_{local}$

      $q_\alpha^{k_e} = q_\alpha^{k_e} + \hat{A}_{\alpha\beta}^{k_e}\, s_\beta^{k_e}$

- direct stiffness the array $q_\alpha^{k_e}$

  - sum the local contribution of $q_\alpha^{k_e}$ to the global vector q_i:

    set q_i to zero

    loop through $k_e = 1, ..., \mathcal{K}$

      loop through $\alpha = 1, .., N_{local}$

        $i = g_\alpha^{k_e}$

        $q_i = q_i + q_\alpha^{k_e}$

  - Take care of the periodic boundary conditions:

    for a given periodic node, add up all the q_is and write

    the sum back to all the global q_is

  - write back to the local data structure

    loop through $k_e = 1, ..., \mathcal{K}$

      loop through $\alpha = 1, .., N_{local}$

        $i = g_\alpha^{k_e}$

        $q_\alpha^{k_e} = q_i$

The same algorithm is used to calculate the action of the mass matrix $\underline{\mathrm{M}}$.

4.1.4 Mesh Generation

In our mesh generation procedure we adapt the mesh generation modules of FELISA which is a three-dimensional inviscid flow software package [39]. This mesh generator creates an unstructured, linear tetrahedral mesh for the geometry of choice. FELISA uses the advancing front technique to create a mesh. First, it meshes the surfaces of the described geometry with triangles, then it creates tetrahedra by advancing the front from one surface to the next until the entire fluid domain is meshed. The user has control over the mesh spacing by specifying different parameters. First, one must specify the background mesh by using one or more tetrahedra that enclose the entire region to be meshed. We choose to enclose the region to be meshed (Ω_{me}) in one tetrahedra that specifies uniform mesh spacing h throughout Ω_{me}. Second, we use point sources to refine the mesh in certain parts of the domain Ω_{me}. The point source mesh spacing h_{sph} varies according to the inputs h_4,S_C,DD, and the formula

$$h_{sph} = \begin{cases} h_4 & \text{if } r \leq S_C \\ h_4 e^{\left|\frac{r-S_C}{DD-S_C}\right| \ln 2} & \text{if } r > S_C \end{cases}$$

where r is the distance from the location of the point source; S_C is the radius of the sphere centered at the point source in which the mesh spacing is constant; and DD is the distance from the point source at which the mesh spacing is $2h_4$. When one or more point sources are used, FELISA selects $\min(h, h_{sph})$ as the local mesh spacing.

Unfortunately, our version of FELISA does not allow for periodic boundary conditions. In other words, the triangles on opposite faces of the meso-cell cube are not mirror images of each other. In order to overcome this problem we use a two-dimensional triangular mesh generator to mesh one face of the cube [22]. This mesh generator allows us to control the location of the nodes on the edges of the square. Once we have the surface mesh, we copy this face five times to obtain an admissible

cube surface mesh. Subsequently, we input this surface mesh into FELISA and let it mesh the surfaces of the spheres and the volume. Note that we are not able to replicate a mesh on a square generated by FELISA because we have no guarantee that two opposite edges of the square have periodic nodes. Of course FELISA, outputs the coordinates of all the nodes and their local to global mapping $g_\alpha^{k_e}$.

A limitation of our mesh generation procedure is that inclusions cannot intersect the meso-cell cube. Since inclusions are meshed by FELISA and meso-cube surfaces are meshed independently, we would have non-conforming surface meshes where the inclusions intersect the cube. In general we avoid this problem by studying non-intersecting geometries. However, when studying a closed-packed bed of spheres arranged in a simple cubic array we must implement the bounding procedures of Section 3.1. In particular, the lower bound geometry intersects each face of the meso-cell. We create a conforming mesh by exploiting the symmetry of the problem. Figure 4-1 shows the mesh of $\frac{1}{8}$ of the meso-cell volume entirely obtained by FELISA. This mesh is replicated to fill the entire volume resulting in a periodic mesh.

The meshes obtained as described are linear. In order to create a second order subparametric mesh, we insert an extra node at the mid-point of each edge of each tetrahedron. Moreover, to create an isoparametric mesh, we need to search for all the edges of the tetrahedra whose end-nodes are on the sphere and then move the mid-node so that it lays on the sphere instead of inside of it. It has been found that this procedure can distort certain elements so much that the Jacobian J changes sign within those elements, preventing the conjugate gradient from converging. To avoid this problem we act in one of two ways. First, we can refine the mesh in the neighborhood of the sphere surface by introducing a point source at the center of the sphere. Second, we can replace the sphere with a slightly larger one, generate a mesh, and then move all the nodes on the sphere to the surface of the original inclusion. This procedure stretches the elements radially so that less deformation occurs. Both methods solve the problem effectively; however, the first is preferred since we usually desire a more refined mesh around the inclusions.

In Appendix C, we illustrate the method described here by solving Poisson's equa-

tion for heat conduction through a simple cubic array of insulating spheres and deducing the effective conductivity of the medium.

4.2 Porous Media

In this section we present the discretized porous media problem along with the discrete permeability and a discussion of the Uzawa iterative solution scheme.

In solving the porous media problem we discretize the variational weak form (2.23), (2.24). We rewrite it as

$$a(\mathbf{u},\mathbf{v}) - b(p,\mathbf{v}) = (\mathbf{f},\mathbf{v}) \quad \forall \mathbf{v} \in (H^1_{0\#}(\Omega_{me}))^3 \,, \tag{4.37}$$

and

$$-b(q,\mathbf{u}) = 0 \quad \forall q \in L^2_{\#,0}(\Omega_{me}) \,, \tag{4.38}$$

where $\mathbf{u} \in (H^1_{0\#}(\Omega_{me}))^3$ and $p \in L^2_{\#,0}(\Omega_{me})$ are the velocity and pressure solutions respectively. We also use $a(\mathbf{u},\mathbf{v}) = \int_{\Omega_{me}} \frac{\partial u_i}{\partial y_j}\frac{\partial v_i}{\partial y_j} d\mathbf{y}$; $b(p,\mathbf{v}) = \int_{\Omega_{me}} p\frac{\partial v_i}{\partial y_i} d\mathbf{y}$; and $(\mathbf{f},\mathbf{v}) = \int_{\Omega_{me}} \delta_{1i} v_i d\mathbf{y}$. For our finite element approximation we select the $\mathcal{P}_1 - \mathcal{P}_2$ Taylor-Hood element which approximates the pressure p_h with linear ($\mathcal{N}_0 = 1$) polynomials and the velocity field $\mathbf{u}_h$ with second order polynomials ($\mathcal{N}_0 = 2$). This pressure-velocity formulation is chosen because it satisfies the div-stability condition [19]. We introduce two discrete spaces: $Y_h(\Omega_{me}) = \{v|_{\Omega^{k_e}} \in \mathcal{P}_2(\Omega^{k_e})\} \cap H^1_{\#}(\Omega_{me})$; and $W_h(\Omega_{me}) = \{q|_{\Omega^{k_e}} \in \mathcal{P}_1(\Omega^{k_e})\} \cap C_{\#,0}(\Omega_{me})$. Note that the discrete space W_h is continuous since $C(\Omega_{me})$ is the space of all continuous functions. The discrete solution $\mathbf{u}_h \in [Y_h(\Omega_{me})]^3$ and $p_h \in W_h(\Omega_{me})$ satisfy

$$a(\mathbf{u}_h,\mathbf{v}) - b(p_h,\mathbf{v}) = (\mathbf{f},\mathbf{v}) \quad \forall \mathbf{v} \in (Y_h(\Omega_{me}))^3 \,, \tag{4.39}$$

and

$$-b(q,\mathbf{u}_h) = 0 \quad \forall q \in W_h(\Omega_{me}) \,. \tag{4.40}$$

We introduce a tetrahedral mesh consisting of $\mathcal{K}$ elements; N^V_{gn} velocity nodes and

N_{gn}^P pressure nodes. Now we define the velocity basis $\phi_i^V \in Y_h$ and the pressure basis $\phi_i^P \in W_h$. Representing our functions discretely with these bases we obtain from (4.39) and (4.40)

$$\underline{\mathbf{A}}\,\underline{u}_{h_i} - \underline{\mathbf{D}}_i^T\,\underline{p}_h = \underline{\mathbf{M}}\,\underline{\hat{f}}_i\,, \quad i = 1,2,3\,, \tag{4.41}$$

and

$$-\,\underline{\mathbf{D}}_i\,\underline{u}_{h_i} = 0\,, \tag{4.42}$$

where $\underline{\mathbf{A}}$ and $\underline{\mathbf{M}}$ are the same matrices described in Section 4.1 for $\mathcal{P}_2$ elements; and $\underline{\mathbf{D}}_i$ is the discrete divergence operator, which in elemental form is

$$(\hat{D}_i)_{\alpha\beta}^{k_e} \;=\; \int_{\Omega^{k_e}} h_\alpha^P \frac{\partial h_\beta^V}{\partial y_i} d\mathbf{y} \quad \alpha = 1,..,4\,,\ \beta = 1,..,10\,, \tag{4.43}$$

where h_β^V and h_α^P are the $\mathcal{P}_2$ and $\mathcal{P}_1$ elemental interpolants respectively. For uniqueness, we require that the pressure satisfies

$$\sum_{m=1}^{N_{gn}^V} p_{h_m} \;=\; 0\,. \tag{4.44}$$

Finally, the discrete permeability of (2.15) can be written as

$$\kappa_h^P \;=\; \frac{1}{\lambda^3}\,\underline{1}^T\,\underline{\mathbf{M}}\,\underline{u}_{h_1}\,. \tag{4.45}$$

We can also write

$$\kappa_h^P \;=\; \frac{1}{\lambda^3}\,\underline{u}_{h_i}^T\,\underline{\mathbf{A}}\,\underline{u}_{h_i}\,, \tag{4.46}$$

where we sum over $i = 1,2,3$. Equation (4.46) is obtained by multiplying (4.41) by $\underline{u}_{h_i}^T$; summing over the repeated index i; and realizing that $\underline{u}_{h_i}^T\underline{\mathbf{D}}_i^T = (\underline{\mathbf{D}}_i\,\underline{u}_{h_i})^T = 0$. Obviously, we can calculate κ_h^P both ways and compare the results to ensure that the code is behaving correctly.

We define an error $E_h^P \equiv |\kappa - \kappa_h^P|$ which can be written as

$$E_h^P \;\approx\; \frac{1}{\lambda^3}|a(\mathbf{u},\mathbf{u}) - a(\mathbf{u}_h,\mathbf{u}_h)|\,. \tag{4.47}$$

The approximation sign is due to the skin-error introduced by subparametric meshes and the quadrature errors introduced by isoparametric elements. Note that by selecting $\mathbf{v} = \mathbf{u}$ in (4.37) and $\mathbf{v} = \mathbf{u}_h$ in (4.39); using (4.38) and (4.40); subtracting the resulting equations; and taking the absolute value we get

$$|a(\mathbf{u},\mathbf{u}) - a(\mathbf{u}_h,\mathbf{u}_h)| \;=\; |(\mathbf{f},\mathbf{u}-\mathbf{u}_h)|\,, \tag{4.48}$$

in the absence of quadrature errors. Evoking the Cauchy-Schwartz inequality [18] to bound the right hand side of (4.48), we have

$$|a(\mathbf{u},\mathbf{u}) - a(\mathbf{u}_h,\mathbf{u}_h)| \;\leq\; ||\mathbf{f}||_{L^2}||\mathbf{u}-\mathbf{u}_h||_{L^2}\,, \tag{4.49}$$

which in view of (4.47) gives

$$E_h^P \;\leq\; \frac{1}{\lambda^3}||\mathbf{f}||_{L^2}||\mathbf{u}-\mathbf{u}_h||_{L^2}\,, \tag{4.50}$$

where $||\mathbf{v}||_{L^2} = \left(\int_{\Omega_{me}} \mathbf{v}\cdot\mathbf{v}d\mathbf{y}\right)^{1/2}$ is the L^2 norm. Equation (4.50) shows that the permeability error E_h^P is bounded by the finite element discretization error in L^2, which is $O(h^2)$ for linear elements and $O(h^3)$ for second order elements; where h is the mesh spacing.

In order to solve for the discrete velocities and pressure we implement the Uzawa saddle-decoupling algorithm [35]. To obtain the saddle-decomposition, we multiply equation (4.41) by $\underline{\mathbf{D}}_i\underline{\mathbf{A}}^{-1}$ and use (4.42) to obtain

$$\underline{\mathbf{S}}\,\underline{p}_h = -\,\underline{\mathbf{D}}_i\,\underline{\mathbf{A}}^{-1}\underline{\mathbf{M}}\,\underline{\hat{f}}_i\,,\; i=1,2,3\,, \tag{4.51}$$

and

$$\underline{\mathbf{A}}\,\underline{u}_{h_i} = \underline{\mathbf{D}}_i^T\,\underline{p}_h + \underline{\mathbf{M}}\,\underline{\hat{f}}_i\,,\; i=1,2,3\,. \tag{4.52}$$

where $\underline{\mathbf{S}} \equiv \underline{\mathbf{D}}_i\,\underline{\mathbf{A}}^{-1}\underline{\mathbf{D}}_i^T$ is a symmetric, positive–definite matrix. We solve (4.51) for the pressure field using a procedure that relies on the conjugate gradient algorithm. First, we compute the forcing term by solving $\underline{\mathbf{A}}\,\underline{g}_i = \underline{\mathbf{M}}\,\underline{f}_i$ for $\underline{g}_i$ using the conjugate

gradient method; then we simply carry out the multiplication $\underline{\mathbf{D}}_i \underline{g}_i$. Second, we implement an *outer* conjugate gradient iteration in which the matrix to be inverted is $\underline{\mathbf{S}}$. To evaluate the action of $\underline{\mathbf{S}}$ on a vector $\underline{q}$ we rely on three *inner* conjugate gradient solves used as follows

$$\begin{aligned} \underline{t}_i &= \underline{\mathbf{D}}_i^T \underline{q}\,, \\ \underline{\mathbf{A}}\,\underline{z}_i &= \underline{t}_i\,, \text{(solved by conjugate gradient iteration)} \\ \underline{\mathbf{S}}\,\underline{q} &= \underline{\mathbf{D}}_i\,\underline{z}_i\,. \end{aligned} \tag{4.53}$$

Once the pressure is determined, we solve (4.52) for the velocity unknowns through the use of yet another conjugate gradient iteration. Finally, we use either (4.45) or (4.46) to determine the permeability. Note that when the local mesh spacing h varies considerably within the meso-scale mesh, it is convenient to precondition the outer pressure solver [18]. The diagonal lumped pressure mass matrix is a simple and efficient preconditioner.

In closing the section, we mention the micro-scale implementation. It is actually trivial: once the geometry has been altered, we mask all the nodes on the surface of the inclusions and proceed as usual.

4.3 Sedimentation

We rewrite the sedimentation problem (2.48)-(2.50) as

$$a'(\mathbf{u},\mathbf{v}) - b(p',\mathbf{v}) = c\,(\mathbf{f},\mathbf{v}) - (1-c)\,l(\mathbf{v}) \quad \forall \mathbf{v} \in Y\,, \tag{4.54}$$

$$-\,b(q,\mathbf{u}) = 0 \quad \forall q \in L^2_{\#,0}(\Omega_{me})\,, \tag{4.55}$$

$$-\,\eta\,[(\mathbf{f},\mathbf{u}) + l(\mathbf{u})] \;=\; 0 \quad \forall \eta \in \mathcal{R}\,, \tag{4.56}$$

where $\mathbf{u} \in Y$ and $p' \in L^2_{\#,0}(\Omega_{me})$ are the velocity and pressure solutions respectively. We also have used $a'(\mathbf{u},\mathbf{v}) = \int_{\Omega_{me}} \frac{\partial v_i}{\partial y_j}\left(\frac{\partial u_i}{\partial y_j} + \frac{\partial u_j}{\partial y_i}\right) d\mathbf{y}$; $(\mathbf{f},\mathbf{v}) = \int_{\Omega_{me}} \delta_{2i} v_i d\mathbf{y}$; and $l(\mathbf{v}) =$

$\frac{\pi}{6}\sum_{k=1}^{N}(V_2)_k$, where $(V_2)_k$ is such that $\mathbf{v}|_{\partial\Omega_k} = \mathbf{V}_k + \mathbf{Z}_k \times (\mathbf{y} - \mathbf{y}_k)$, $k = 1, .., N$ as in (2.41).

Since we are still dealing with Stokes flow, we select the $\mathcal{P}_1 - \mathcal{P}_2$ Taylor-Hood element for our finite element discretization. Again, we introduce a tetrahedral mesh consisting of $\mathcal{K}$ elements; N_{gn}^V velocity nodes and N_{gn}^P pressure nodes. We also introduce two discrete spaces: $Y_h^S(\Omega_{me}) = \{v|_{\Omega^{k_e}} \in \mathcal{P}_2(\Omega^{k_e})\} \cap Y$; and $W_h^S(\Omega_{me}) = \{q|_{\Omega^{k_e}} \in \mathcal{P}_1(\Omega^{k_e})\} \cap C_{\#,0}(\Omega_{me})$. Now we define the velocity basis $\phi_i^V \in Y_h^S$ and the pressure basis $\phi_i^P \in W_h^S$. Note that our velocity basis is such that $\phi_i^V(\mathbf{y}_j) = \delta_{ij}$, $1 \leq i, j \leq N_{dof}$, where $N_{dof} = N_{gn}^V - N_{surf} + 6N$ is the number of one component velocity degrees-of-freedom of the finite element mesh; and N_{surf} is the number of nodes on the spheres. In fact, all the nodes that are on the surface of a sphere (slave nodes) represent six degrees-of-freedom (master nodes). Since the bases have to be nodal, we introduce a master-slave mapping matrix $\underline{\mathbf{Q}}$ that transforms the six master degrees-of-freedom into slave nodal values that are compatible with solid body motion of the sphere [1]. We use $\underline{\mathbf{Q}}$ in the following way

$$\underline{v}_h \;=\; \underline{\mathbf{Q}}\,\underline{v}_h^{master}\,, \tag{4.57}$$

where $\underline{v}_h$ has length $3N_{gn}^V$ and $\underline{v}_h^{master}$ has length $3N_{dof}$. Note that in the sedimentation formulation we need to merge all three velocity components into one vector since the operator $a'(\cdot,\cdot)$ couples the three directions.

Representing our functions discretely with these bases we obtain

$$\underline{\mathbf{Q}}^T\underline{\mathbf{A}}\,\underline{\mathbf{Q}}\,\underline{u}_h^{master} - \underline{\mathbf{Q}}^T\underline{\mathbf{D}}^T\underline{p}_h' \;=\; \underline{\mathbf{Q}}^T c\underline{\mathbf{B}}\underline{f} - (1-c)\underline{\mathbf{L}}\,, \tag{4.58}$$

$$-\underline{\mathbf{D}}\,\underline{\mathbf{Q}}\,\underline{u}_h^{master} \;=\; 0\,, \tag{4.59}$$

$$\underline{1}^T\underline{\mathbf{B}}\,\underline{\mathbf{Q}}\,\underline{u}_h^{master} + \frac{\pi}{6}\sum_{k=1}^{N}(U_2)_k \;=\; 0\,, \tag{4.60}$$

where $\underline{\mathbf{A}}$, $\underline{\mathbf{D}}$ and $\underline{\mathbf{B}}$ operate on the finite element nodes (i.e. the mesh nodes), and $\underline{\mathbf{L}}$ operates on the velocity master degrees-of-freedom. In principle, instead of storing three matrices to evaluate $\underline{\mathbf{Q}}^T\underline{\mathbf{A}}\,\underline{\mathbf{Q}}\,\underline{v}_h^{master}$ we could create one matrix $\underline{\mathbf{A}}' = \underline{\mathbf{Q}}^T\underline{\mathbf{A}}\,\underline{\mathbf{Q}}$

and then evaluate $\underline{\mathbf{A}}'\underline{v}_h^{master}$. However, it is easier to evaluate $\underline{\mathbf{Q}}\underline{v}_h^{master}$ and $\underline{\mathbf{Q}}^T\underline{v}_h$, than $\underline{\mathbf{Q}}^T\underline{\mathbf{A}}$. For this reason, we keep the matrices separate. (See Appendix B for the elemental constructs of $\underline{\mathbf{Q}}$, $\underline{\mathbf{Q}}^T$, and $\underline{v}_h$.)

The discrete Laplacian $\underline{\mathbf{A}}$ differs from the discrete operator of the Poisson problem. At an elemental level, the Laplacian can be written as the sum of two parts: $\hat{A}^{k_e}_{\alpha\beta} = \tilde{\tilde{A}}^{k_e}_{\alpha\beta} + \tilde{A}^{k_e}_{\alpha\beta}$. The two components are given by

$$\tilde{\tilde{A}}^{k_e}_{(\alpha=i\cdot\gamma)(\beta=j\cdot\psi)} = \delta_{ij}\int_{\Omega^{k_e}} \frac{\partial h_\gamma}{\partial y_m}\frac{\partial h_\psi}{\partial y_m}d\mathbf{y}\,, \tag{4.61}$$

$$\tilde{A}^{k_e}_{(\alpha=i\cdot\gamma)(\beta=j\cdot\psi)} = \int_{\Omega^{k_e}} \frac{\partial h_\gamma}{\partial y_i}\frac{\partial h_\psi}{\partial y_j}d\mathbf{y}\,, \tag{4.62}$$

where $(i,j) = 1,2,3$ are the coordinate directions; and $(\gamma,\psi) = 1,..,10$. It should be noticed that $\hat{A}^{k_e}_{\alpha\beta}$ is a 30 by 30 matrix for each element k_e instead of being a 10 by 10 as for the permeability problem. The matrix $\hat{D}^{k_e}_{\alpha\beta}$, $\alpha = 1,..,4$, $\beta = 1,..30$, is simply given by

$$\underline{\hat{\mathbf{D}}}^{k_e} = (\underline{\hat{\mathbf{D}}}_1^{k_e}\ \underline{\hat{\mathbf{D}}}_2^{k_e}\ \underline{\hat{\mathbf{D}}}_3^{k_e})\,, \tag{4.63}$$

where $\underline{\hat{\mathbf{D}}}_i^{k_e}$ is given by (4.43). Finally, $\underline{\mathbf{B}}$ in elemental form is

$$\hat{B}^{k_e}_{(\alpha=i\cdot\gamma)(\beta=j\cdot\psi)} = \delta_{2i}\delta_{2j}\hat{M}^{k_e}_{\gamma\psi} \qquad \alpha,\beta = 1,..,30\,. \tag{4.64}$$

The vector $\underline{\mathbf{L}} = (\underline{\mathbf{L}}_1^T\ \underline{\mathbf{L}}_2^T\ \underline{\mathbf{L}}_3^T)^T$ is, on a global level, given by

$$(L_i)_j = \begin{cases} \delta_{2i}\frac{\pi}{6} & \text{if } j \text{ is a sphere translational degree-of-freedom} \\ 0 & \text{otherwise} \end{cases} \tag{4.65}$$

where $i = 1,2,3$, $j = 1,..,N_{dof}$. The local representation of $\underline{\mathbf{L}}$ is similar to that of $\underline{v}_h^{master}$ described in Appendix B: we have $(L^{master})^{k_e}_\alpha$, $\alpha = 1,..,30$, $k_e = 1,..,\mathcal{K}$, and $(L^{VW,master})^k_\gamma$, $\gamma = 1,..,6$, $k = 1,..,N$. The former array is zero, and the latter is $(L^{VW,master})^k_\gamma = \delta_{2\gamma}\frac{\pi}{6}$. Note that the right hand side of (4.58) is obtained in three steps. First, we calculate $c\underline{\mathbf{B}}\underline{f}$ on the slave degrees-of-freedom. Second, we map the

slave degrees-of-freedom onto the master degrees-of-freedom by operating with $\underline{\mathbf{Q}}^T$ (i.e. $\underline{\mathbf{Q}}^T c\underline{\mathbf{B}}\underline{f}$). Finally, we subtract $(1-c)\underline{\mathbf{L}}$ to obtain the right hand side forcing term.

The solution of (4.58)-(4.60) is obtained using the Uzawa algorithm described in the previous section. The saddle-decomposition is obtained by multiplying (4.58) by $\underline{\mathbf{D}}\underline{\mathbf{Q}}(\underline{\mathbf{Q}}^T\underline{\mathbf{A}}\underline{\mathbf{Q}})^{-1}$. The result is

$$\underline{\mathbf{S}}\,\underline{p}'_h = -\underline{\mathbf{D}}\underline{\mathbf{Q}}(\underline{\mathbf{Q}}^T\underline{\mathbf{A}}\underline{\mathbf{Q}})^{-1}(\underline{\mathbf{Q}}^T c\underline{\mathbf{B}}\underline{f} - (1-c)\underline{\mathbf{L}})\,, \tag{4.66}$$

$$(\underline{\mathbf{Q}}^T\underline{\mathbf{A}}\underline{\mathbf{Q}})\,\underline{u}_h^{master} = \underline{\mathbf{Q}}^T(\underline{\mathbf{D}}^T\,\underline{p}'_h + c\underline{\mathbf{B}}\underline{f}) - (1-c)\underline{\mathbf{L}}\,, \tag{4.67}$$

where $\underline{\mathbf{S}} = \underline{\mathbf{D}}\underline{\mathbf{Q}}(\underline{\mathbf{Q}}^T\underline{\mathbf{A}}\underline{\mathbf{Q}})^{-1}\underline{\mathbf{Q}}^T\underline{\mathbf{D}}^T$. Note that the inner and outer conjugate gradients invert $(\underline{\mathbf{Q}}^T\underline{\mathbf{A}}\underline{\mathbf{Q}})$ and $\underline{\mathbf{S}}$ respectively, which are both positive-definite matrices. Moreover, in sedimentation, $mask_i = 1$ for every node since there is no Dirichlet boundary condition.

Periodicity is achieved through the direct stiffness summing procedure, which is the same as the one described in Section 4.1. Direct stiffness is implemented on any local vector (actually, any two dimensional array for our elemental constructs) that is the result of the product of a local matrix (three-dimensional array) with a local vector. Operating with $\underline{\mathbf{Q}}$ and $\underline{\mathbf{Q}}^T$ does not require direct stiffness since these are just master-slave "mappings".

Equation (4.60) is implemented similarly to the uniqueness conditions on the velocities (2.31) and on the pressure (2.32). For example, (4.60) is satisfied by calculating the value of the left hand side with the velocity results of a given iteration, and subtracting the result (divided by the volume of the cube) from the velocity field. In infinite precision arithmetic, (4.60) need only be satisfied after the solver that inverts $(\underline{\mathbf{Q}}^T\underline{\mathbf{A}}\underline{\mathbf{Q}})$ has converged. However, to ensure that the conjugate gradient iteration converges in finite precision arithmetic, we satisfy condition (4.60) every, say, 100 iterations. Note that when integrating over the fluid region Ω_{me} with the mass matrix, we are integrating over a volume $\mathcal{V}_{me,h}$ which differs slightly from the continuous one $\mathcal{V}_{me}$. In the continuous formulation, the solvability of the variational

weak form (2.44)-(2.46) is guaranteed, in part, by the backflow pressure gradient $\tau = \frac{N\mathcal{W}}{\lambda^3}$ (Section 2.3). In the discrete formulation, solvability is guaranteed by a discrete backflow pressure gradient $\tau_h = \frac{N\mathcal{W}}{N\pi d^3/6+\mathcal{V}_{me,h}}$. Non-dimensionally, τ_h is equivalent to the discrete porosity $c_h = \frac{N\pi d^3/6}{N\pi d^3/6+\mathcal{V}_{me,h}}$. It follows that we have to replace the volume fraction c with c_h in (4.66) and (4.67).

Finally, we discuss the implementation of the micro-scale models described in Section 3.2 for the case of two inclusions in the meso-cell ($N = 2$). The lower bound is obtained by rigidly connecting the spheres, thus creating a "dumbbell". The variational weak form of the problem is given by (2.49),(3.34) and (3.37). After having created a mesh, we treat the dumbbell as one particle with six degrees-of-freedom and a center of mass located at the mid-point of the segment that joins the centers of the spheres. The appropriate saddle problem is

$$\underline{\mathbf{S}}\,\underline{p}'_h = -\underline{\mathbf{D}}\underline{\mathbf{Q}}(\underline{\mathbf{Q}}^T\underline{\mathbf{A}}\underline{\mathbf{Q}})^{-1}(\underline{\mathbf{Q}}^T c_h\underline{\mathbf{B}}\underline{f} - 2(1-c'_h)\underline{\mathbf{L}})\,, \tag{4.68}$$

$$(\underline{\mathbf{Q}}^T\underline{\mathbf{A}}\underline{\mathbf{Q}})\,\underline{u}_h^{master} = \underline{\mathbf{Q}}^T(\underline{\mathbf{D}}^T\,\underline{p}'_h + c_h\underline{\mathbf{B}}\underline{f}) - 2(1-c'_h)\underline{\mathbf{L}}\,, \tag{4.69}$$

where $c'_h = \frac{2\pi d^3/6+\mathcal{V}_{nip}}{2\pi d^3/6+\mathcal{V}_{nip}+\mathcal{V}_{me,h}}$ is the discrete dumbbell volume fraction; and $\mathcal{V}_{nip}$ is the continuous volume of the part of the dumbbell between the two spheres before it is meshed. Of course, the zero net flowrate condition changes to

$$\underline{1}^T\underline{\mathbf{B}}\underline{\mathbf{Q}}\underline{u}_h^{master} + (2\frac{\pi}{6} + \frac{\mathcal{V}_{nip}}{d^3})(U_2)_{N_D} \;=\; 0\,, \tag{4.70}$$

where $k = N_D$ is the dumbbell.

Since the upper bounds are achieved by decreasing the radii of the two spheres, we do not need to make any changes to (4.66), (4.67) or (4.60) provided we use the discrete concentration of the shrunk spheres, and use (3.63) when comparing the upper bound settling speed to the actual settling speed of the original suspension.

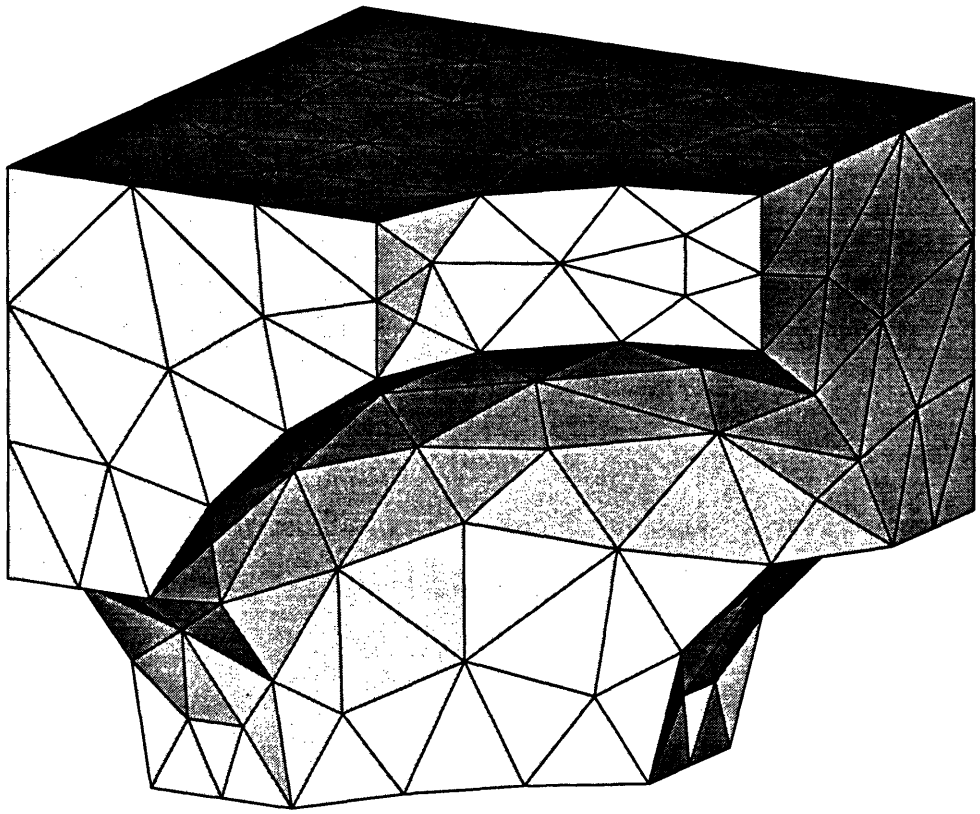

Figure 4-1: Mesh of one-eight of the lower bound geometry for a simple cubic array of spheres (porous media).

Chapter 5

Results and Conclusions

In this chapter we present and discuss our results and make some conclusions. In Section 5.1 we present the porous media results for a simple cubic array of spheres and validate them with well known analytical solutions. We are able to reach maximum packing density and discuss low-Reynolds-number fluidization by using the micro-scale treatment of Section 3.1. In Section 5.2 the sedimentation methodology is validated by relating the porous media results to the settling velocity of a simple cubic array of spheres. We then look at the settling of two spheres in a meso-scale cell and compare the results with that of a pair of spheres settling in an infinite fluid. Subsequently, we implement the bounding procedures of Section 3.2 for the two sphere case. Finally, the qualitative behavior of three spheres in the meso-cell is discussed. In Section 5.3 we summarize our studies and make some conclusions which are followed by suggestions on future work (Section 5.4).

Note that all the numerical results presented in this chapter are dimensionless; however, for the purpose of discussion, lengths are in reference to a meso-cell cube of unit edge.

5.1 Porous Media Results

5.1.1 Numerical Results

Exact results for creeping flow through a simple cubic array of spheres are obtained by Zick & Homsy [49] in the form of a drag coefficient K defined as

$$K \equiv \frac{D}{D_{STOKE}}, \tag{5.1}$$

where D_{STOKE} is the Stokes drag on a sphere moving at a constant speed U_∞ in an unbounded fluid, and D is the drag on a sphere in the simple cubic array moving at the same speed U_∞ in a quiescent fluid. The drag coefficient can be related to the permeability quite simply. First, a momentum balance on the meso-scale cell tells us that the pressure force induced by the macroscopic pressure gradient $\Delta P/L$ balances the drag force D. Second, through Darcy's law $U_\infty = -\frac{\kappa}{\mu}\frac{\Delta P}{L}$ we relate the drag to the dimensionless permeability:

$$\kappa = \frac{1}{18cK}. \tag{5.2}$$

Table 5.1 shows the permeability results obtained by Zick & Homsy versus ours for different sphere concentrations. It is apparent that the results are in good agreement.

To ensure that our code behaves correctly, we observe how a suitable error norm behaves as the mesh size is refined for a given concentration c. This test, known as a convergence test, is shown in figure 5-1 as a log-log plot of the error E_h^P versus the nominal mesh spacing h for a concentration $c = 0.125$. The error is defined as (see Section 4.2)

$$E_h^P \equiv \mid \kappa - \kappa_h^P \mid, \tag{5.3}$$

where κ is the exact permeability and κ_h^P is the finite element discrete permeability. Note that in the absence of skin-errors, the discrete solution κ_h^P cannot be greater than the exact solution κ since the finite element method finds the maximum of

J_Ω^P over a restricted class of functions (i.e. polynomials). Indeed, this is what we observe when using isoparametric elements as opposed to subparametric elements which overestimate the permeability since they reduce the volume of the sphere.

The data of figure 5-1 is obtained by using isoparametric and subparametric $\mathcal{P}_2 - \mathcal{P}_1$ (Taylor-Hood) tetrahedral elements with a nominal mesh spacing h that varies from 0.17 to 0.07 (from about 3,000 to 25,000 one-component velocity degrees-of-freedom) in a cube of unit side. The calculations are made on a high-end HP 9000 workstation and take from several minutes to several hours of CPU time. Finite element theory predicts that $O(h^3)$ convergence should be observed for Taylor-Hood elements [50] [45], since E_h^P is a measure of the L^2 norm (see (4.50)). Indeed, figure 5-1 shows that the convergence rate is about three for isoparametric elements. However, subparametric elements exhibit second order convergence. This is probably due to the skin-error associated with the surface mesh of the sphere. Notice that inequality (4.50) might not be sharp, hence E_h^P might *potentially* converge faster than $O(h^3)$ for Taylor-Hood elements. In any case, the convergence rates seem well behaved and posses the correct trends: smaller errors for isoparametric compared to subparametric elements and decrease in error as the mesh is refined.

In order to achieve maximum packing density ($c = 0.5236$), we must implement the geometry changes described in Section 3.1, since a mesh cannot be generated when the sphere touches the sides of the meso-cell. Table 5.2 shows the bounds on the permeability obtained with two different nip diameters. Note that as the nip region increases in size (diameter increases) the bounds get more crude (Section 3.1) and the problem, having fewer degrees-of-freedom, is easier to solve. Figure 5-2 depicts part of a mesh for the lower bound geometry.

5.1.2 Physical Results

As described in the previous section, we have succeeded in reproducing the well known results for permeability in simple cubic arrays. Although the selected geometry seldom models the spatial distribution of inclusions in real porous media, it can still lead to interesting analyses. For instance, we can relate the permeability of a packed bed to

the concept of minimum fluidization velocity $U_{mf} = \frac{1}{\lambda^3}\int_{\Omega_{me}}(u_1)_{mf}dy$ [11], which is that average fluid velocity that creates a pressure drop across a packed bed of particles such that the pressure drop balances the buoyancy corrected weight of the particles. It is typically expected that a velocity greater than U_{mf} leads to fluidization. Using Darcy's law, we can write the pressure drop in terms of the minimum fluidization velocity, the fluid viscosity, and the permeability. We thus have

$$Re_{mf} = \kappa c\,(Ga\,Mv)\,, \tag{5.4}$$

where $Re_{mf} = \frac{\rho_{co}U_{mf}d}{\mu_{co}}$ is the fluidization Reynolds number; $Ga = \frac{d^3 g \rho_{co}^2}{\mu_{co}^2}$ is Galileo's number; and $Mv = \frac{\rho_{di}-\rho_{co}}{\rho_{co}}$. For cubic centered spheres (5.4) reads

$$Re_{mf} = 1.32 \cdot 10^{-3}(Ga\,Mv)\,, \tag{5.5}$$

where $(\kappa c) = 1.32 \cdot 10^{-3}$ is obtained by using $\kappa = 0.002520$ and $c = 0.5236$.

Empirical correlations that relate Re_{mf}, Ga and Mv are abundant in the literature; many of them can be found in Davidson, Clift & Harrison [11]. Unfortunately, most of the formulas are not linear in $(GaMv)$ since they account for flow regimes that range from low to intermediate Reynolds numbers. Nevertheless, among those formulas that are linear, we find that the empirical coefficient (κc) varies from $8 \cdot 10^{-4}$ to $8 \cdot 10^{-3}$ for different types of randomly packed beds, which shows that our estimate is of the correct order of magnitude. The empirical coefficient is most probably a strong function of the spatial distribution of the particles.

5.2 Sedimentation Results

5.2.1 Numerical Results

We start by analyzing the sedimentation of a simple cubic array of spheres and compare the results to the porous media ones, since, for this geometry, the two problems are equivalent. In fact, both flows are caused by a pressure gradient: in porous media flow, the pressure gradient is imposed, whereas in sedimentation it is caused by the

buoyancy corrected weight of the particles (i.e. the backflow pressure gradient). Relating the settling speed of a simple cubic array to the permeability is fairly simple. First, we adopt a coordinate system that is fixed on a sedimenting sphere and notice that

$$u_{2,permea} = u_{2,sed} - U_2 \ , \tag{5.6}$$

where $u_{2,permea}$ and $u_{2,sed}$ are the *dimensional* velocity fields in the $\mathbf{e}_2$ directions for the permeability and sedimentation problems respectively; and U_2 is the coordinate system shift (i.e. the vertical velocity of a sphere). Second, we use Darcy's law $< u_{2,permea} >= -\frac{\kappa}{\mu_{co}} \frac{\Delta P}{L}$; where $< u_{2,permea} >= \frac{1}{\lambda^3} \int_{\Omega_{me}} u_{2,permea} dy$ can be written as $< u_{2,permea} >= -U_2$ by using (5.6) and the zero net volume flowrate condition (2.30); and $\frac{\Delta P}{L} = -\tau = \frac{\mathcal{W}}{\lambda^3}$ in sedimenting flows. By non-dimensionalizing all quantities, it follows that

$$\kappa^* = -\frac{U_2^*}{c} = \frac{\mathcal{U}^*}{c} \ , \tag{5.7}$$

for simple cubic arrays, where we have used the superscript (*) to emphasize that all quantities are dimensionless.

Figure 5-3 is a plot of $E_h^S \equiv |\kappa - \kappa_h^S|$ versus h for a concentration of $c = 0.125$ for isoparametric $\mathcal{P}_2 - \mathcal{P}_1$ elements, where $\kappa_h^S = \frac{\mathcal{U}_h}{c}$. The mesh size goes from $h = 0.15$ to $h = 0.091$ in a meso-cell of unit side. The CPU time ranges from one hour to half a day. The data points seem to suggest third order convergence as expected, since E_h^S is a measure of the discretization error $||\mathbf{u} - \mathbf{u}_h||_{L^2}$.

Table 5.3 shows the sedimentation results compared to the porous media results. Although the numerical permeability data points are close, they do not coincide. The reason for this is that, although the formulations are equivalent in a continuous sense, they are not in the discrete sense. In fact, in the porous media numerical procedure we *force* the velocity to be zero on the sphere boundary, whereas in the sedimentation numerical procedure we require force and torque balances on the sphere. Note that we do not attempt to implement the nip-region bounds to achieve maximum packing

density because the lower bound would imply that each sphere in the array is connected to six others. Although the bound would work, it is a very contrived situation: in real sedimenting flows we would not rigidly connect the entire suspension. Figure 5-4 is a plot of permeability versus concentration for our results and the analytical ones. Note that the three sets of results are virtually indistinguishable from each other, and that we have included the porous media maximum packing density result as a vertical "error-bar" that represents the crudest of the bounds of table 5.2.

Next, we include a pair of particles in the meso-scale cell. Although this situation is far from simulating the real random sedimentation problem, it shows some interesting features of Stokes flow, which are discussed in Section 5.2.2. In this subsection we only report numerical results. For instance, take the case of a meso-cell with edges of unit length and two spheres of diameter $d = 0.1$ separated by an inter-center distance $l_d = 0.2$. We analyze three cases corresponding to three orientations of the line connecting the centers of the spheres. In all three cases the centers of the spheres are on the $y_3 = 0.5$ plane. Figure 5-5a shows the surface mesh for case 1 which corresponds to the line of centers being perpendicular to the gravity vector. In case 2 the line of centers is parallel to gravity which points in the $-y_2$-direction (figure 5-5b). Finally, figure 5-5c shows case 3 where the line of centers makes a $\frac{\pi}{4}$ angle with the horizontal. Table 5.4 summarizes the translational and rotational degrees-of-freedom of each particle for the three cases. The meshes are obtained by using a point source at each sphere center and the parameters: $h = 0.15, h_4 = 0.03, S_C = 0.10, DD = 0.15$ which result in about 7,000 elements (10,000 degrees-of-freedom for each velocity component). In addition, we keep the pair centered in the meso-cell. Note that we have tried various sphere arrangements such that the pair is at a non-zero angle with the $y_3 = 0.5$ plane and found that our results remain largely invariant.

Although the three discussed cases do not require the micro-scale treatment of Section 3.2, we implement bounding procedures anyway to take advantage of the relatively high viscous dissipation that takes place in the nip region between the particles. Thus, we expect that the bounds will have noticeable effects. For each of the original cases we introduce the lower and the upper bound analysis. The

lower bound is obtained by connecting the pair of spheres with a cylinder of diameter $d_c = 0.08$. Note that we now have one particle: the dumbbell. The upper bound is obtained by shrinking both spheres to a diameter $d' = 0.08$. While the mesh parameters for the dumbbell remain the same, the ones for the upper bound become: $h = 0.15, h_4 = 0.025, S_C = 0.08, DD = 0.13$ which result in about 7,000 elements. Table 5.5 shows the dumbbell motions, and table 5.6 shows the results for two spheres of diameter d'. Recall from Section 3.2.2 that to obtain the settling velocity bound from table 5.6 we need to multiply $(U_2)_k$ by $\frac{d}{d'}$ as shown in (3.63).

Finally, we show the bounds for the settling speeds in table 5.7. As mentioned, the three analyzed cases are not geometrically stiff, so implementing the bounding procedures does not decrease the number of degrees-of-freedom significantly. When the gap between the spheres is smaller, the bounds become sharper and the number of degrees-of-freedom decreases appreciably.

5.2.2 Physical Results

The simple cubic array case is very useful in validating our code. One interesting aspect of this well-known flow is that the settling velocity of the array is always smaller than the Stokes velocity, which in non-dimensional form is $\mathcal{U}_{STOKE} = \frac{1}{18}$. In the limit of $c \to 0$ we recover this result; for example, the smallest concentration we reach is $c = 0.000268$, and the settling speed of this array is $\mathcal{U}_h = 0.04867$, which is less than, but close to, $\mathcal{U}_{STOKE} = 0.05556$. The lowest settling speed is achieved at the maximum concentration $c = 0.5236$. In this close-packed limit, the settling speed is $\mathcal{U} = \kappa c = 1.32 \cdot 10^{-3}$ which is clearly less than $\mathcal{U}_{STOKE}$. This phenomena, known as hindered settling, is common to all sedimentation processes that occur in any kind of impermeable container. In fact, the upward flow of fluid retards the motion of the suspension, so N particles in a meso-cell fall slower than the same N particles in an unbounded fluid. Note that sedimentation in unbounded fluids has a peculiar behavior: since each additional particle drags along with it some fluid and therefore other particles, an infinite number of particles falls at an infinite speed [21].

The hindered settling argument applies to the pair of spheres discussed in the

previous subsection. In fact, Happel & Brenner report analytical results for two spheres falling in an unbounded fluid [21] obtained using the method of reflections. It can be shown that our spheres are slower than the ones in the analytical study. For example, when the sphere centers are separated by a distance that is three times their radius, the analytical study predicts that the settling speeds are $\mathcal{U}_{HP,hor} = 0.07059$ when the line of centers is horizontal, and $\mathcal{U}_{HP,ver} = 0.07959$ when the line of centers is parallel to gravity. For spheres of diameter $d = 0.2$ and inter-particle distance $l_c = 0.3$ in a meso-scale cube of edge unity, we calculate that $\mathcal{U}_{h,hor} = 0.03956 < \mathcal{U}_{HP,hor}$ and $\mathcal{U}_{h,ver} = 0.05063 < \mathcal{U}_{HP,ver}$. Again, in the limit of zero concentration ($c \to 0$), the results should be identical.

There are some interesting qualitative remarks about the fall of two spheres in a periodic cell. First, the translational velocity vectors of the two particles are parallel. In other words, the inter-particle distance l_c remains constant throughout their fall. This can be explained through the concept of kinematic reversibility of Stokes flows ([47], [37] p. 641). In such flows, by reversing the fluid and the boundary motions as well as the pressure gradient and body forces, we are presented with a new flow that still satisfies the equations of motion. For the case of two spheres with their line of centers parallel to gravity it is intuitive, due to symmetry, that they have to fall parallel to gravity. However, it is not as clear that they should not catch up with each other (or separate from each other). In fact, if the top sphere caught up with the bottom one, by reversing the flow (which is equivalent to reversing gravity) the spheres diverge. This is impossible since there is no geometric up or down in this flow: rotating the gravity vector by π should yield the same flow. In other words, we cannot obtain qualitatively different motions by reversing the flow in such a symmetric geometry. Thus the spheres must fall and keep their distance constant. The same argument can be made for a pair of spheres oriented in any way. These results are consistent with the analytical results of Happel & Brenner discussed earlier. Note that some experiments show that the spheres actually change their center to center distance [26], however, this is probably an indication of the presence of inertia in the flow. For example, Feng, Hu & Joseph show phenomena such as "kissing and

tumbling" in their dynamical simulations which are for non-zero Reynolds numbers [16].

A second interesting fact is that a pair of spheres counter-rotate as they fall (unless they are aligned with gravity). Due to the symmetry of the problem they could not rotate in the same sense. Moreover, the sense of counter-rotation is consistent with the fact that fluid tends to flow around the two spheres (as if they were a single body). A third phenomenon is that a pair of particles in the meso-cell falls faster than one of the particles in the meso-cell, which is qualitatively similar to the behavior of particles in an unbounded fluid. Moreover, if the motion of the pair is compared to that of two spheres in an unbounded fluid as we did earlier, the hindering phenomenon is observed: the latter pair falls faster than the former.

Some comments can be made on the bounds presented in the previous section. For instance, the lower bound is sharper than the upper bound. This is probably because in the original flow, the spheres are close enough that there is little fluid motion between them. So blocking the flow (creating a dumbbell) does not affect the flow substantially. This argument also explains why the bound is sharper for the case of the line of centers being aligned with gravity. Intuitively, the nip region should be one of very low viscous dissipation for this orientation. Of course, as the particles get closer together, the lower bound gets sharper. Note that when analyzing a meso-cell with many inclusions, the nip region between two close neighbors can still be a region of relatively high viscous dissipation if, due to the particle distribution, fluid flow is "forced" to flow through the nip region. Clearly in this case the lower bound will not be as sharp.

Lastly, we experiment with three spheres in a meso-scale cube. In fact, this is the minimum number of spheres needed to observe relative motion of the inclusions. Figure 5-6a shows the surface mesh of the geometry we analyze which consists of three spheres on the $y_3 = 0.5$ plane. Two lie on a $y_2 = constant$ plane 0.4 units apart, and the third is positioned halfway between them but at a lower y_2 location (0.10 units below). Spheres 1 and 3 fall down and towards each others while counter-rotating. Sphere 2 falls straight down at a higher settling speed than the other two (see table

5.8). Table 5.9 shows the motion of the up-down symmetric flow, where the lower sphere is placed above the other two (figure 5-6b). This is equivalent to switching the sign of the gravity vector and the e_2 unit vector in figure 5-6a. Due to kinematic reversibility of the flow, the former action reverses the flow described in table 5.8 (i.e. all the velocity components switch signs). The latter action switches the signs of u_2 only so that we have the situation of figure 5-6b. Indeed, by performing the described transformations on the flow of table 5.8 we obtain the flow of table 5.9. It is important that our sedimentation formulation allows for relative motion of the inclusions, since this is an essential feature of real sedimenting suspensions.

5.3 Conclusions

This thesis has presented a procedure to analyze three-dimensional porous media and sedimentation inertia-free flows. The methodology relies on a variational scale-decomposition procedure and subsequent finite element solution of the meso-scale problem. Furthermore, we show how to efficiently treat geometrically stiff meso-scale problems by introducing nip-region modifications that can be proven to have variational bounding properties. Although our methodology is applicable to a random inclusion distributions of any concentration, we focus on simple periodic geometries to validate our procedure and show some interesting aspects of low-Reynolds-number flows.

Our porous media analysis is validated by reproducing well known results for simple cubic arrays of spheres. Moreover, we implement the micro-scale bounding procedures for a packed bed of spheres which allows us to make some comments about the minimum fluidization velocity.

The porous media results are used to validate the sedimentation formulation for simple cubic arrays. In order to observe more interesting behavior, we include two spheres in the meso-scale analysis. This allows us to check our results against well known Stokes flow properties such as kinematic reversibility, and to implement the micro-scale bounds. Finally, we observe relative motion between the particles when

we include three particles in the meso-scale cell.

In conclusion, we have validated our analytico-numerical approaches to porous media and sedimentation flows. However, there is still much to accomplish, as discussed in the next section.

5.4 Future Work

What follows are several suggestions regarding future work in porous media and sedimentation flows:

- Investigate random inclusion distributions. In order to do this we need to incorporate statistical analysis as discussed in Section 2.1, and alter the mesh generation procedure to allow spheres to intersect the meso-scale cube boundary. From a computational point of view, including many particles, possibly up to 100, creates serious memory and CPU speed requirements. This multi-particle problem lends itself to parallel processing as described by Cruz, Ghaddar & Patera [7].

- Include inertia (at intermediate Reynolds numbers).

- For sedimentation: explicitly track the particle trajectories in time, and determine a time averaged steady-state settling speed. Note that we can extend our current methodology by explicitly updating the position of the particles at each time step based on the quasi-static velocity field of the previous time step. We can therefore *determine* the particle JPDF.

- Study polydisperse and non-spherical inclusions.

- Extend the sedimentation methodology to fluidized beds of spherical particles at low to intermediate Reynolds numbers.

concentration	$\kappa_{zick-homsy}$	κ_h^P
0.008	4.554	4.507
0.064	0.3089	0.3080
0.125	0.1036	0.1031
0.216	0.03456	0.03455
0.343	0.01052	0.01047
0.45	0.004394	0.004374

Table 5.1: Permeability versus concentration results for simple cubic array of spheres.

nip diameter	$\kappa_{h,LB}^P$	$\kappa_{zick-homsy}$	$\kappa_{h,UB}^P$
0.2	0.002459	0.002520	0.002588
0.25	0.002250	0.002520	0.002862

Table 5.2: Permeability bounds for maximum packing density.

concentration	$\kappa_{zick-homsy}$	κ_h^P	κ_h^S
0.008	4.554	4.507	4.468
0.064	0.3089	0.3080	0.3068
0.125	0.1036	0.1031	0.1028
0.216	0.03456	0.03455	0.03432
0.343	0.01052	0.01047	0.01046
0.45	0.004394	0.004374	0.004368

Table 5.3: Permeability versus concentration results for simple cubic array of spheres: sedimentation results.

CASE	k	$(U_1)_k$	$(U_2)_k$	$(U_3)_k$	$(W_1)_k$	$(W_2)_k$	$(W_3)_k$
1	1	–	-0.050322	–	–	–	-0.007421
1	2	–	-0.050324	–	–	–	0.007412
2	1	–	-0.059150	–	–	–	–
2	2	–	-0.059184	–	–	–	–
3	1	-0.003920	-0.054733	–	–	–	-0.005346
3	2	-0.003917	-0.054708	–	–	–	0.005288

Table 5.4: Two spheres falling in a periodic box: translational and rotational degrees-of-freedom.

CASE	(U_1)	(U_2)	(U_3)	(W_1)	(W_2)	(W_3)
1	–	-0.047004	–	–	–	–
2	–	-0.058298	–	–	–	–
3	-0.005217	-0.052605	–	–	–	–

Table 5.5: Two spheres falling in a periodic box: lower bound.

CASE	k	$(U_1)_k$	$(U_2)_k$	$(U_3)_k$	$(W_1)_k$	$(W_2)_k$	$(W_3)_k$
1	1	–	-0.050980	–	–	–	-0.004649
1	2	–	-0.050981	–	–	–	0.004752
2	1	–	-0.058560	–	–	–	–
2	2	–	-0.05865	–	–	–	–
3	1	-0.003441	-0.054772	–	–	–	-0.003367
3	2	-0.003456	-0.054749	–	–	–	0.003316

Table 5.6: Two spheres falling in a periodic box: upper bound geometry.

CASE	$\mathcal{U}_{h,LB}$	$\mathcal{U}_h$	$\mathcal{U}_{h,UB}$
1	0.04700	0.05032	0.06372
2	0.05830	0.05916	0.07328
3	0.05261	0.05472	0.06845

Table 5.7: Two spheres falling in a periodic box: bound results

k	$(U_1)_k$	$(U_2)_k$	$(U_3)_k$	$(W_1)_k$	$(W_2)_k$	$(W_3)_k$
1	0.002954	-0.04860	–	–	–	-0.006537
2	–	-0.05423	–	–	–	–
3	-0.002953	-0.04866	–	–	–	0.006348

Table 5.8: Three spheres falling in a periodic box.

k	$(U_1)_k$	$(U_2)_k$	$(U_3)_k$	$(W_1)_k$	$(W_2)_k$	$(W_3)_k$
1	-0.002961	-0.04859	–	–	–	-0.006545
2	–	-0.05423	–	–	–	–
3	0.002943	-0.04865	–	–	–	0.006352

Table 5.9: Three spheres falling in a periodic box: reversed motion.

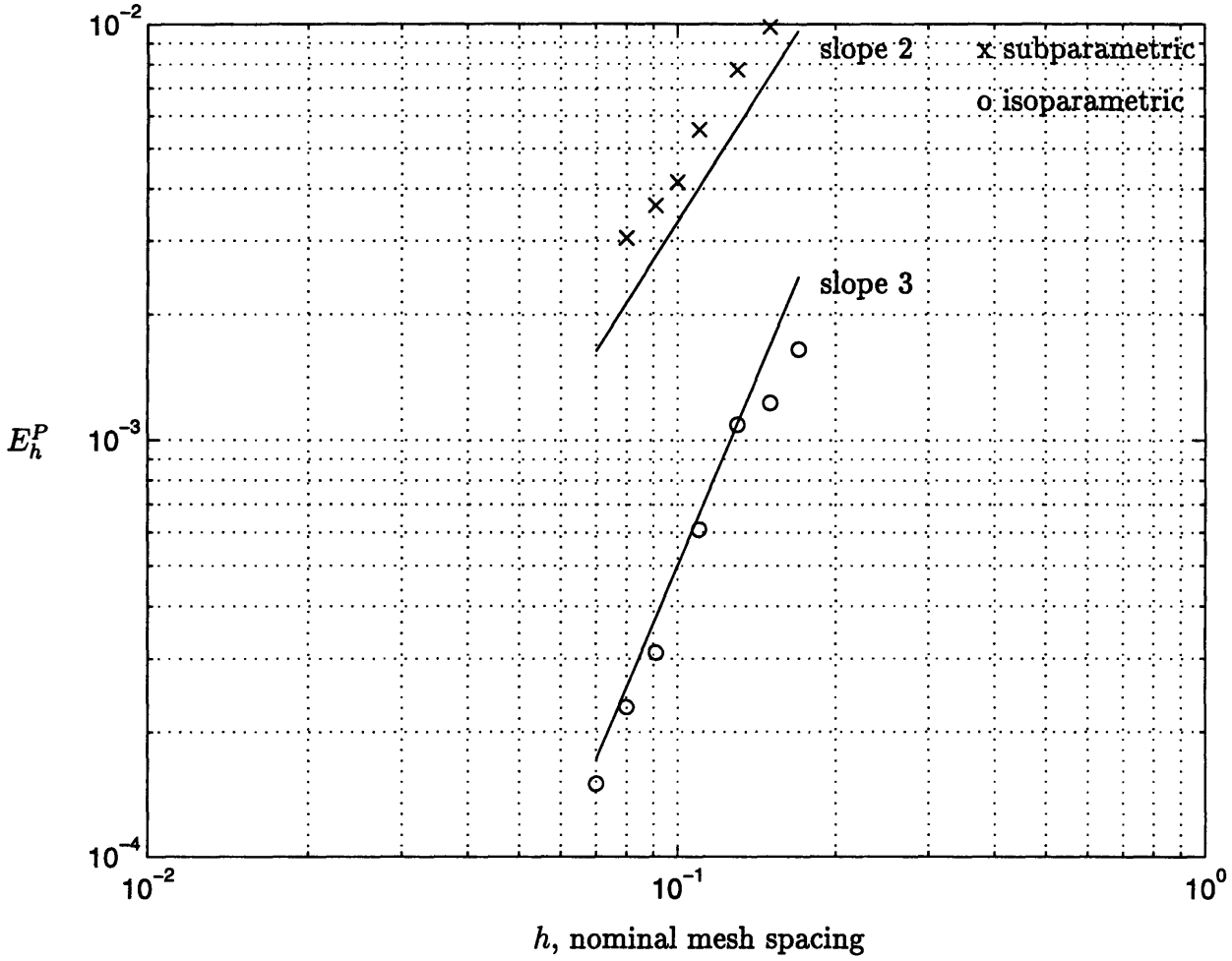

Figure 5-1: Convergence plot for the permeability code: E_h^P versus h for simple cubic array ($c = 0.125$).

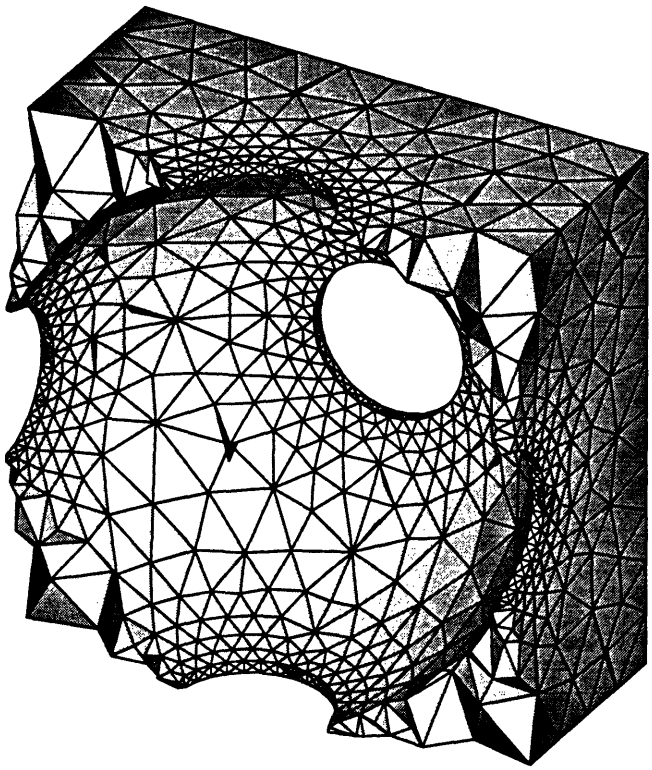

Figure 5-2: Permeability lower bound for maximum packing density (mesh cross-section).

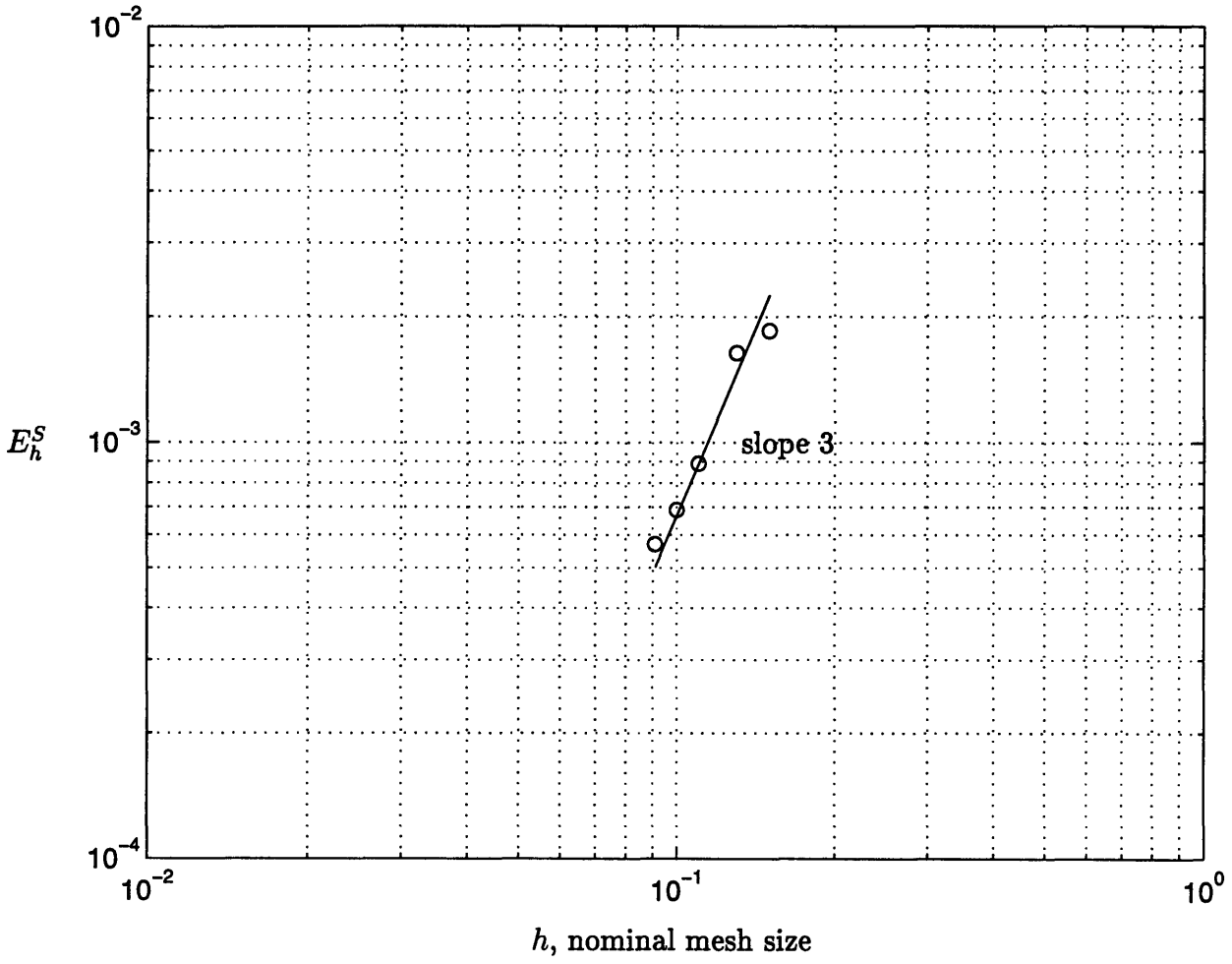

Figure 5-3: Convergence plot for the sedimentation code: E_h^S versus h for simple cubic array ($c = 0.125$).

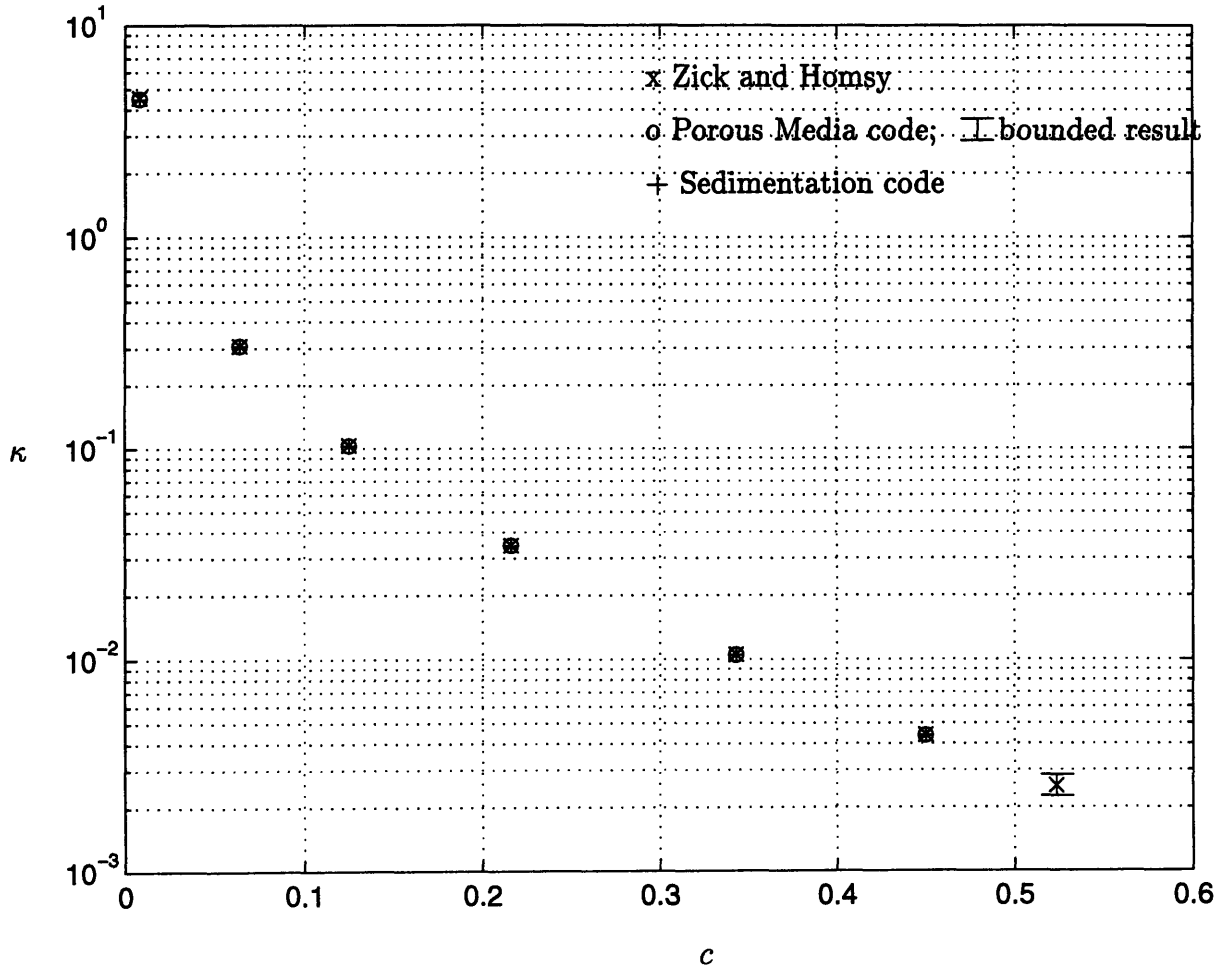

Figure 5-4: Permeability κ versus concentration c for simple cubic array.

a) CASE 1

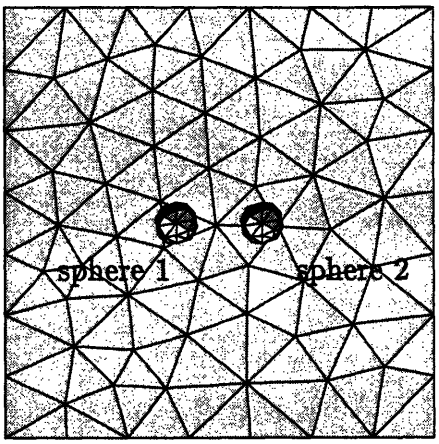

b) CASE 2

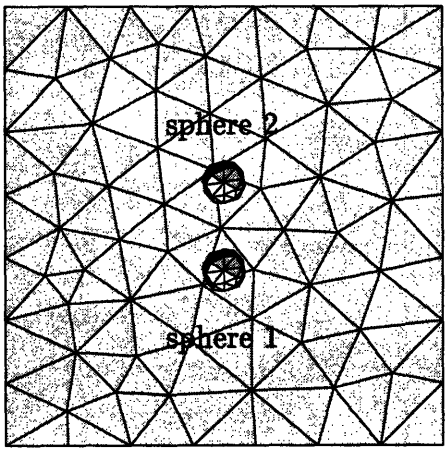

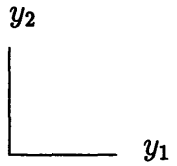

c) CASE 3

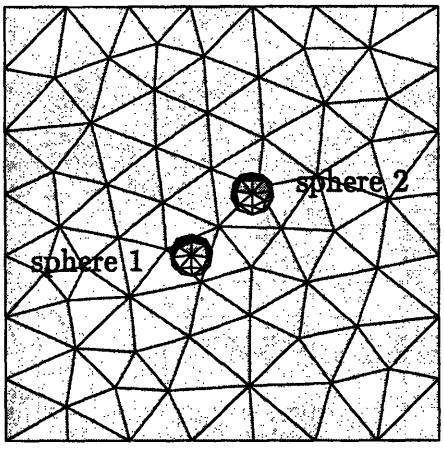

Figure 5-5: Sedimentation of two spheres in a meso-cell: surface meshes of the spheres and a face of the meso-cell.

a) CASE 1

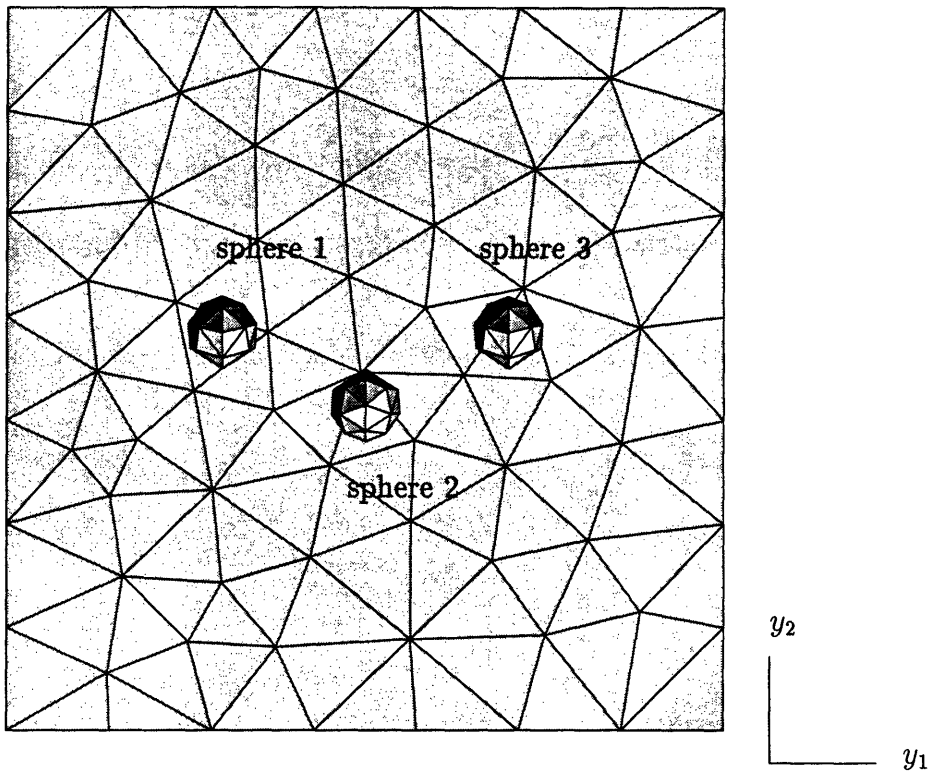

b) CASE 2

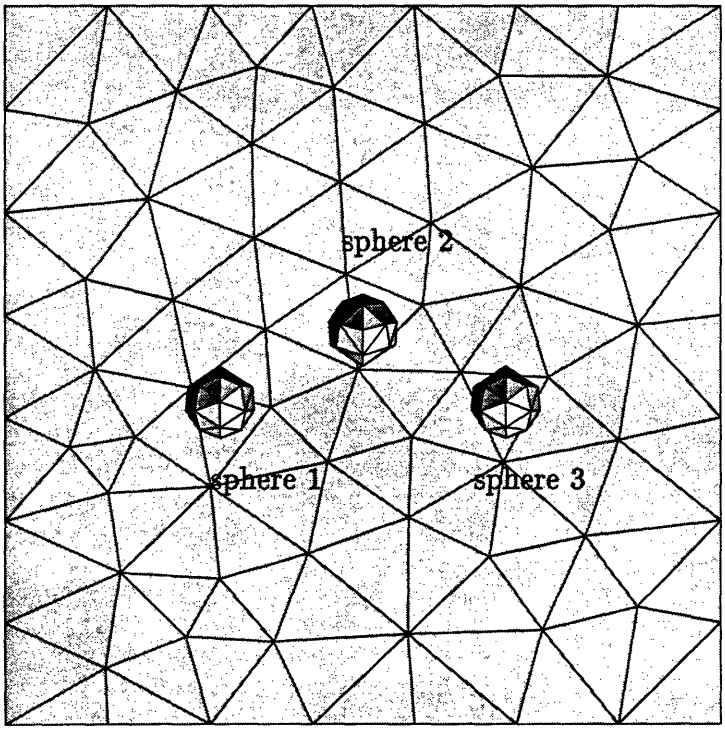

Figure 5-6: Sedimentation of three spheres in a meso-cell: surface meshes of the spheres and a face of the meso-cell.

Appendix A

Derivation of Equations from Chapter 2

A.1 Derivation of (2.39)

We start by multiplying (2.28) by $\mathbf{u}$ and integrating over Ω_{me} to obtain

$$-\int_{\Omega_{me}} u_i \frac{\partial}{\partial y_j}\left(\mu_{co}\left[\frac{\partial u_i}{\partial y_j}+\frac{\partial u_j}{\partial y_i}\right]\right)d\mathbf{y}+\int_{\Omega_{me}} u_i\frac{\partial p'}{\partial y_i}d\mathbf{y}-\int_{\Omega_{me}}\tau u_i\delta_{2i}d\mathbf{y} \;=\; 0\,. \quad \text{(A.1)}$$

By using the vector form of Green's theorem (the equivalent of integration by parts) [23]; rewriting $u_i\frac{\partial p'}{\partial y_i}=\frac{\partial}{\partial y_i}(p'u_i)-p'\frac{\partial u_i}{\partial y_i}$; and using the divergence theorem, we get

$$-\int_{\partial\Omega_{me}} u_i\left(\mu_{co}\left[\frac{\partial u_i}{\partial y_j}+\frac{\partial u_j}{\partial y_i}\right]\right)n_j dS+\int_{\Omega_{me}}\frac{\partial u_i}{\partial y_j}\left(\mu_{co}\left[\frac{\partial u_i}{\partial y_j}+\frac{\partial u_j}{\partial y_i}\right]\right)dV+$$
$$\int_{\partial\Omega_{me}} p'u_i n_i dS-\int_{\Omega_{me}} p'\frac{\partial u_i}{\partial y_i}dV-\int_{\Omega_{me}}\tau u_2 dV \;=\; 0\,, \quad \text{(A.2)}$$

where dV denotes an infinitesimal volume element in the fluid region, and dS is an infinitesimal surface element on a sphere. Now we use the fact that (2.33) applies to the velocity field in the surface integrals; we use incompressibility (2.29); the fact

that $\mathbf{a}\cdot(\mathbf{b}\times\mathbf{c})=(\mathbf{a}\times\mathbf{b})\cdot\mathbf{c}$ for vectors; and the fact that $\left(\frac{\partial u_i}{\partial y_j}+\frac{\partial u_j}{\partial y_i}\right)\left(\frac{\partial u_i}{\partial y_j}+\frac{\partial u_j}{\partial y_i}\right)=2\frac{\partial u_i}{\partial y_j}\left(\frac{\partial u_i}{\partial y_j}+\frac{\partial u_j}{\partial y_i}\right)$ to get

$$\int_{\Omega_{me}}\frac{1}{2}\mu_{co}\left(\frac{\partial u_i}{\partial y_j}+\frac{\partial u_j}{\partial y_i}\right)\left(\frac{\partial u_i}{\partial y_j}+\frac{\partial u_j}{\partial y_i}\right)dV-\tau\int_{\Omega_{me}}u_2dV\;=$$
$$\sum_{k=1}^{N}(U_i)_k\int_{\partial\Omega_k}\left[-p'\delta_{ij}+\mu_{co}\left(\frac{\partial u_i}{\partial y_j}+\frac{\partial u_j}{\partial y_i}\right)\right]n_jdS+$$
$$\sum_{k=1}^{N}\mathbf{W}_k\cdot\int_{\partial\Omega_k}(\mathbf{y}-\mathbf{y}_k)\times[-p'\mathbf{n}+\mathbf{S}:\mathbf{n}]\,dS\,, \tag{A.3}$$

where $\mathbf{S}=\mu_{co}\left(\frac{\partial u_i}{\partial y_j}+\frac{\partial u_j}{\partial y_i}\right)$; and we have mixed tensor and vector notations to avoid complicated indicial notation due to the vector product. Note that the integrals over the meso-scale cube boundaries cancel out by periodicity. Observing that $-p'\mathbf{n}+\mathbf{S}:\mathbf{n}=\mathbf{T}':\mathbf{n}$ we can rewrite (A.3) as

$$\int_{\Omega_{me}}\frac{1}{2}\mu_{co}\left(\frac{\partial u_i}{\partial y_j}+\frac{\partial u_j}{\partial y_i}\right)\left(\frac{\partial u_i}{\partial y_j}+\frac{\partial u_j}{\partial y_i}\right)dV-\tau\int_{\Omega_{me}}u_2dV\;=$$
$$\sum_{k=1}^{N}(U_i)_k\int_{\partial\Omega_k}\mathbf{T}':\mathbf{n}dS+\sum_{k=1}^{N}\mathbf{W}_k\cdot\int_{\partial\Omega_k}(\mathbf{y}-\mathbf{y}_k)\times(\mathbf{T}':\mathbf{n})dS\,. \tag{A.4}$$

Using conditions (2.30), (2.34) and (2.35) we get

$$\int_{\Omega_{me}}\frac{1}{2}\mu_{co}\left(\frac{\partial u_i}{\partial y_j}+\frac{\partial u_j}{\partial y_i}\right)\left(\frac{\partial u_i}{\partial y_j}+\frac{\partial u_j}{\partial y_i}\right)dV\;=\;-\mathcal{W}\sum_{k=1}^{N}(U_2)_k\,, \tag{A.5}$$

which, in view of (2.38), shows that

$$J^S_{\Omega_{me}}(\mathbf{u})=I^S_{\Omega_{me}}(\mathbf{u})=\int_{\Omega_{me}}\frac{1}{2}\mu_{co}\left(\frac{\partial u_i}{\partial y_j}+\frac{\partial u_j}{\partial y_i}\right)\left(\frac{\partial u_i}{\partial y_j}+\frac{\partial u_j}{\partial y_i}\right)dV\,. \tag{A.6}$$

which proves (2.39).

A.2 Derivation of (2.40)

In order to arrive at (2.40), we multiply (2.28) by the test function $\mathbf{v} \in B$, and integrate over Ω_{me}. We have

$$-\int_{\Omega_{me}} v_i \frac{\partial}{\partial y_j}\left(\mu_{co}\left[\frac{\partial u_i}{\partial y_j}+\frac{\partial u_j}{\partial y_i}\right]\right) d\mathbf{y} + \int_{\Omega_{me}} v_i \frac{\partial p'}{\partial y_i} d\mathbf{y} - \int_{\Omega_{me}} \tau v_i \delta_{2i} d\mathbf{y} \;=\; 0\,. \quad \text{(A.7)}$$

As in the previous section, we integrate by parts according to Green's theorem and use the divergence theorem to obtain

$$-\int_{\partial\Omega_{me}} v_i\left(\mu_{co}\left[\frac{\partial u_i}{\partial y_j}+\frac{\partial u_j}{\partial y_i}\right]\right) n_j dS + \int_{\Omega_{me}} \frac{\partial v_i}{\partial y_j}\left(\mu_{co}\left[\frac{\partial u_i}{\partial y_j}+\frac{\partial u_j}{\partial y_i}\right]\right) dV + \int_{\partial\Omega_{me}} p' v_i n_i dS - \int_{\Omega_{me}} p' \frac{\partial v_i}{\partial y_i} dV - \int_{\Omega_{me}} \tau v_2 dV \;=\; 0\,. \quad \text{(A.8)}$$

We require that $\frac{\partial v_i}{\partial y_i} = 0$. In addition, the test function $\mathbf{v}$ has to be consistent with solid body motion of the spheres according to the no-slip kinematic condition of (2.41). Rearranging terms, (A.8) becomes

$$\int_{\Omega_{me}} \frac{\partial v_i}{\partial y_j}\left(\mu_{co}\left[\frac{\partial u_i}{\partial y_j}+\frac{\partial u_j}{\partial y_i}\right]\right) dV - \tau\int_{\Omega_{me}} v_2 dV \;=\; -\sum_{k=1}^{N}\int_{\partial\Omega_k} p'(V_i)_k n_i dS - \sum_{k=1}^{N}\int_{\partial\Omega_k} p'\left(\mathbf{Z}_k \times (\mathbf{y}-\mathbf{y}_k)\right)_i n_i dS + \sum_{k=1}^{N}\int_{\partial\Omega_k} (V_i)_k\left(\mu_{co}\left[\frac{\partial u_i}{\partial y_j}+\frac{\partial u_j}{\partial y_i}\right]\right) n_j dS + \sum_{k=1}^{N}\int_{\partial\Omega_k} \left(\mathbf{Z}_k \times (\mathbf{y}-\mathbf{y}_k)\right)_i \left(\mu_{co}\left[\frac{\partial u_i}{\partial y_j}+\frac{\partial u_j}{\partial y_i}\right]\right) n_j dS\,. \quad \text{(A.9)}$$

Using the fact that $\left(\frac{\partial v_i}{\partial y_j}+\frac{\partial v_j}{\partial y_i}\right)\left(\frac{\partial u_i}{\partial y_j}+\frac{\partial u_j}{\partial y_i}\right) = 2\frac{\partial v_i}{\partial y_j}\left(\frac{\partial u_i}{\partial y_j}+\frac{\partial u_j}{\partial y_i}\right)$; and the fact that $\mathbf{V}_k$ and $\mathbf{Z}_k$ do not vary over $\partial\Omega_k$ we have

$$\int_{\Omega_{me}} \frac{1}{2}\mu_{co}\left(\frac{\partial v_i}{\partial y_j}+\frac{\partial v_j}{\partial y_i}\right)\left(\frac{\partial u_i}{\partial y_j}+\frac{\partial u_j}{\partial y_i}\right) dV - \tau\int_{\Omega_{me}} v_2 dV \;=$$

$$\sum_{k=1}^{N}(V_i)_k \int_{\partial\Omega_k}\left[-p'\delta_{ij}+\mu_{co}\left(\frac{\partial u_i}{\partial y_j}+\frac{\partial u_j}{\partial y_i}\right)\right]n_j dS + \sum_{k=1}^{N}\mathbf{Z}_k\cdot\int_{\partial\Omega_k}(\mathbf{y}-\mathbf{y}_k)\times[-p'\mathbf{n}+\mathbf{S}:\mathbf{n}]\,dS\,, \tag{A.10}$$

where we have again mixed indicial and vector notations and used $\mathbf{a}\cdot(\mathbf{b}\times\mathbf{c})=(\mathbf{a}\times\mathbf{b})\cdot\mathbf{c}$ for vectors. Recognizing that $-p'\mathbf{n}+\mathbf{S}:\mathbf{n}=\mathbf{T}':\mathbf{n}$ we rewrite (A.10) as

$$\int_{\Omega_{me}}\frac{1}{2}\mu_{co}\left(\frac{\partial v_i}{\partial y_j}+\frac{\partial v_j}{\partial y_i}\right)\left(\frac{\partial u_i}{\partial y_j}+\frac{\partial u_j}{\partial y_i}\right)dV-\tau\int_{\Omega_{me}}v_2 dV = \sum_{k=1}^{N}(V_i)_k\int_{\partial\Omega_k}\mathbf{T}':\mathbf{n}dS+\sum_{k=1}^{N}\mathbf{Z}_k\cdot\int_{\partial\Omega_k}(\mathbf{y}-\mathbf{y}_k)\times(\mathbf{T}':\mathbf{n})dS\,. \tag{A.11}$$

We now require that $\int_{\Omega_{me}}v_2 dV=-\frac{\pi d^3}{6}\sum_{k=1}^{N}(V_2)_k$ and use conditions (2.34) and (2.35) to arrive at

$$\int_{\Omega_{me}}\frac{1}{2}\mu_{co}\left(\frac{\partial v_i}{\partial y_j}+\frac{\partial v_j}{\partial y_i}\right)\left(\frac{\partial u_i}{\partial y_j}+\frac{\partial u_j}{\partial y_i}\right)dV \;=\; -\mathcal{W}\sum_{k=1}^{N}(V_2)_k \quad \forall\mathbf{v}\in B\,. \tag{A.12}$$

If we multiply both sides of the equation by 2, and identify $\mathbf{v}=\delta\mathbf{u}$ (which is the variation of $\mathbf{u}$), we recognize that (A.12) is the first variation of the functional $J^S_{\Omega_{me}}$ set equal to zero.

In fact, let us take the first variation of $J^S_{\Omega_{me}}$:

$$J^S_{\Omega_{me}}(\mathbf{w}+\mathbf{v}) \;=\; -\int_{\Omega_{me}}\tfrac{1}{2}\mu_{co}\left(\tfrac{\partial v_i}{\partial y_j}+\tfrac{\partial w_i}{\partial y_j}+\tfrac{\partial v_j}{\partial y_i}+\tfrac{\partial w_j}{\partial y_i}\right)\left(\tfrac{\partial v_i}{\partial y_j}+\tfrac{\partial w_i}{\partial y_j}+\tfrac{\partial v_j}{\partial y_i}+\tfrac{\partial w_j}{\partial y_i}\right)dV - 2\mathcal{W}\textstyle\sum_{k=1}^{N}(V_2+V_2')_k\,, \tag{A.13}$$

where $(\mathbf{w},\mathbf{v})\in B^2$; and $\mathbf{w}|_{\partial\Omega_k}=\mathbf{V}'_k+\mathbf{Z}'_k\times(\mathbf{y}-\mathbf{y}_k)$. Rearranging (A.13),

$$J^S_{\Omega_{me}}(\mathbf{w}+\mathbf{v}) \;=\; -\int_{\Omega_{me}}\frac{1}{2}\mu_{co}\left(\frac{\partial w_i}{\partial y_j}+\frac{\partial w_j}{\partial y_i}\right)\left(\frac{\partial w_i}{\partial y_j}+\frac{\partial w_j}{\partial y_i}\right)dV-2\mathcal{W}\sum_{k=1}^{N}(V_2')_k$$

$$- \int_{\Omega_{me}} \mu_{co} \left(\frac{\partial v_i}{\partial y_j} + \frac{\partial v_j}{\partial y_i} \right) \left(\frac{\partial w_i}{\partial y_j} + \frac{\partial w_j}{\partial y_i} \right) dV - 2\mathcal{W} \sum_{k=1}^{N} (V_2)_k$$
$$- \int_{\Omega_{me}} \frac{1}{2} \mu_{co} \left(\frac{\partial v_i}{\partial y_j} + \frac{\partial v_j}{\partial y_i} \right) \left(\frac{\partial v_i}{\partial y_j} + \frac{\partial v_j}{\partial y_i} \right) dV \,, \quad \text{(A.14)}$$

where the terms on the second line represent the first variation of $J^S_{\Omega_{me}}$ and the last term is the second variation. Note that the second variation is always negative. It follow from (A.14) that

$$J^S_{\Omega_{me}}(\mathbf{u} + \delta\mathbf{u}) \;=\; J^S_{\Omega_{me}}(\mathbf{u}) + \delta J^S_{\Omega_{me}}(\mathbf{u}) + \delta^2 J^S_{\Omega_{me}}(\mathbf{u}) \,, \qquad \text{(A.15)}$$

where δJ^S and $\delta^2 J^S$ are the first and second variations of J^S respectively. Since $\delta^2 J^S_{\Omega_{me}}(\mathbf{u}) < 0$, and $\delta J^S_{\Omega_{me}}(\mathbf{u}) = 0$ from (A.12), we get

$$J^S_{\Omega_{me}}(\mathbf{u} + \delta\mathbf{u}) \;=\; J^S_{\Omega_{me}}(\mathbf{u}) + \delta^2 J^S_{\Omega_{me}}(\mathbf{u}) < J^S_{\Omega_{me}}(\mathbf{u}) \quad \forall \delta\mathbf{u} \in B,\ \delta\mathbf{u} \neq 0 \,, \qquad \text{(A.16)}$$

which proves that $\mathbf{u}$ is the argument that maximizes $J^S_{\Omega_{me}}(\mathbf{v})$ for all $\mathbf{v} \in B$, as claimed in (2.40).

A.3 Equivalence of Strong Form (2.28)-(2.35) and Variational Weak Form (2.44)-(2.46)

Equations (2.44) - (2.46) can also be obtained from the strong form equations. In fact, (2.45) is obtained by multiplying (2.29) by $q \in L^2_{\#,0}$ and integrating over Ω_{me}; and (2.46) comes from multiplying (2.30) by $\eta \in \mathcal{R}$. To arrive at (2.44) we multiply (2.28) by $\mathbf{v} \in Y$ and integrate over Ω_{me}. Integrating by parts and using the divergence theorem we arrive at (A.8). Then we use the no-slip boundary condition (2.33) to get

$$\int_{\Omega_{me}} \frac{\partial v_i}{\partial y_j} \left(\mu_{co} \left[\frac{\partial u_i}{\partial y_j} + \frac{\partial u_j}{\partial y_i} \right] \right) dV - \int_{\Omega_{me}} p' \frac{\partial v_i}{\partial y_i} dV - \int_{\Omega_{me}} \tau v_2 dV$$

$$-\sum_{k=1}^{N} \mathbf{V}_k \cdot \int_{\partial\Omega_k} \mathbf{T}' : \mathbf{n} dS - \sum_{k=1}^{N} \mathbf{Z}_k \cdot \int_{\partial\Omega_k} (\mathbf{y} - \mathbf{y}_k) \times (\mathbf{T}' : \mathbf{n}) dS \;=\; 0\,. \qquad \text{(A.17)}$$

The last integral vanishes due to the torque balance condition (2.35). Finally, by using the force balance condition (2.34) and rearranging terms we obtain (2.44), which reads

$$\begin{aligned} \mu_{co} \int_{\Omega_{me}} \frac{\partial v_i}{\partial y_j} \left(\frac{\partial u_i}{\partial y_j} + \frac{\partial u_j}{\partial y_i} \right) d\mathbf{y} \;\; - \;\; & \int_{\Omega_{me}} p' \frac{\partial v_i}{\partial y_i} d\mathbf{y} - \tau \left[\int_{\Omega_{me}} v_2 \, d\mathbf{y} - \frac{\pi d^3}{6\mathcal{W}} I^S(\mathbf{v}) \right] \\ = \;\; & I^S(\mathbf{v}) \quad \forall \mathbf{v} \in Y\,. \end{aligned} \qquad \text{(A.18)}$$

We conclude by noting that the stress boundary conditions (2.34) and (2.35) are *natural* boundary conditions in this formulation. This can be seen by integrating (A.18) by parts and noticing that satisfying the new equation for any variation $\mathbf{v} \in Y$ implies that the stress boundary conditions (2.34) and (2.35) are automatically satisfied.

Appendix B

Affine Mapping; Gaussian Quadrature; and Master-Slave Mapping

B.1 Affine Mapping Matrices

In equation (4.13), the following affine mapping is presented

$$\zeta_\alpha \;=\; C_\alpha^{k_e} \;+\; \sum_{\beta=1}^{3} D_{\alpha\beta}^{k_e}\, y_\beta \,. \tag{B.1}$$

The vector $C_\alpha^{k_e}$ is defined as

$$\begin{aligned} C_\alpha^{k_e} \;=\; \Big[y_{1_{[\alpha+3]}} \left(y_{2_{[\alpha+1]}} y_{3_{[\alpha+2]}} - y_{2_{[\alpha+2]}} y_{3_{[\alpha+1]}} \right) - y_{2_{[\alpha+3]}} \left(y_{1_{[\alpha+1]}} y_{3_{[\alpha+2]}} - y_{1_{[\alpha+2]}} y_{3_{[\alpha+1]}} \right) \\ + y_{3_{[\alpha+3]}} \left(y_{1_{[\alpha+1]}} y_{2_{[\alpha+2]}} - y_{1_{[\alpha+2]}} y_{2_{[\alpha+1]}} \right) \Big] / (6\, vol^{k_e}) \,, \end{aligned} \tag{B.2}$$

and

$$D_{\alpha 1}^{k_e} \;=\; \Big[y_{2_{[\alpha+3]}} \left(y_{3_{[\alpha+2]}} - y_{3_{[\alpha+1]}} \right) - y_{3_{[\alpha+3]}} \left(y_{2_{[\alpha+2]}} - y_{2_{[\alpha+1]}} \right) \tag{B.3}$$

$$-y_{2_{[\alpha+1]}}y_{3_{[\alpha+2]}} + y_{2_{[\alpha+2]}}y_{3_{[\alpha+1]}}\Big] /(6\, vol^{k_e}) \,,$$

$$D^{k_e}_{\alpha 2} = \Big[-y_{1_{[\alpha+3]}}\left(y_{3_{[\alpha+2]}} - y_{3_{[\alpha+1]}}\right) + y_{3_{[\alpha+3]}}\left(y_{1_{[\alpha+2]}} - y_{1_{[\alpha+1]}}\right) \tag{B.4}$$
$$+y_{1_{[\alpha+1]}}y_{3_{[\alpha+2]}} - y_{1_{[\alpha+2]}}y_{3_{[\alpha+1]}}\Big] /(6\, vol^{k_e}) \,,$$

$$D^{k_e}_{\alpha 3} = \Big[y_{3_{[\alpha+3]}}\left(y_{2_{[\alpha+2]}} - y_{2_{[\alpha+1]}}\right) - y_{2_{[\alpha+3]}}\left(y_{1_{[\alpha+2]}} - y_{1_{[\alpha+1]}}\right) \tag{B.5}$$
$$+y_{1_{[\alpha+2]}}y_{2_{[\alpha+1]}} - y_{1_{[\alpha+1]}}y_{2_{[\alpha+2]}}\Big] /(6\, vol^{k_e}) \,,$$

where $y_{i_{[\alpha]}}$ is the coordinate of local node α in the i direction; and $[\alpha] = \alpha_{mod\,4}$.

B.2 Gaussian Quadrature Points and Weights

In (4.24) we give the Gaussian integration formula in terms of points $\breve{\zeta}_{\alpha j}$ and weights $\breve{w}_j$, $j = 1, .., np$. To integrate a fifth order polynomial over the domain $\hat{\Omega}$, we need the fifteen points and weights shown in table B.1 [46].

B.3 Master-Slave Mapping

In Section 4.3 we introduce the matrix $\underline{\mathbf{Q}}$ which maps the six degrees-of-freedom of a sphere onto the finite element nodes that are on the surface of the sphere. We want to write $\underline{v}_h = \underline{\mathbf{Q}}\underline{v}_h^{master}$ with local data structures. The local representation of $(v_h)_i$, $i = 1, .., N_{gn}$ is $(v_h)^{k_e}_\alpha$, $k_e = 1, .., \mathcal{K}$, $\alpha = 1, .., 30$ where the first 10 entries are for the y_1 components, the second decade is for the y_2 components, and the last decade is for the y_3 components. To represent $(v_h^{master})_i$, $i = 1, .., N_{dof}$ locally we choose to use two arrays: $(v_h^{master})^{k_e}_\alpha$ and $(v_h^{VW,master})^k_\gamma$. The first has the same structure of $(v_h)^{k_e}_\alpha$ but has a zero entry when $g^{k_e}_\alpha$ corresponds to a node on a sphere. The second array has the form $(v_h^{VW,master})^k_\gamma$ where $\gamma = 1, .., 6$ is for the six degrees-of-freedom of sphere

$k = 1, .., N$. In more detail, we have

$$
\begin{aligned}
(v_h^{VW,master})_1^k &= (V_1)_k \,, \\
(v_h^{VW,master})_2^k &= (V_2)_k \,, \\
(v_h^{VW,master})_3^k &= (V_3)_k \,, \\
(v_h^{VW,master})_4^k &= (W_1)_k \,, \\
(v_h^{VW,master})_5^k &= (W_2)_k \,, \\
(v_h^{VW,master})_6^k &= (W_3)_k \,.
\end{aligned}
\tag{B.6}
$$

The action of the matrix $\underline{\mathbf{Q}}$ is described by the following algorithm:

- set $(v_h)_\alpha^{k_e}$ to zero.
- loop $k_e = 1, .., \mathcal{K}$

  loop $\alpha = 1, .., 10$

  if node $g_\alpha^{k_e}$ is on sphere k then

$$
\begin{aligned}
(v_h)_\alpha^{k_e} &= (v_h^{VW,master})_1^k + (v_h^{VW,master})_5^k (y_{3(g_\alpha^{k_e})} - y_{3k}) \\
&\qquad - (v_h^{VW,master})_6^k (y_{2(g_\alpha^{k_e})} - y_{2k}). \\
(v_h)_{(\alpha+10)}^{k_e} &= (v_h^{VW,master})_2^k + (v_h^{VW,master})_6^k (y_{1(g_\alpha^{k_e})} - y_{1k}) \\
&\qquad - (v_h^{VW,master})_4^k (y_{3(g_\alpha^{k_e})} - y_{3k}). \\
(v_h)_{(\alpha+20)}^{k_e} &= (v_h^{VW,master})_3^k + (v_h^{VW,master})_4^k (y_{2(g_\alpha^{k_e})} - y_{2k}) \\
&\qquad - (v_h^{VW,master})_5^k (y_{1(g_\alpha^{k_e})} - y_{1k}).
\end{aligned}
$$

  else

$$
\begin{aligned}
(v_h)_\alpha^{k_e} &= (v_h^{master})_\alpha^{k_e}. \\
(v_h)_{(\alpha+10)}^{k_e} &= (v_h^{master})_{(\alpha+10)}^{k_e}. \\
(v_h)_{(\alpha+20)}^{k_e} &= (v_h^{master})_{(\alpha+20)}^{k_e}.
\end{aligned}
$$

The matrix $\underline{\mathbf{Q}}^T$ operates in the opposite direction: from slave to master degrees-of-freedom. The structure of $\underline{\mathbf{Q}}^T$ follows from that of $\underline{\mathbf{Q}}$. For instance, $\underline{\mathbf{Q}}$ transcribes the translational degree-of-freedom of a particle onto its surface nodes. Therefore, the

matrix $\underline{\mathbf{Q}}^T$ must add up all the slave nodal surface values and transcribe the result to the translational degree-of-freedom of the particle. The action of $\underline{\mathbf{Q}}^T$ is calculated according to the algorithm

- set $(v_h^{VW,master})_\gamma^k$ to zero.
- loop $k_e = 1, .., \mathcal{K}$

  loop $\alpha = 1, .., 10$

  if node $g_\alpha^{k_e}$ is on sphere k then

$$
\begin{aligned}
(v_h^{VW,master})_1^k &= (v_h^{VW,master})_1^k + (v_h)_\alpha^{k_e}/multi_{(g_\alpha^{k_e})}. \\
(v_h^{VW,master})_2^k &= (v_h^{VW,master})_2^k + (v_h)_{(\alpha+10)}^{k_e}/multi_{(g_\alpha^{k_e})}. \\
(v_h^{VW,master})_3^k &= (v_h^{VW,master})_3^k + (v_h)_{(\alpha+20)}^{k_e}/multi_{(g_\alpha^{k_e})}. \\
(v_h^{VW,master})_4^k &= (v_h^{VW,master})_4^k + ((v_h)_{(\alpha+20)}^{k_e}(y_{2_{(g_\alpha^{k_e})}} - y_{2k}) \\
&\qquad -(v_h)_{(\alpha+10)}^{k_e}(y_{3_{(g_\alpha^{k_e})}} - y_{3k}))/multi_{(g_\alpha^{k_e})}. \\
(v_h^{VW,master})_5^k &= (v_h^{VW,master})_5^k + ((v_h)_\alpha^{k_e}(y_{3_{(g_\alpha^{k_e})}} - y_{3k}) \\
&\qquad -(v_h)_{(\alpha+20)}^{k_e}(y_{1_{(g_\alpha^{k_e})}} - y_{1k}))/multi_{(g_\alpha^{k_e})}. \\
(v_h^{VW,master})_6^k &= (v_h^{VW,master})_6^k + ((v_h)_{(\alpha+10)}^{k_e}(y_{1_{(g_\alpha^{k_e})}} - y_{1k}) \\
&\qquad -(v_h)_\alpha^{k_e}(y_{2_{(g_\alpha^{k_e})}} - y_{2k}))/multi_{(g_\alpha^{k_e})}. \\
(v_h^{master})_\alpha^{k_e} &= 0. \\
(v_h^{master})_{(\alpha+10)}^{k_e} &= 0. \\
(v_h^{master})_{(\alpha+20)}^{k_e} &= 0.
\end{aligned}
$$

Note that $g_\alpha^{k_e} = g_{(\alpha_{mod10})}^{k_e}$.

j	$\breve{w}_j$	$\breve{\zeta}_{1j}$	$\breve{\zeta}_{2j}$	$\breve{\zeta}_{3j}$	$\breve{\zeta}_{4j}$
1	0.118518518519	0.25	0.25	0.25	0.25
2	0.0719370837790	r_1	r_1	r_1	s_1
3	0.0719370837790	r_1	r_1	s_1	r_1
4	0.0719370837790	r_1	s_1	r_1	r_1
5	0.0719370837790	s_1	r_1	r_1	r_1
6	0.0690682072263	r_2	r_2	r_2	s_2
7	0.0690682072263	r_2	r_2	s_2	r_2
8	0.0690682072263	r_2	s_2	r_2	r_2
9	0.0690682072263	s_2	r_2	r_2	r_2
10	0.05291005291	v_1	u_1	u_1	v_1
11	0.05291005291	u_1	v_1	u_1	v_1
12	0.05291005291	u_1	u_1	v_1	v_1
13	0.05291005291	v_1	v_1	u_1	u_1
14	0.05291005291	v_1	u_1	v_1	u_1
15	0.05291005291	u_1	v_1	v_1	u_1

Table B.1: Gaussian quadrature points: $r_1 = 0.091971078$, $s_1 = 0.724086765$, $r_2 = 0.319793627$, $s_2 = 0.040619116$, $v_1 = 0.056350832$, $u_1 = 0.443649167$

Appendix C

Heat Conduction in Composites

We use figure 2-3 from the viscous porous media problem to describe the heat conduction problem. The continuous matrix Ω_{co} consists of a solid material with heat conductivity k_{co}. The inclusions Ω_{di} are heat insulating spheres arranged in space according to a given JPDF. Heat flow is induced by a temperature gradient $\Delta T/L$ that extends over the macro-scale of characteristic length L. We want to determine the effective conductivity k of the material. Note that in this appendix we use k to represent the conductivity, not the sphere number as in the sedimentation formulation. Moreover, we only deal with isotropic media, for which the effective conductivity k is a scalar.

In the original medium, the temperature distribution $T(\mathbf{x})$ is determined by Laplace's equation in Ω_{co} with homogeneous Neumann (zero heat flux) boundary conditions at the sphere surfaces and wall ($\partial\Omega_{co} \cup \Gamma_w$) and Dirichlet boundary conditions on Γ_{in} and Γ_{out} such that $\Delta T = T_{in} - T_{out}$. Cruz & Patera [9], use homogenization theory to arrive at the meso-scale strong form. By expanding $T(\mathbf{x}) = T_{ma}(\mathbf{x}) + \epsilon\chi(\mathbf{x},\mathbf{y}) + O(\epsilon^2)$, where $\epsilon = \lambda/L$ we obtain

$$-\frac{\partial}{\partial y_i}(k_{co}\frac{\partial \chi}{\partial y_i}) = 0 \quad in\ \Omega_{me}\ , \tag{C.1}$$

with Neumann boundary condition

$$-k_{co}\frac{\partial \chi}{\partial y_i}n_i = -k_{co}\frac{\Delta T}{L}n_1 \quad on\ \partial\Omega_{me}\ . \tag{C.2}$$

In addition we require that χ be λ-triply periodic and that $\int_{\Omega_{me}} \chi d\mathbf{y} = 0$ for uniqueness. Physically, (C.2) states that the gradient in the perturbation temperature χ and the imposed macro-scale temperature gradient must balance on the adiabatic surface $\partial\Omega_{me}$.

The non-dimensional forms of (C.1), (C.2) are obtained by non-dimensionalizing the temperature with $\frac{\Delta T d}{L}$; the conductivity with k_{co}; and the linear dimensions with d. We rewrite (C.1), (C.2) as

$$-\frac{\partial^2 \chi}{\partial y_i \partial y_i} = 0 \quad in\ \Omega_{me}\ , \tag{C.3}$$

$$-\frac{\partial \chi}{\partial y_i}n_i = -n_1 \quad on\ \partial\Omega_{me}\ , \tag{C.4}$$

where the same symbols represent the new dimensionless quantities.

We now pursue the variational formulation of the problem. We introduce the functional $J^C_\Omega(w)$

$$J^C_\Omega(w) = \int_\Omega \frac{\partial w}{\partial y_m}\frac{\partial w}{\partial y_m}d\mathbf{y} - 2\int_\Omega \frac{\partial w}{\partial y_1}d\mathbf{y}\ . \tag{C.5}$$

It can be shown that

$$\chi = \arg \min_{w \in H^1_{\#,0}(\Omega_{me})} J^C_{\Omega_{me}}(w)\ , \tag{C.6}$$

where $H^1_{\#,0}(\Omega_{me})$ is the space of all square-integrable functions w that are λ-triply periodic; that have square-integrable first derivatives; and for which $\int_{\Omega_{me}} w d\mathbf{y} = 0$. By setting the first variation of (C.5) equal to zero, we obtain the variational weak form of the conduction problem. We have

$$\int_{\Omega_{me}} \frac{\partial v}{\partial y_m}\frac{\partial \chi}{\partial y_m}d\mathbf{y} = \int_{\Omega_{me}} \frac{\partial v}{\partial y_1}d\mathbf{y} \qquad \forall v \in H^1_{\#,0}(\Omega_{me})\ . \tag{C.7}$$

The variational weak form (C.7) is equivalent to the strong form (C.3), (C.4). Indeed,

by multiplying (C.3) by v; integrating by parts; and using (C.4) we obtain (C.7). Note that the non-homogeneous Neumann boundary condition (C.4) appears as a forcing term in the variational formulation of the problem.

The non-dimensional effective conductivity k is expressed as [9] [6]

$$k = (1-c) - \frac{1}{\lambda^3} \int_{\Omega_{me}} \frac{\partial \chi}{\partial y_1} d\mathbf{y} , \tag{C.8}$$

which from (C.5), (C.6) and (C.7), can be expressed as

$$k = (1-c) + \frac{1}{\lambda^3} \min_{w \in H^1_{\#,0}(\Omega_{me})} J^C_{\Omega_{me}}(w) . \tag{C.9}$$

The finite element discretization of (C.7) and (C.8) is obtained as described in Section 4.1. The system of equations to solve is represented by

$$\underline{\mathbf{A}}\, \underline{\chi}_h = \underline{f} , \tag{C.10}$$

where $\underline{\chi}_h$ is the vector of unknowns; and $\underline{\mathbf{A}}$ is the usual Laplacian operator. The local representation of $\underline{f}$ is

$$\hat{f}^{k_e}_{\alpha} = \int_{\Omega^{k_e}} \frac{\partial h_\alpha}{\partial y_1} d\mathbf{y} , \tag{C.11}$$

where $\alpha = 1, .., N_{local}$ depending on the choice of element (i.e. $\mathcal{P}_1$ or $\mathcal{P}_2$); and $k_e = 1, .., \mathcal{K}$.

The solution procedure consists of the conjugate gradient iteration with direct stiffness summation of Section 4.1.3 with two minor modifications. First, there are no Dirichlet boundary conditions, so the *mask* array is set to 1 for every node. Second, we require uniqueness of χ_h which is ensured by requiring that $\sum_{i=1}^{N_{gn}} \underline{\chi}_h = 0$, where N_{gn} is the number of global nodes.

The discrete effective conductivity k_h is given by

$$k_h = (1-c) - \frac{1}{\lambda^3} \underline{\chi}_h{}^T \underline{f} , \tag{C.12}$$

which can also be written as

$$k_h \;=\; (1-c) - \frac{1}{\lambda^3}\underline{\chi}_h{}^T \underline{\mathbf{A}}\underline{\chi}_h \,. \tag{C.13}$$

We determine the conductivity of simple cubic arrays of insulating spheres using $\mathcal{P}_1$ and $\mathcal{P}_2$ elements. Our results are compared to the analytical results of Sangani & Acrivos [43] which are accurate to $O(c^9)$. We define the error E_h^C

$$E_h^C \;=\; |k_h - k| \,. \tag{C.14}$$

Since E_h^C is a measure of the discretization error in the H^1 seminorm [6], it is $O(h^2)$ for linear elements and $O(h^4)$ for second order elements [50] [45]. Figure C-1 is a plot of E_h^C versus the nominal mesh spacing h for three types of elements: $\mathcal{P}_1$, subparametric $\mathcal{P}_2$, and isoparametric $\mathcal{P}_2$. The sphere volume fraction is $c = 0.2$. Linear elements exhibit the correct convergence rate and have a higher error than second order elements. Although we do not achieve a fourth order convergence rate for the bilinear elements, we do observe the correct trends for isoparametric meshes: the error is smaller than for subparametric meshes and the convergence rate is higher (close to $O(h^3)$). The third order convergence of the isoparametric meshes could be caused by a couple of phenomena: our "nodal" approximation of the actual H^1 seminorm might not be appropriate; or , due to relative coarse meshes, the results might be pre-asymptotic. Computer memory limitations prevent us from pursuing finer meshes to verify the latter possibility.

Figure C-2 is a plot of the effective conductivity k versus pore concentration c for simple cubic arrays (table C.1). We compare our results with the analytical ones of Sangani & Acrivos and the experimental ones of Lu & Kou [33]. The experimental results where obtained using a test cube that contains one insulating sphere and imposing Dirichlet boundary conditions on two opposite faces of the cube to create a temperature gradient, and insulating the other four faces of the cube. Note that these boundary conditions are not consistent with a periodic array of spheres. In any case, their results are still in good agreement with the exact ones.

In conclusion, we have tested our methodology for the special case of simple cubic

arrays of spheres. However, our formulation is quite general and able to handle random inclusion distributions. Moreover, although we do not pursue the micro-scale bounds, they can be obtained following the two-dimensional treatment of Cruz, Ghaddar & Patera [8].

concentration	k_h
0.008	0.98817
0.064	0.90704
0.125	0.82354
0.216	0.70684
0.343	0.55560
0.45	0.43275

Table C.1: Conduction versus concentration results for simple cubic array of spheres.

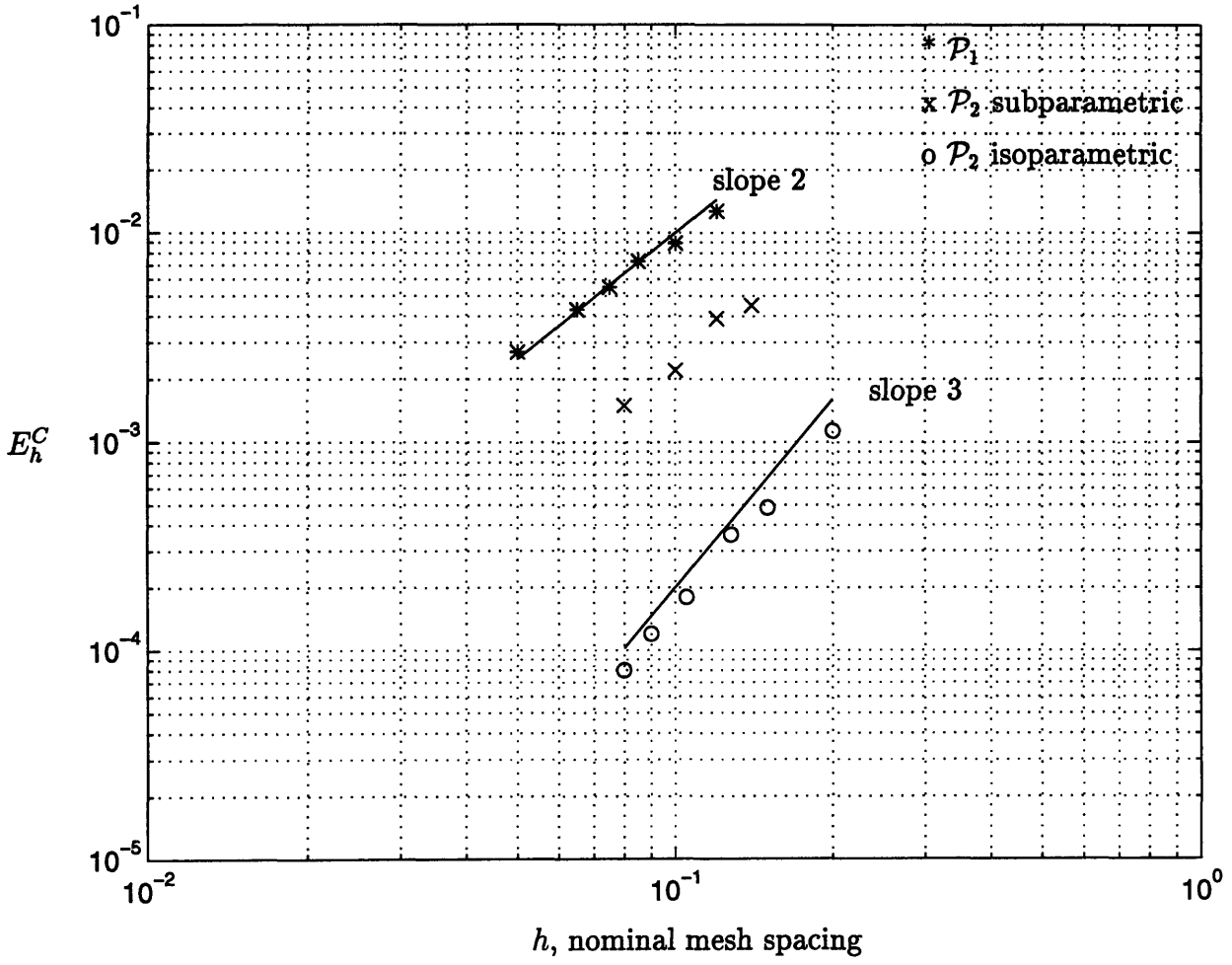

Figure C-1: Convergence plot for the heat conduction code: E_h^C versus h for simple cubic array ($c = 0.2$).

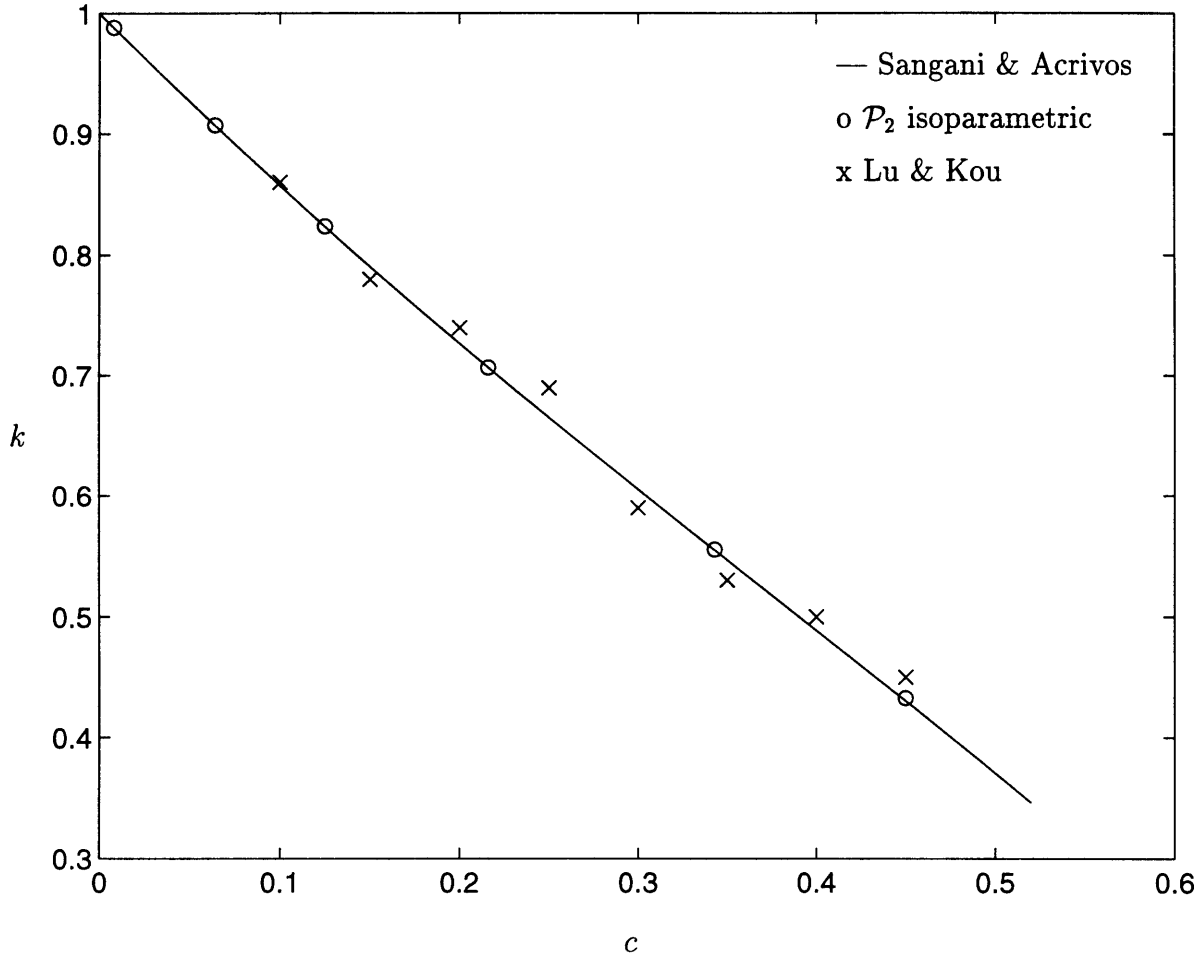

Figure C-2: Effective conductivity k versus concentration c for simple cubic array.

Bibliography

[1] G. Anagnostou, Y. Maday, C. Mavriplis & A. T. Patera (1990), "On the Mortar Element Method: Generalizations and Implementation." In *Domain Decomposition Methods for Partial Differential Equations*, T. F. Chan, R. Glowinski, J. Periaux and O. B. Widlund (eds.), SIAM, Philadelphia.

[2] G. K. Batchelor (1972), "Sedimentation in a Dilute Dispersion of Spheres," *J. Fluid Mech.*, **52**:245-268.

[3] G. K. Batchelor (1974), "Transport Properties of Two–Phase Materials with Random Structure," *Ann. Rev. Fluid Mech.*, **6**:227-255.

[4] A. Bensoussan, J.-L. Lions & G. C. Papanicolaou (1978), *Asymptotic Analysis for Periodic Structures*, North–Holland, Amsterdam.

[5] J. F. Brady & G. Bossis (1988), "Stokesian Dynamics," *Ann. Rev. Fluid Mech.*, **20**:111-157.

[6] M.C. Cruz (1993), "A Parallel Monte-Carlo Partial-Differential-Equation Procedure for the Analysis of Multicomponent Random Media," *Ph.D. Thesis*, Massachusetts Institute of Technology.

[7] M.C. Cruz, C.K. Ghaddar & A.T. Patera (1994), "Parallel Simulation of Multicomponent Random Media," *Proc. ASME Int. Symp. Parallel Comp. in Multiphase Flow Sys. Simulations*, S. Kim, G.K. Karniadakis, M.K. Vernon (eds.), FED**199**:1-9.

[8] M.C. Cruz, C.K. Ghaddar & A.T. Patera (1995), "A Variational-Bound Nip-Element Method for Geometrically Stiff Problems; Application to Thermal Composites and Porous Media," *Proc. R. Soc. Lond. A*, **449**:93-122.

[9] M.C. Cruz & A.T. Patera (1995), "A Parallel Monte-Carlo Finite-Element Procedure for the Analysis of Multicomponent Random Media," *Int. J. Numer. Methods Eng.*, **38**:1087-1121.

[10] A. Dasgupta, T.I-P. Shih, K.P. Kundu & J.M. Deur (1994), "Flow Past Arrays of Spherical Particles at Low to Intermediate Reynolds Numbers," Submitted to *J. Fluid Mech.*.

[11] J.F. Davidson, R. Clift & D. Harrison (1985), *Fluidization.* Second Edition. Academic Press, London.

[12] R.H. Davis & A. Acrivos (1985), "Sedimentation of Noncolloidal Particles at Low Reynolds Numbers," *Ann. Rev. Fluid. Mech.*, **17**: 91-118.

[13] R.H. Davis (1986), "The Effective Thermal Conductivity of a Composite Material with Spherical Inclusions," *Int. J. Thermophysics*, **7**:609-620.

[14] R.H. Davis & K.H. Birdsell (1988), "Hindered Settling of Semidilute Monodisperse and Polydisperse Suspensions," *AIChE Journal*, **34**:123-129.

[15] L. Durlofsky, J.F.Brady & G. Bossis (1987), "Dynamic Simulation of Hydrodynamically Interacting Particles," *J. Fluid Mech.*, **180**:21-49.

[16] J.Feng, H.H. Hu & D.D. Joseph (1994), "Direct Simulation of Initial Value Problems for the Motion of Solid Bodies in a Newtonian Fluid. Part 1. Sedimentation," *J. Fluid Mech.*, **261**: 95-134.

[17] C.K.Ghaddar (1994), "Parallel Analytico-Computational Methods for Multicomponent Media: Application to Thermal Composites and Porous Media flows," *Ph.D. Thesis*, Massachusetts Institute of Technology.

[18] G. H. Golub & C. F. Van Loan (1989), *Matrix Computations*, 2nd. edition, The Johns Hopkins University Press, Baltimore, Maryland.

[19] M. D. Gunzburger (1989), *Finite Element Methods for Viscous Incompressible Flows: A Guide to Theory, Practice, and Algorithms*, Academic Press, San Diego, California.

[20] J.M. Ham & G.M. Homsy (1988), "Hindered Settling and Hydrodynamic Dispersion in Quiescent Sedimenting Suspensions," *Int. J. Multiphase Flow*, **14**:533-546.

[21] J. Happel & H. Brenner (1983), *Low Reynolds Number Hydrodynamics*, Martinus Nijhoff, The Hague.

[22] F. Hecht & E. Saltel (1990), "Emc2: Editeur de maillages et de contours bidimensionnels," Manuel d'utilisation, Rapport Technique No. 118, INRIA.

[23] F.B. Hildbrand (1976), *Advanced Calculus for Applications*, Prentice-Hall, Englewood Cliffs, New Jersey.

[24] R. Hill & G. Power (1956), "Extremum Principles for Slow Viscous Flow and the Approximate Calculation of Drag," *Quart. J. Mech. Appl. Math.*, **9**:313-319.

[25] M.S. Ingberg & D.E. Womble (1994), "Hindered Settling Computations using a Parallel Boundary Element Method," *Parallel Computing in Multiphase Flow Systems Simulations*, **199**:53-59.

[26] K.O.L.F. Jayaweera, B.J. Mason & G.W. Slack (1964), "The Behavior of Clusters of Spheres Falling in a Viscous Fluid. Part 1. Experiment," *J. Fluid Mech.*, **20**:121-128.

[27] H. Kardestuncer, Editor in Chief (1987), *Finite Element Handbook*, McGraw-Hill, New York.

[28] J. B. Keller, L. A. Rubenfeld & J. E. Molyneux (1967), "Extremum Principles for Slow Viscous Flows with Applications to Suspensions," *J. Fluid Mech.*, **30**:97-125.

[29] N. Kikuchi (1986), *Finite Element Methods in Mechanics*, Cambridge University Press, Cambridge.

[30] S. Kim & S. J. Karrila (1991), *Microhydrodynamics: Principles and Selected Applications*, Butterworth–Heinemann, Boston, Massachusetts.

[31] G.J. Kynch (1952), "A Theory of Sedimentation," *Trans. Faraday Soc.*, **48**:166-176.

[32] J.C. Ladd (1993), "Dynamical Simulations of Sedimenting Spheres," *Phys. Fluids A*, **5**:299-309.

[33] K.T. Lu & H.S. Kou (1993), "The Effective Thermal Conductivity of Porous Material with Spherical Inclusions in a Tetragonal or Simple Cubic Array," *Int. Comm. Heat Mass Transfer*, **20**:489-500.

[34] A.V. Luikov, A.G. Shashkov, L.L. Vasiliev & Yu. E. Fraiman (1968), "Thermal Conductivity of Porous Systems," *Int. J. Heat Mass Transfer*, **11**:117-140.

[35] Y. Maday, D. Meiron, A.T. Patera & E.M. Rønquist (1993), "Analysis of Iterative Methods for the Steady and Unsteady Stokes Problem: Application to Spectral Element Discretizations," *SIAM J. Sci. Comput.*, **14**:310-337.

[36] C.C. Mei & J.-L. Auriault (1989), "Mechanics of Heterogeneous Porous Media with Several Spatial Scales," *Proc. R. Soc. London A*, **426**:391-423.

[37] R.L. Panton (1984), *Incompressible Flow*, John Wiley & Sons, New York, NY.

[38] A.T. Patera (1994), *Computational (Incompressible) Fluid Dynamics. Lecture Notes on Basic Material*, Lecture Notes from course 2.274 held at the Massachusetts Institute of Technology.

[39] J. Peiró, J. Peraire & K. Morgan (1993), "FELISA SYSTEM Reference Manual", Computational Aerospace Sciences Laboratory / Aeronautics Department MIT.

[40] S. Prager (1961), "Viscous Flow through Porous Media," *Phys. Fluids*, **4**:1477-1482.

[41] D.H. Rothman (1988), "Cellular-Automaton Fluids: A Model for Flow in Porous Media," *Geophysics*, **53**:509-518.

[42] P.G. Saffman (1973), "On the Settling Speed of Free and Fixed Suspensions," *Stud. Appl. Math.*, **52**:115-127.

[43] A.S. Sangani & A. Acrivos (1983), "The Effective Conductivity of a Periodic Array of Spheres," *Proc. R. Soc. Lond. A*, **386**:263-275.

[44] A. E. Scheidegger (1974), *The Physics of Flow through Porous Media*, 3rd. edition, University of Toronto Press, Toronto.

[45] G. Strang & G.J. Fix (1973), *An Analysis of the Finite Element Method*, Prentice-Hall, Englewood Cliffs, N.J..

[46] A.H. Stroud (1969), "A Fifth Degree Integration Formula for the n-Simplex," *SIAM J. Numer. Anal.*, **6**:90-98.

[47] G.I. Taylor, *Low Reynolds Number Flows*, Film, Encyclopaedia Britannica Educational Corp., Chicago, Ill.

[48] S. Torquato (1991), "Random Heterogeneous Media: Microstructure and Improved Bounds on Effective Properties," *Appl. Mech. Rev.*, **44**:37-76.

[49] A.A. Zick & G.M. Homsy (1982), "Stokes Flow through Periodic Arrays of Spheres," *J. of Fluid Mech.*, **115**:13-26.

[50] O.C. Zienkiewicz & R.L. Taylor (1989), *The Finite Element Method. Volume 1*, 4th. edition, McGraw-Hill, London. 2307-28